Rochester Institute of Technology

RIT Digital Institutional Repository

8-15-2023

Optimization of Alternative Mask Absorber Materials for EUV Lithography

Rajiv Naresh Sejpal
rns4256@rit.edu

R·I·T

Optimization of Alternative Mask Absorber Materials

for EUV Lithography

by

Rajiv Naresh Sejpal

A dissertation submitted in partial fulfillment of the requirements
for the degree of Doctorate of Philosophy in Microsystems Engineering

Microsystems Engineering Program
Kate Gleason College of Engineering

Rochester Institute of Technology
Rochester, New York
August 15, 2023

OPTIMIZATION OF ALTERNATIVE MASK ABSORBER MATERIALS FOR EUV LITHOGRAPHY
by
Rajiv Naresh Sejpal

Committee Approval:

We, the undersigned committee members, certify that we have advised and/or supervised the candidate on the work described in this dissertation. We further certify that we have reviewed the dissertation manuscript and approve it in partial fulfillment of the requirements of the degree of Doctor of Philosophy in Microsystems Engineering.

_____
Dr. Bruce W. Smith   Date
Distinguished Professor, Microsystems Engineering

_____
Dr. Parsian K. Mohseni   Date
Professor, Microsystems Engineering

_____
Dr. Ivan Puchades   Date
Professor, Microsystems Engineering

_____
Dr. Martin Burkhardt   Date
Research Staff Member, IBM

Certified by:

_____
Dr. Stefan Preble   Date
Director, Microsystems Engineering Program

_____
Dr. Doreen Edwards   Date
Dean, Kate Gleason College of Engineering

ABSTRACT

Kate Gleason College of Engineering
Rochester Institute of Technology

Degree: Doctor of Philosophy   **Program**: Microsystems Engineering

Authors Name: Rajiv Naresh Sejpal

Advisors Name: Dr. Bruce W. Smith

Dissertation Title: Optimization of Alternative Mask Absorber Materials for EUV Lithography

In efforts to continuously scale feature dimensions in semiconductor manufacturing, the industry has moved from refractive optical lithography to reflective extreme ultra-violet lithography (EUVL). The latter provides a significant improvement in the resolution by illuminating mask patterns using 13.5nm source wavelength at oblique chief ray angles (CRA).

A typical EUVL mask consists of a multilayer Bragg mirror topped with a 55-70nm Tantalum-based (Ta-based) absorber stack to obtain layout patterns. This current three-dimensional (3D) mask architecture in combination with a small source wavelength and oblique illumination angles results in mask 3D (M3D) effects such light shadowing, pitch dependent best focus variations, and image pattern shifts across different mask geometries. Three-dimensional mask topography effects lead to a loss of aerial image contrast and the usable depth of focus. To reduce some of these M3D effects, and to extend the 0.33 and 0.55 numerical aperture (0.33NA & 0.55NA) EUVL systems to future technological nodes, a thinner alternative mask absorber is necessary. This research focuses on determining the alternative mask absorber candidates for the reflective EUV lithography masks. This study does not intend to identify a singular absorber material but rather focuses on establishing a

framework to identify materials for various absorber technologies and optimize them accordingly to suit the layout-design requirements. The research methods adopted in this dissertation include analytical modeling, experimental validation, and lithography simulations.

A major contribution to this thesis is to use an analytical effective media approximation (EMA) model to identify optical constants of the material composites and model them as EUV absorber candidates. Using the EMA model, a technique to engineer EUV mask absorber composites is outlined. The validation of the EMA model is performed by multilayer thin films deposition and ellipsometry measurements at 800nm inspection wavelength in the UV-VIS-NearIR wavelength spectrum. Multilayer composites from three material systems specifically, the Mo-Ni, Mo-W, and the Ni-Al(1%Si) are fabricated via physical vapor deposition (PVD – sputtering) techniques. The ellipsometry measured optical constants of the multilayer composites show good agreement with the EMA modeled values.

Another key contribution to this thesis is the introduction of a co-optimization technique to determine the absorber design requirements in combination with 3D performance modeling of the nearfield intensity and phase to qualitatively identify their impact on the M3D effects. In the case of attenuated phase shifting mask (attPSM) absorbers, the relative absorber reflectivity is utilized to determine optimum imaging performance in the 30-55nm desired absorber thickness range. Absorber thickness corresponding to the absorber reflectivity peaks are shown to have high aerial image contrast through normalized image log slope (NILS) and low mask error enhancement factors (MEEF). Additionally, the high phase shift requirement ($> 200°$) justifies the need

of a low refractive index (low – n) of the absorber composites. It is found that optimum phase shift in EUVL depends on various factors including the absorber material, diffraction angle at the mask, mask pattern and the relative absorber reflectivity. Finally, using a similar optimization approach, index matched absorbers with high extinction coefficient (high n – high k) are also recommended as promising absorber candidates for future EUV generations.

This thesis is dedicated to my parents,
Shaila & Naresh Sejpal,
my sister,
Devashree Lakhani,
and to my wife,
Miral Sejpal.
Thank you for your love and support.

ACKNOWLEDGMENTS

Table of Contents

List of Figures

List of Tables

List of Acronyms:

3D	Three Dimensional
AI	Aerial Image
ALD	Atomic Layer Deposition
ALE	Atomic Layer Etch
ASD	Area Selective Deposition
attPSM	Attenuated Phase Shifting Mask
BARC	Bottom Anti-Reflective Coating
CAR	Chemically Amplified Resist
CD	Critical Dimension
CRA	Chief Ray Angle
DC	Direct Current
DOF	Depth of Focus
DR	Duty Ratio
DUV	Deep Ultra-Violet
EMA	Effective Media Approximation
EUVL	Extreme Ultra-Violet Lithography
FC	False Contact
FCR	False Contact Ratio
GPU	Graphic Processing Unit
HIL	High Index Liquid
HM	Hard Mask
IC	Integrated Circuit

ICP	Inductively Coupled Plasma
IRDS	International Roadmap for Device and Systems
ITRS	International Technology Roadmap for Semiconductors
LWR	Line Width Roughness
M3D	Mask Three Dimensional
MEEF	Mask Error Enhancement Factor
MLD	Molecular Layer Deposition
MSE	Mean Square Error
NA	Numerical Aperture
NILS	Normalized Image Log Slope
NTE	Non Telecentricity Error
NTRS	National Technology Roadmap for Semiconductors
OAI	Off Axis Illumination
OPC	Optical Proximity Correction
PAC	Photo-Active Compound
PEB	Post Exposure Bake
PSM	Phase Shifting Mask
PTD	Positive Tone Development
PVD	Physical Vapor Deposition
RF	Radio Frequency
RIE	Reactive Ion Etching
RMSE	Root Mean Squared Error
SMO	Source Mask Optimization

SRAF   Sub-Resolution Assist Features

UV-VIS-NearIR   Ultraviolet-Visible-Near Infra-Red

VASE   Variable Angle Spectroscopic Ellipsometry

1 Introduction

Integrated circuits (ICs) are extensively used in all modern electronic devices for a variety of applications in a diverse consumer market. ICs have been at the core of every technology since they were proposed by Jack Kilby in 1957 at Texas Instruments [1]. Since its inception over half a century ago, the size and architecture of the IC has changed significantly. The first IC was a phase shift oscillator using germanium transistors [2]. Even in the early stages of development it was clear that the future of electronic systems will be driven by their size and cost. In 1958, Jean Hoerni of Fairchild Semiconductor invented the first diffused transistor by using photolithography techniques developed by Robert Noyce and Gordon Moore who later founded Intel in 1968. The processing technique was then labelled "PLANAR" process. The formation of native oxide on the surface of these planar devices protected the device junctions and enabled higher stability.

In 1965, Gordon Moore published an article in which he predicted that by the year 1975, the number of components on an IC would be roughly 65,000 to keep the manufacturing cost to a minimum as shown in Figure 1.1 below [3]. This meant that the total number of components per circuit would double every two years through scaling, now famously known as the Moore's Law [4], [5]. In 2023, the highest component count (transistors) on a commercially available graphics processing unit (GPU) from AMD is 153 billion [6]. Component scaling of such magnitude has been primarily obtained by using optical lithographic techniques.
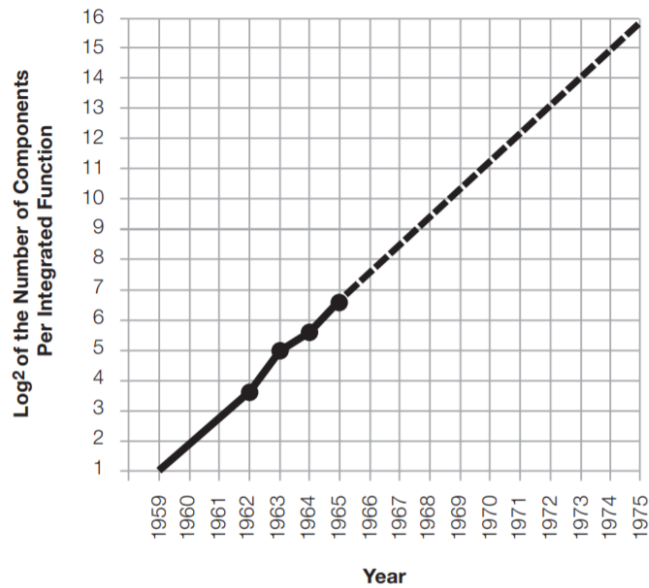
Figure 1.1: Moore's Law predicting component count till year 1975 [3].

1.1 Microlithography Techniques and Systems

Lithographic techniques have undergone significant advancements in a relatively short semiconductor history. There are three main types of lithography techniques: contact lithography, proximity lithography and projection lithography as shown in Figure 1.2 [7]. In the early years till mid 1970's, the contact and proximity lithography techniques were typically used for pattern transfer. In contact lithography, a mask mold is pressed on to the wafer stack enabling pattern transfer. Contact lithography can provide high resolution but suffers from mask damage and defects. Proximity lithography is a resolution limited technique which is driven by the gap between the mask and the exposure wavelength. On the other hand, projection lithography projects the mask image onto the photoresist using a lens assembly. The projection optics are designed to provide a demagnified mask image that enables high resolution. With the introduction of sophisticated computer aided lens

designs, projection lithography has been the primary method for pattern transfer in the semiconductor IC industry.

Contact   Proximity   Projection
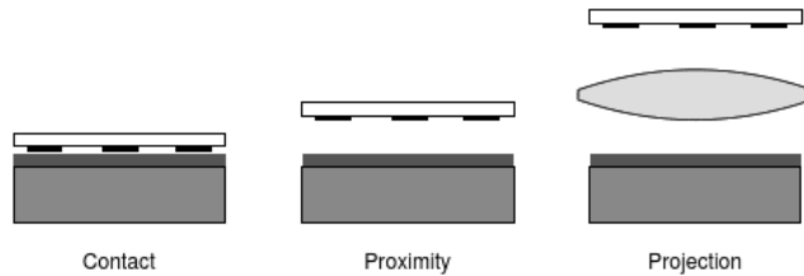
Figure 1.2: Pattern transfer techniques in microlithography systems [7].

A projection microlithography system as shown in Figure 1.3 can be divided into three parts: the illumination system, the projection lens assembly, and the wafer positioning system [8]. Light sources are typically Hg arc lamps or high-powered lasers. The light from the source goes through the condenser lens optics to achieve uniform illumination intensity. This light continues through the reticle and forms an image of the source at the entrance pupil of the projection lens. The size of the source image on the entrance pupil defines the degree of coherence. The projection lens or the lithographic lens is an assembly of a large number of simple lens elements (usually over 30) designed to typically provide 4× demagnification of the mask image. A large number of lens elements are required to rectify the optical aberrations in the system. The demagnified image is then directed to the substrate coated with a photoresist which is sensitive to the illumination wavelength. The substrate is mounted on a highly sophisticated wafer positioning system with the wafer stage in the vacuum chamber. The wafer stage is then moved in the x- and y- directions to expose all the dies on the substrate. The stepping process is carried out with nanometer accuracy that is within the alignment tolerances of the given process [8].
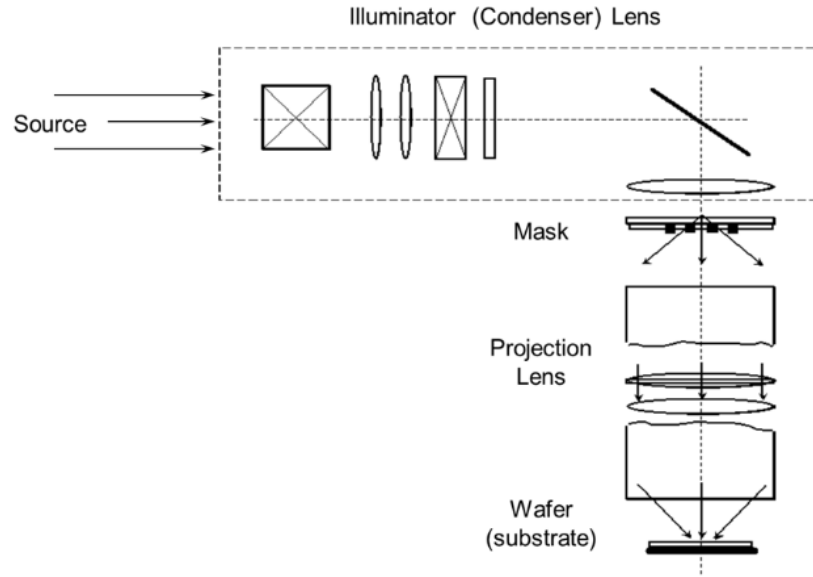
Figure 1.3: Block diagram illustrating projection lithography system [8].

1.2 Microlithography Process

Pattern transfer in optical lithography is performed with a process that includes substrate and stack preparation, exposure and development, metrology, semiconductor processing and finally, resist strip. Depending on the pattern design and requirements, the process specifics such as resist height, exposure time etc., may change however, the process flow is generally the same.

In substrate and stack preparation, the wafer is first cleaned to remove particle contamination. It is then subject to a dehydration bake to remove any water molecules which results in poor resist adhesion. Additionally, the wafer is coated with an adhesion promoter before BARC (bottom anti-reflective coating) or resist. After spin coating the resist, the wafer is prebaked to improve the resist stability at room temperature.

The resist coated wafer is exposed with the mask image through a stepper/scanner system described in section 1.1. After the exposure, the wafer is heated again in a step called the post-exposure bake (PEB). In the case of conventional photoresists, the purpose

of the PEB is to create a solubility differential by hardening the non-exposed part of the resist (PTD: positive tone development resist). PEB is also executed for chemically amplified resists (CAR) for increased photoreaction and deprotection to generate a solubility differential. Finally, the resist is developed to obtain the mask patterns on the photoresist.

Patterns obtained on the photoresist are inspected for pattern uniformity and defects. Subsequent semiconductor processing (etching, deposition etc.) is realized if the resist patterns meet the design requirements. Finally, the remaining resist is stripped to enable further wafer processing.

1.3 Optical System Considerations in Lithography

A projection lithography tool is a diffraction limited system which is characterized by its resolution and depth of focus (DOF). The resolution is the minimum pitch that can be imaged with sufficient pattern fidelity. As the projection lithography systems closely resemble microscopes, their resolution can be mathematically represented using Lord Rayleigh's criterion [9] shown in Equation (1.1) as:

$$hp_{min} = k_1 \frac{\lambda}{NA} \tag{1.1}$$

Here, hp_{min} is the minimum resolvable half-pitch, k_1 is a process dependent factor, λ is the source wavelength and NA is the numerical aperture of the projection lens (objective lens). The process parameter k_1 is independent of the projection lens assembly and it is determined by processing factors such as the photoresist contrast, illumination source shape, mask type and resolution enhancement techniques such as source mask optimization (SMO) [10]–[13], off axis illumination (OAI) [14], phase shift masking (PSM) [15], optical

proximity correction (OPC) [16]–[24] and sub-resolution assist features (SRAF) [24]–[28].

There is a theoretical minimum limit on k_1 of 0.25. For a $k_1 < 0.25$, the image contrast between a line and space pattern is zero. Traditionally, the resolution is described in terms of half-pitch. For equal lines and spaces i.e., 1:1 duty ratio (DR), the half pitch is equal to the smallest resolvable feature. The smallest resolvable feature is also known as critical dimension (CD).

Another derivative of Lord Rayleigh's criterion is the depth of focus (DOF) given by Equation (1.2). The DOF is the distance in the optical axis at which the resolved image is distinguishable and satisfactory for further processing. Therefore, it is the value of maximum acceptable defocus.

$$DOF = \pm k_2 \frac{\lambda}{NA^2} \tag{1.2}$$

where, k_2 is also a process dependent factor. The value of k_2 for a specific process can be determined by first measuring the common DOF of the layer for a given range of exposure latitude.

There is a trade-off between the resolution and DOF for a projection lens system as seen from Equation (1.1) and (1.2). Resolution can be improved by scaling the source wavelength. Reducing the source wavelength enables printing of smaller features. However, smaller wavelengths result in lower depth of focus. Similarly, higher NA systems can improve the system resolution at the cost of reduced depth of focus. Furthermore, the DOF degrades with the square of the NA. Hence, it is more favorable to scale wavelength than the numerical aperture.

Since the commercialization of steppers [29] in the 1980s, lithography systems have seen reduction in source wavelengths along with the incremental changes in the

numerical aperture. The earliest reduction stepper used mercury g-line wavelength of 436nm and had a projection lens of 0.28 NA [30]. The g-line steppers could provide a resolution down to 1µm. In the mid-1980s, new steppers with 365m source wavelength (i-line lithography) enabled shrinking of feature sizes to 300nm. The systems also observed higher NA ranges between 0.48 – 0.60 [31]. In the 1990's the resolution was scaled utilizing 248nm KrF laser sources at 0.80 NAs and higher. By the early 2000s, deep ultraviolet (DUV) laser sources with high efficiency were utilized. The following lithography generations implemented a 193nm ArF laser at 0.90 NA and higher. Combining higher NA and shorter wavelengths allowed scaling the resolution down to 130nm with aggressive engineering techniques [8]. However, the NA as described in equation (1.3) has the theoretical upper limit of 1 as the refractive index of air/vacuum is 1. Substantial efforts were invested in developing the 157nm lithography using the F_2 laser but the material challenges for the photoresist and lens assembly proved extremely difficult [32], [33]. Additionally, wavelength scaling was not as significant as previous node changes and eventually 157nm lithography was abandoned.

$$NA = n\,sin(\alpha) \qquad (1.3)$$

here *n* is the refractive index of the medium and α is half of the angle from the focus point to the lens edge.

To continue shrinking feature sizes, the NA was scaled by changing the projection medium from air to water. Water with a refractive index of 1.44 enabled NA as high as 1.35 while keeping the wavelength constant at 193nm. This is called immersion lithography or *193i* lithography [34], [35]. The NA can be further increased by implementing high index liquids (HIL) [36], but such techniques suffer from lens and

substrate contamination. Additionally, a completely new process flow with HIL compatible wafer stack is required. As obtaining shorter wavelength and higher NA (> 1.35) became progressively difficult, process enhancement techniques such as multiple patterning were successfully used. Multiple patterning techniques such as double/triple pattering [37], [38] require multiple exposures either by decomposition or self-aligned processes [39] which enhanced the resolution significantly. This allowed lithography operations below the theoretical minimum of 0.25 k_1 values. However, multi-patterning processes substantially increase the cost and time of production which is proportional to the number of exposures.

1.4 Technology Roadmaps

Advanced lithography and semiconductor processing techniques are complex processes that require multiple operations to achieve target requirements and final device. It is therefore necessary that every aspect of fabrication technology advances simultaneously. To achieve such standardization, roadmaps have been historically used by the semiconductor industry as the target reference for future research. Such a roadmap was first published in 1991 by National Technology Roadmap for Semiconductors (NTRS). As the semiconductor industry grew globally, NTRS evolved in 1998 to form the International Technology Roadmap for Semiconductors.

The ITRS comprised of a team of semiconductor industry experts from US, Europe, Korea, Japan, and Taiwan. Each year, ITRS introduced a roadmap outlining the requirements of a new technological node with the outlook for a foreseeable future [40]. Each new node had smaller feature sizes compared to its previous counterpart with tighter device specifications and tolerances. To obtain a clear distinction between the devices, DRAM (dynamic random-access memory), flash and logic chips had separate respective

roadmaps. Between 1998 to 2015, the ITRS served as the primary reference point for semiconductor research in areas such as process integration for devices and structures, factory integration, IC interconnects, microelectromechanical system (MEMS) devices and other research ideas. As the semiconductor industry grew, ITRS was reorganized and relabeled as ITRS 2.0 to integrate emerging semiconductor and IC environment. Seven International Focus Teams (IFT) were formed to overlook the previous as well as new technological elements as shown in Figure 1.4. As the microsystems and the semiconductor ecosystem continued to evolve beyond Moore and, to blend emerging systems and technology, International Roadmap for Device and Systems (IRDS) was initiated in 2016.
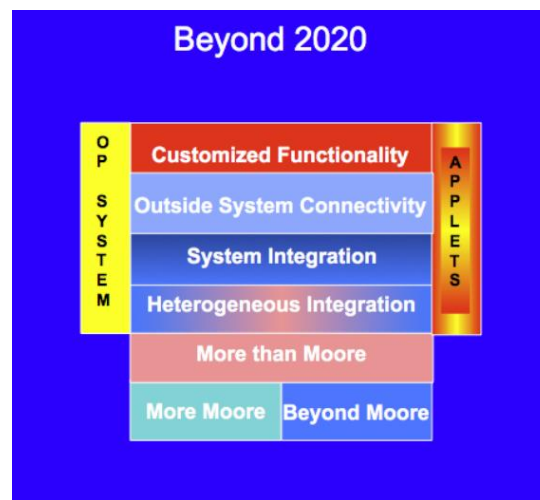
Figure 1.4: 2012 ITRS 2.0 highlighting seven focus areas for 2020 and beyond.

IRDS succeeds ITRS with the intent to provide predictions, and outlines the path for industry, academia, and research of electronic devices and manufacturing. IRDS focuses on technological advancement by emphasizing systems, architectures, and applications. IRDS implements this through three main goals:

- Identify the respective technology trends over a 15-year period.

- Determine challenges and solutions.

- Facilitate collaboration through conferences and workshops.

Figure 1.5 shows the lithography challenges identified in 2022 IRDS revision. The high-NA anamorphic EUV is expected to be implemented by the year 2025. The major challenges for next generation EUV lithography includes improved resist processing, stitching of half-fields associated with high-NA EUV, throughput, and alternative mask technologies. This study is dedicated to identifying such improved mask technologies through determining the novel mask absorber candidates for EUV lithography. Implementing enhanced EUV masks also presents the potential to extend the 0.33NA EUVL systems to next generation nodes.

Table LITH-2	Potential Solutions for Leading-Edge Logic Lithography					
	2022	2025	2028	2031	2034	2037
Logic node	3 nm	2.1 nm	1.5 nm	1.0 nm	0.7 nm	0.5 nm
Node	G48M24	G45M20	G42M16	G40M16T2	G38M16T4	G38M16T6
Minimum ½-pitch	12 nm	10	8 nm	8 nm	8 nm	8 nm
Primary options for logic	EUV 0.33.NA multiple patterning	EUV 0.33.NA multiple patterning EUV 0.55.NA single patterning	EUV 0.55.NA single patterning EUV 0.55.NA multiple patterning	EUV 0.55.NA single patterning EUV 0.55.NA multiple patterning Beyond EUVL (λ=6.X nm)	EUV 0.55.NA single patterning EUV 0.55.NA multiple patterning Beyond EUVL (λ=6.X nm)	EUV 0.55.NA single patterning EUV 0.55.NA multiple patterning Beyond EUVL (λ=6.X nm)
Potential solutions for cost reduction, LER reduction		Optical + DSA EUV + DSA	Optical + DSA EUV + DSA	Optical + DSA EUV + DSA	Optical + DSA EUV + DSA	Optical + DSA EUV + DSA

Figure 1.5: Lithography challenges identified in 2022 IRDS revision. The 0.55NA lithography to be implemented by the year 2025.

1.5 Aerial Image Formation

The imaging capability of a lithographic system is determined by its minimum achievable resolution. The minimum achievable resolution of a lithographic system can be calculated using the Eq. (1.1) that shows the minimum resolvable half-pitch. Occasionally,

half-pitch (hp_{min}) or critical dimension (in case of 1:1 duty ratio) are interchangeably used to define the minimum resolution of the system.

When a mask pattern *m(x, y)* is illuminated by a coherent point source, its image at a distance *z* from the mask in the far-field Fraunhofer region can be calculated using the Fourier transform [41] of the mask object in the pupil plane *(x', y')*. This is given by Eq. (1.4), known as the Fraunhofer diffraction integral. Here, *E(x', y')* is the electric field at plane *(x', y')* with *u, v* spatial frequencies. The spatial frequencies can be calculated using Eq. (1.5).

$$E(x',y') = \iint\limits_{-\infty}^{\infty} m(x,y)e^{-2\pi i(ux+vy)}dxdy \tag{1.4}$$

$$u, v = \frac{x', y'}{z\lambda} \tag{1.5}$$

The electric field at the entrance pupil of the objective lens is the Fourier transform of the illuminated mask object. The general representation of the electric field is given in Eq. (1.6), where $\mathcal{F}$ is the Fourier transform operator.

$$M(u, v) = \mathcal{F}\{m(x,y)\} \tag{1.6}$$

The physical size of the objective lens, described in terms of its numerical aperture, determines the maximum diffracted light it captures. In an ideal scenario with a perfect objective lens, the lens transmission is 100%. The pupil function in terms of spatial frequencies is described in Eq. (1.7). The Eq. (1.7) is the equation of a circle in cartesian co-ordinates.

$$H(u, v) = \begin{cases} 1 & \sqrt{u^2 + v^2} < \dfrac{NA}{\lambda} \\ 0 & \sqrt{u^2 + v^2} > \dfrac{NA}{\lambda} \end{cases} \tag{1.7}$$

The resulting image from the exit pupil, converging on a point in the image plane *(x", y")* is the convolution of the mask object function ***m*** with the pupil function ***H***. The calculation complexity of convolution is simplified to multiplication in the frequency domain. Therefore, the resulting image can be calculated as the inverse Fourier transformation of the product of ***M*** with ***H*** and is given in Eq. (1.8).
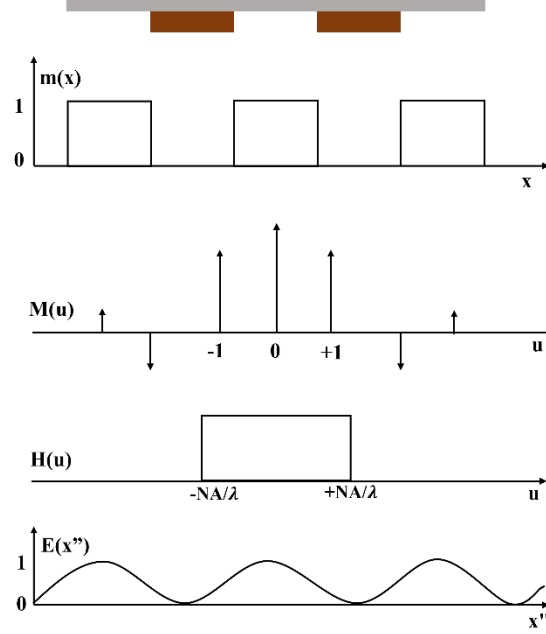
Figure 1.6: Aerial image formation of 1D line/space grating with 1:1 duty ratio.

$$E(x", y") = \mathcal{F}^{-1}\{M(u, v)H(u, v)\} \qquad (1.8)$$

where *(x", y")* are the plane coordinates in the image plane and $\mathcal{F}^{-1}$ is the inverse Fourier transform operator. The aerial image intensity distribution $I(x", y")$ in the image plane is then the squared magnitude of the electric field.

$$I(x", y") = |E(x", y")|^2 \qquad (1.9)$$

By optimizing the projection optics, smaller feature sizes at the image plane may be achieved. The Eq. (1.8) is then modified by the inclusion of magnification (or demagnification) factor. Aerial image formation for a 1D line/space pattern is depicted in

Figure 1.6. The 1D grating has a 1:1DR. The mask function m(x) for a 1D grating can be mathematically represented as a rectangular function.

The aerial image intensity distribution in Eq. (1.9) assumes spatially coherent imaging illumination from an on-axis point source. In practice, lithography systems use non-zero size partially coherent sources that illuminate the mask at multiple angles. The aerial image then becomes the incoherent sum of coherent point sources [42].

1.6 Extreme Ultraviolet Lithography

The current technological node utilizes extreme ultraviolet lithography (EUVL) systems that operate at 13.5nm source wavelength. Such short wavelengths improve the resolution with systems that do not require high NA. At present, the state-of-the-art EUVL systems operate at 0.33-0.55 NA. To avoid absorption and scattering of x-ray wavelengths, EUVL systems are operated under vacuum. Additionally, as the index of refraction of almost all materials at 13.5nm wavelength is close to 1 ($n = 1$ for vacuum), EUVL systems employ reflective optics using multilayer interference coatings.

Figure 1.7: Schematic of a typical 0.33NA EUVL system from ASML.

Figure 1.7 shows a the schematic of a typical 0.33NA EUVL system [43], [44]. The multilayer coatings used for the EUV lenses are also used to manufacture EUV mask blanks which are then coated with an absorbing material to obtain design patterns. The

0.33NA EUVL systems can match the resolution obtained using the *193i* deep ultraviolet

systems (DUV) systems without multiple patterning, reducing the cost of manufacturing.

Optical reflective elements of an EUVL system such as a photomask and the lens

assembly operate on Bragg reflection [45], [46]. Due to the reflective optics, an EUVL

system operates at oblique incidence angles. The chief ray angles (CRA) of 0.33NA and

0.55NA EUVL systems are 6º and 5.355º, respectively. The maximum reflectivity of an

EUV mirror is limited to approximately 70% [47]–[50]. Figure 1.8 shows the reflectivity

of Mo/Si (40 bilayer pairs) multilayer mirror vs. wavelength [51]. The reflectivity peaks at

13.5nm at normal incidence angle. The reflectivity reduces (shifts) as the angle of incidence

increases. It is therefore important to have a high power EUV source for high volume

manufacturing (HVM) and comparable yield.
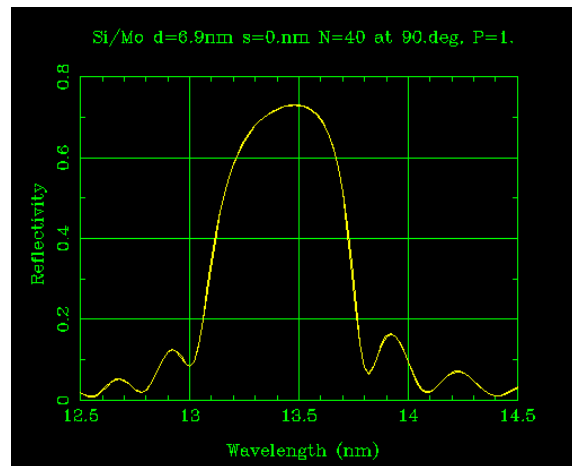
Figure 1.8: Multilayer reflectivity of Mo/Si multilayer mirror at normal incidence (90º). N **is the number of bilayers and** d **is the period of bilayer.**

There are several other non-ideal effects that make EUVL challenging. Some of

these effects such as flare, stochastic effects, and aberrations are a direct result of

wavelength scaling [52]. Another major issue specific to EUVL systems is the so-called

mask three-dimensional (M3D) effects, discussed briefly in the following sections.

1.6.1 M3D Effects

A conventional EUV mask uses 40 Molybdenum – Silicon (Mo/Si) bilayer pairs to reflect the light, typically incident at a chief ray angle, as shown in Figure 1.9 (6° for 0.33 NA systems) [53]. As currently employed in 0.33 – 0.55 NA systems, EUV lithography employs binary masks using non-reflective TaBN mask absorbers [54], in a typical thickness range of 55-70nm. By extending the existing Ta mask absorber technology, the next generation technology nodes may suffer image contrast loss from M3D effects [55] resulting in, among other things, shadowing, best focus shifts through-pitch, and image pattern shifts [56]–[59].
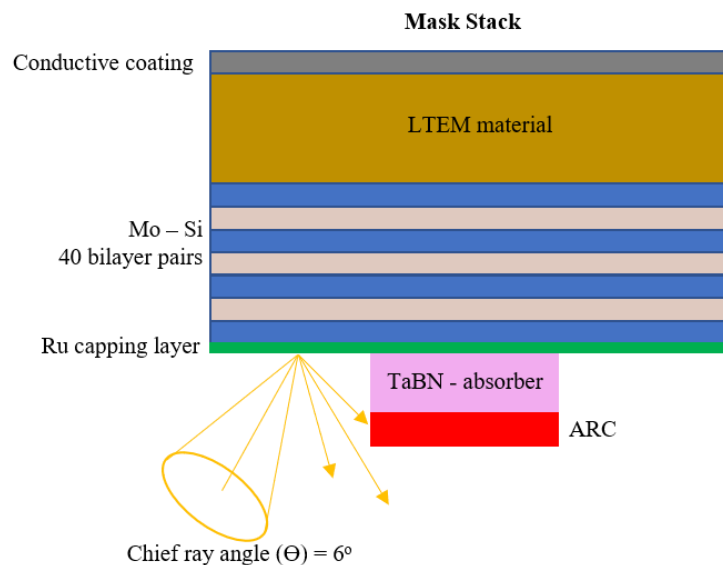
Figure 1.9: A typical EUV mask-stack with TaBN mask absorber. The 6º CRA is for 0.33NA systems.

Figure 1.10 shows the aerial image contrast through Normalized Image Log Slope (NILS) for a 61nm Ta-based mask absorber stack for dense line/space and contact-hole patterns through pitch, respectively. NILS is a product of the Aerial Image Log Slope (ILS) and the critical dimension (CD). Through NILS, the resist exposure profile related to aerial image intensity can be determined. NILS serves as an important metric to represent many lithography process behaviors including the image contrast. For EUV lithography, a NILS

value above 2 is desired. The simulations are performed for a 0.33NA EUVL system using the *Prolith* simulator. Telecentric dipoles are used to illuminate the mask patterns.
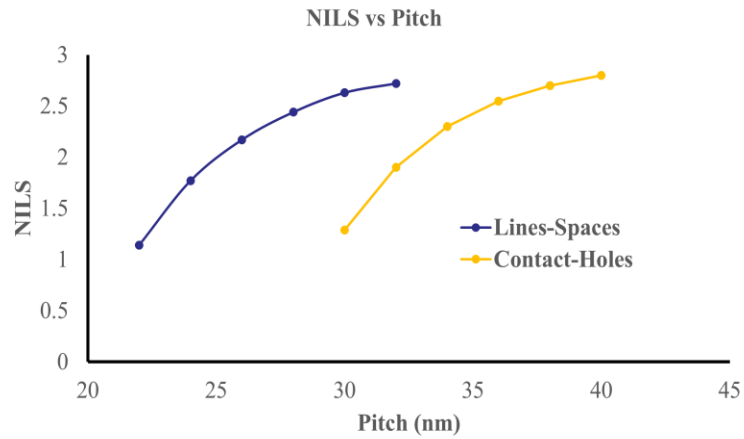
NILS vs Pitch

Figure 1.10: Simulated NILS vs Pitch for dense lines-spaces and contact hole patterned using conventional Ta-absorber mask stack.

The NILS performance of the line/space pattern progressively degrades beyond the 28nm pitch. The 28nm pitch corresponds to k_1 value of approximately 0.34. In the case of contact-holes, NILS value falls below 2 beyond the 34nm pitch ($k_1 = 0.41$). Further scaling of k_1 at 0.33NA is possible by using an alternative absorber to print smaller features with high image contrast.
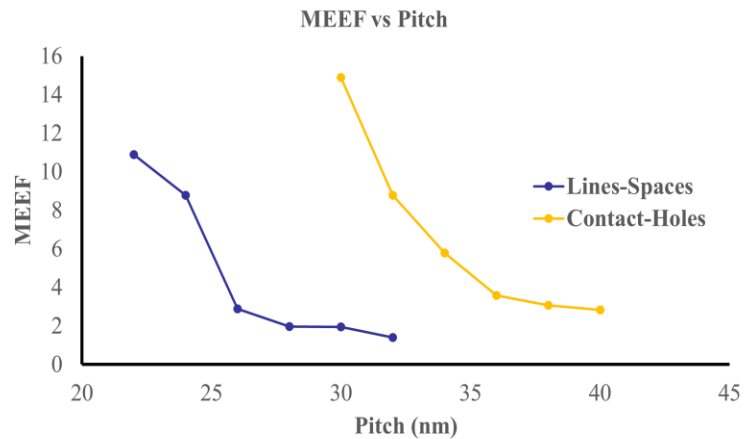
MEEF vs Pitch

Figure 1.11: Simulated MEEF vs Pitch for dense lines-spaces and contact hole patterned using conventional Ta-absorber mask stack.

The mask error enhancement factor (MEEF) is another important metric that needs consideration for future technological nodes. MEEF is a measure of how a small change

on the mask is propagated onto the image at the wafer. Figure 1.11 shows the simulated

Mask Error Enhancement Factor (MEEF) vs pitch for the line/space and contact-holes

patterns. The simulations are performed on a 35nm generic EUV resist using the *Prolith*

simulator. MEEF increases significantly below about 26nm and 36nm pitch for line/space

and contact-holes patterns, respectively. Introducing alternative mask technologies with

reduced MEEF and M3D effects has the potential to significantly enhance the pattern

transfer process using EUV lithography.

1.6.2 Shadowing

Due to the reflective design of the EUVL optics, the chief ray (paraxial beam) is

not orthogonal to the mask plane. Such oblique incidence angles cause a shadowing effect

on mask absorber lines that are perpendicular to the projected beam of light. The shadowing

effect is demonstrated in Figure 1.9, where part of the reflected beam is blocked by the

absorber layer. The effect of shadowing is indicated by the dashed circle in Figure 1.12 for

10nm isolated absorber lines. The highlighted region shows additional darker region in

multilayer (below 300nm on z-axis) on one side of the absorber compared to the other.
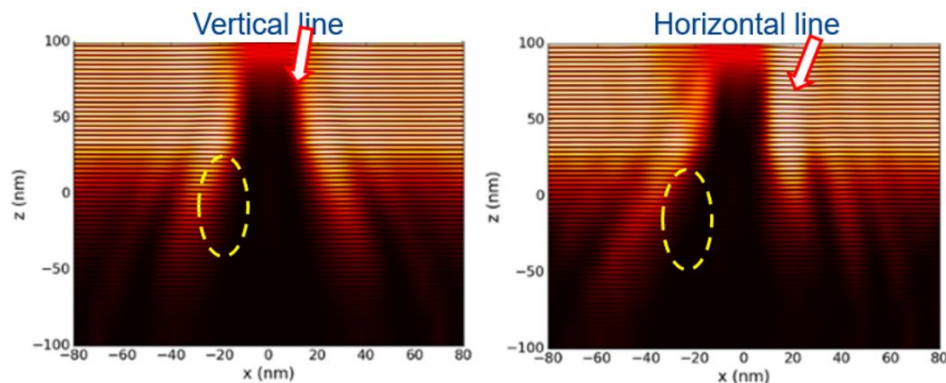
Figure 1.12: Nearfield distribution intensity of 61nm TaBN mask absorber stack. Yellow ring highlights shadowing effect when illuminated at CRA = 6º.

Shadowing leads to orientation sensitive line width variation. This is because

vertical features are parallel to the direction of light incidence. Horizontal features that are

perpendicular to the scan direction therefore experience larger shadowing effect. Shadowing can be reduced by reducing the height of the mask absorber, but it cannot be eliminated because the light is reflected within the multilayer mirror. Some shadowing will exist even if case of an ideal absorber with 0nm thickness [60].

1.6.3 Non-Telecentricity

A telecentric lens is a lens designed to have constant magnification (or demagnification) irrespective of the location of the object. EUV lithography systems employ telecentric projection lenses. The telecentricty errror or non-telecentricity (NTE) in EUV is interchangeably used with the source non-telecentricity that represents the variation of the feature position with regards to focus.
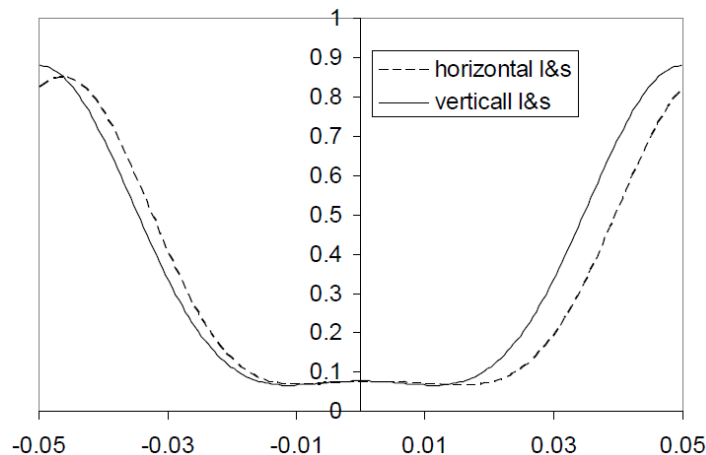
Figure 1.13: Non-Telecentricity error leading to image pattern shift and CD variations between horizontal and vertical line/space patterns.

Non-telecentricity arises from the asymmetric reflections of different mask patterns. The NTE is expressed in nm placement error vs. micrometer defocus (or millirad) and it is a function of illumination angle, mask absorber thickness, pattern pitch and source shape [61]. As shown in Figure 1.13, the horizontal and vertical patterns are shifted with respect to their nominal positions [62]. The patterns also have different CD values due to the orientation sensitive shadowing.

1.6.4 Best Focus Variations

Pitch variations at the mask lead to best focus shifts. Diffraction orders resulting from different mask pitch occupy different positions in the objective lens pupil. Therefore, through pitch patterns interact with spherical aberration of the projection optics, and with the phase error that is introduced on the mask through the absorber. This effect is prominent for smaller pitches that are at the edge of the objective lens pupil. Figure 1.14 shows the best focus variations through pitch [63] for quasar illumination. Substantial variation in the best focus positions at smaller pitches are indicated by the dashed red region.
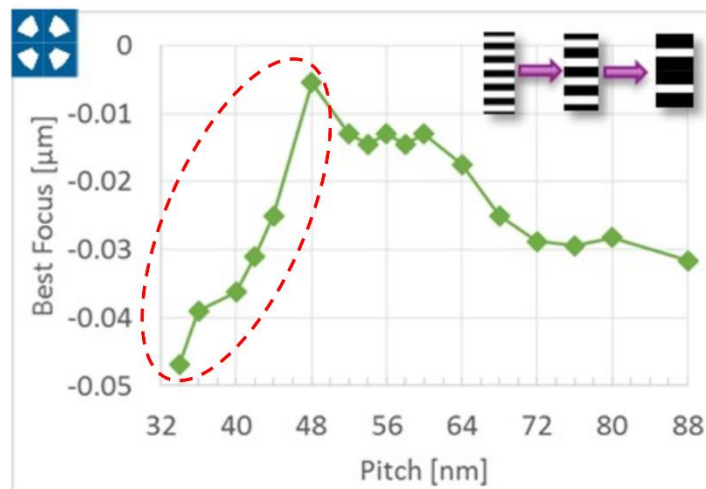
Figure 1.14: Pitch dependent best focus variations.

Best focus variations in combination with non-telecentricity results in edge placement error (EPE) and overlay errors. Identifying a thinner alternative mask absorber that can reduce the best focus variation range as well reduce some of the M3D effects will improve the overall imaging performance [63]–[72].

1.7 High-NA Anamorphic Imaging

Single exposure 0.33NA EUV patterning becomes challenging beyond 28nm pitch for line/space patterns and 34nm pitch for contact-holes patterns, as shown in Figure 1.10

& 1.11. Continued scaling beyond these dimensions may require multi-patterning techniques. Multi-patterning techniques in EUV significantly increase the cost of production due to a larger number of mask/layers required.

After enabling EUV wavelength scaling, the next update to the EUV lithography tool increases the NA of the projection optics to 0.55 [43], [73]–[77]. This is also proposed in the 2022 IRDS revision shown in Figure 1.5. Increasing the NA in EUV lithography is challenging due to the angular illumination necessity. Larger illumination angles are necessary to avoid overlapping of incident and reflected wavefronts as shown in Figure 1.15(a). Overlapping can be eliminated by increasing the CRA but larger incidence angles lead to unacceptable contrast loss and M3D effects.

(a) Full field exposure at 0.55NA
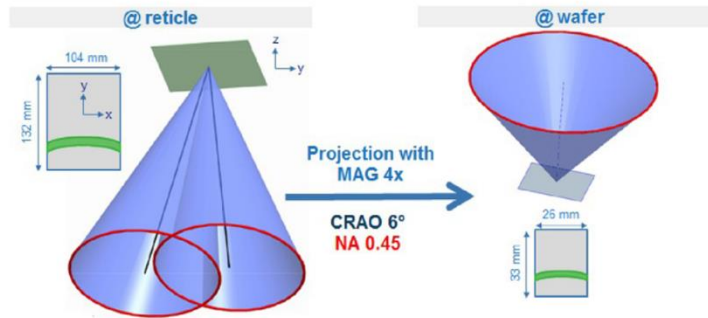
(b) Half field exposure at 0.55NA
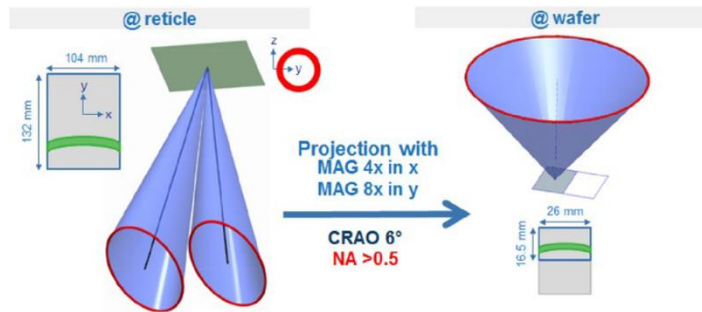
Figure 1.15: 0.55 high-NA EUV optical design considerations. (a) Overlapping wavefronts at 6° CRA for full-field exposure and (b) non-overlapping wavefronts at 6° CRA for half-field exposure using anamorphic design [71].

By implementing anamorphic projection optics, the CRA can be maintained below 6º at 0.55NA (5.35º). The anamorphic projection systems will have 4× demagnification in the x- direction and 8× demagnification in the y- direction (scan direction). Therefore, the mask designs will also have anamorphic layouts with 2× feature sizes in the y-direction. To accommodate layout design changes, only half-field exposures are possible. Figure 1.15(b) shows the high-NA anamorphic EUV design schematically [73].

As previously mentioned, increasing the NA of the objective lens with the conventional design (0.33NA system) requires large incidence angles on some of the projection optics mirrors. Such large angles result in unacceptable reflectivity losses. Therefore, the 0.55NA EUVL systems will utilize central obscuration in a projection lens. The conceptual design of 0.55NA EUVL system in comparison with 0.33NA system is shown in Figure 1.16. As observed in the presented example, the obscured lens may block parts of the ±1 diffraction orders [78]. The light loss results in image contrast loss. Therefore, the obscuration size is limited to ~2-4%. Obscuration aware source mask optimization (SMO) may also be implemented to eliminate this issue.
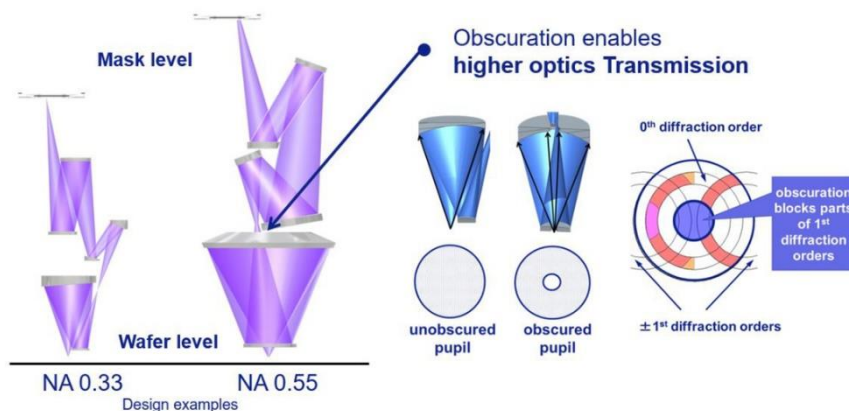
Figure 1.16: Conceptual design of 0.55NA EUVL system in comparison with 0.33NA system. The obsucred pupil for 0.55NA system blocks parts of ±1 diffraction orders [76].

The semiconductor industry has started considering hyper-NA (>0.7NA) EUVL systems [79]. Further increasing the NA will result in larger illumination angles that is followed by aerial image contrast loss. Larger illumination angles will also result in higher M3D effects such as shadowing even at a lower thickness of the alternative absorbers. Finally, substantial light polarization will also be experienced at such large incidence angles. Reducing the polarization induced contrast loss is challenging and may require an EUV light polarizer in combination with aperiodic multilayer mirrors.

1.8 Outline

The outline of this thesis is as follows. Chapter 2 introduces the phase shift masking techniques used in semiconductor manufacturing lithography. This is followed by a brief discussion on the EUV mask absorber requirements and dielectric constant modeling.

In Chapter 3, we discuss an absorber identification technique through dielectric constant modeling and effective media approximation (EMA) model. A brief discussion on different types of EMA models is also provided. Using EMA, a variety of absorber candidates can be identified and engineered. Experimental validation results of the EMA model through thin-film deposition and ellipsometry in the UV-VIS-NearIR wavelengths is also presented.

In Chapter 4, mask absorber design optimization for attenuated phase shifting mask (attPSM) absorbers is discussed. A conceptual technique to identify attPSM absorber candidates through co-optimization of lithography metrics with the relative absorber reflectivity is introduced. Finally, index matched absorbers with high extinction coefficient are proposed as promising alternatives. Chapter 5 concludes this thesis.

2 Background

2.1 Phase Shift Masking

Phase shift masking (PSM) is a resolution enhancement technique that allows pattern transfer at sub-wavelength resolution [9], [80]–[82]. Conventional lithography masks such as chrome-on-glass masks used in DUV, and Ta-based absorber on Mo/Si mirror used in EUV are considered binary masks. An ideal binary mask has 100% transmission in clear areas of the mask and 0% transmission for absorbers. In a phase shifting mask, the absorbing media are replaced by a phase shifting layer that alters the amplitude and the phase of the transmitted light. Phase shifting concept is depicted in Figure 2.1 [8]. The light passing through a medium with refractive index n' and a thickness d will have a phase shift induced by a factor of ${2\pi}/{\lambda}$ $(n' \times d)$. Adding a phase shifter of thickness t and refractive index n'' in the optical path will introduce an additional phase shift of ${2\pi}/{\lambda}$ $(n'' \times t)$. In the example of Figure 2.1, the light exiting the medium with refractive index n'' is 180° out of phase with light exiting the medium n'.
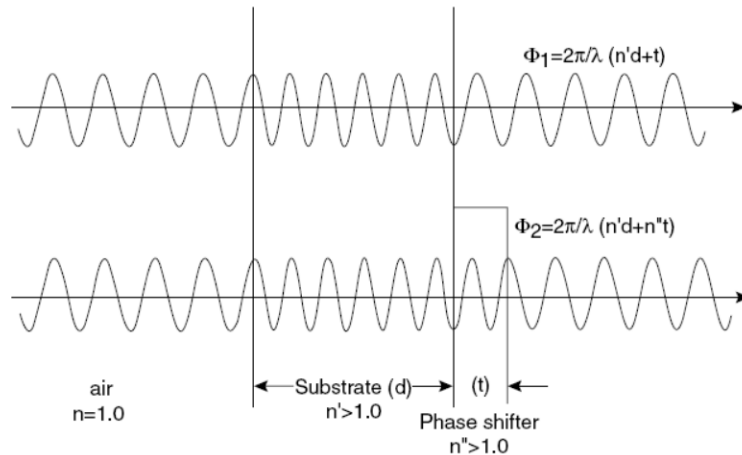
Figure 2.1: Phase shift masking concept. Phase shifter with thickness t and refractive index n'' adds an additional phase shift of $2\pi/\lambda$ $(n'' \times t)$.

By appropriately choosing the material thickness t and its corresponding refractive index, optimum phase shifters may be designed. For the conventional DUV lithography, the medium n' in Figure 2.1 may be imagined as the mask substrate and the medium n'' as the phase shifting absorber. The additional desired phase shift can be calculated using the Equation (2.1).

$$\Delta\emptyset = 2\pi t \left(\frac{n_{psm} - 1}{\lambda}\right) \tag{2.1}$$

As EUVL systems employ reflective optics, the light must make two passes through the phase shifter as depicted in Figure 2.2. In this case the generated phase shift can be calculated using the Equation (2.2).

$$\Delta\emptyset = 4\pi t \left(\frac{n_{psm} - 1}{\lambda}\right) \tag{2.2}$$
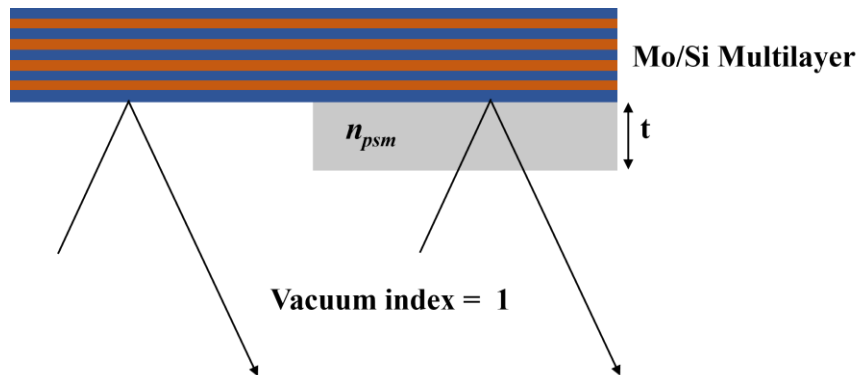
Figure 2.2: Phase shift masking concept for EUV lithography. Light makes two passes through the phase shifter.

2.1.1 Types of Phase Shift Masks

As previously mentioned, phase shift masking is a resolution enhancement technique. PSM increases the aerial image contrast through frequency doubling or edge enhancement technique. Many different approaches and mask designs have been proposed over the years to improve the imaging performance of lithography systems through phase

shift masking. Some of these phase shifting techniques are discussed briefly in the following sections.

Absorberless, or more traditionally known as chromeless, phase shift masks introduce a desired phase shift by adding or removing the mask material through semiconductor processing techniques [83]–[85]. The term absorberless is used as it can be applicable to EUVL reticles. Figure 2.3 shows the schematic of an absorberless phase shifting mask for optical DUV lithography. The etched material has a thickness corresponding to the desired phase shift. The aerial image intensity (red curve) is the square of the electric field with 2× frequency. Therefore, the absorberless phase shifting mask design offers resolution doubling. The pitch of the intensity of the aerial image is twice the mask pitch.
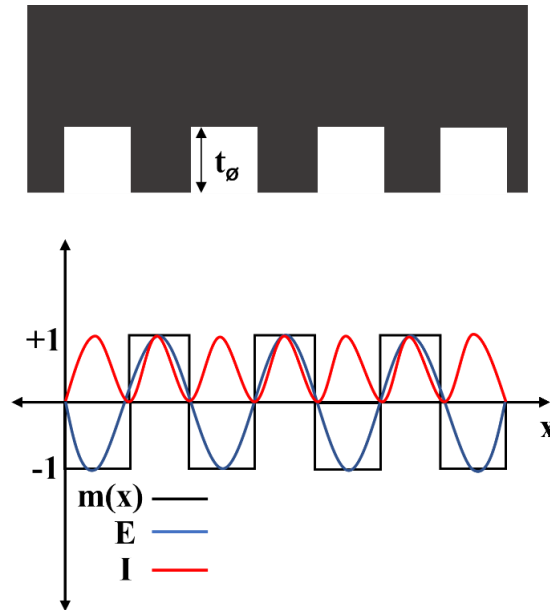
Figure 2.3: Schematic of absorberless (chromeless) phase shifting mask for DUV lithography.

For EUV reticles, the design is etched into the multilayer mirror as shown in Figure 2.4. The small EUV wavelength (13.5nm) is extremely sensitive to surface roughness and

defects. Challenging etch control is necessary to obtain a low defect mask pattern and to achieve a high CD uniformity. Due to processing limitations, such absorberless mask designs are impractical.
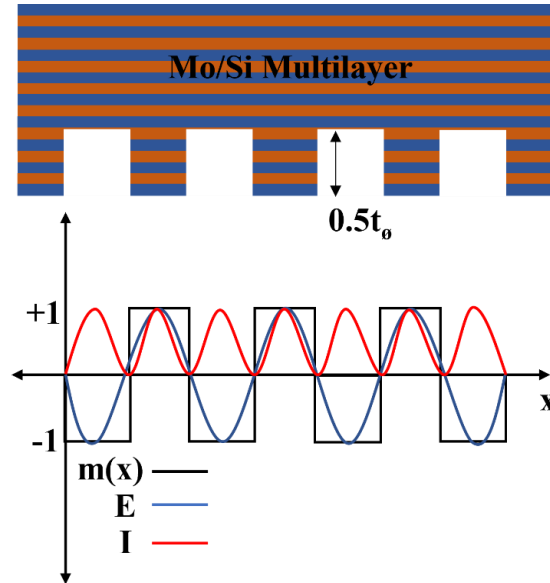
Figure 2.4: Schematic of absorberless phase shifting mask for a EUV lithography. The patterns are etched into the multilayer mirror.

2.1.1.2 Alternating PSM

Alternating phase shift mask designs employ a phase shifter and an absorber layer to introduce a phase shift between the nominally clear and dark regions to achieve frequency doubling [86]–[88]. The phase information in the case of an alternating phase shifting mask is modified by either adding or subtracting the optional phase shifting material corresponding to the desired phase shift (typically 180º or π for DUV). Alternating PSM designs achieved through etching (subtracting) in the substrate are sometimes referred to as strong alternating PSM.

For coherent illumination, the lens NA required to capture the diffracted orders is essentially half the NA necessary to capture the same number of diffracted orders produced by a conventional binary mask. Therefore, the resolution of the system is doubled alternating PSM is employed. Increasing the partial coherence factor diminishes the impact

26

of this phase shifting technique. Figure 2.5 shows the alternating PSM design for a DUV
lithography mask along with the generated electric field and aerial image intensity.
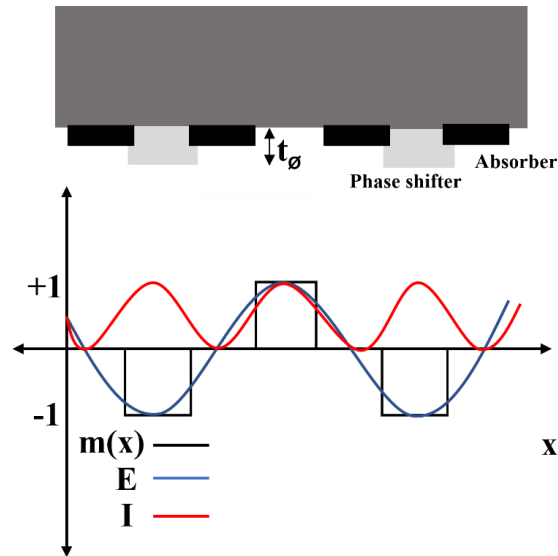
Figure 2.5: Schematic of alternating phase shifting mask for DUV lithography. The patterns are designed using a phase shifter and an absorber layer.

Figure 2.6 depicts the strong alternating phase shifting mask design and resulting
electric field and intensity responses for EUV lithography masks. Phase shift in this
example is achieved by a combination of etching into the multilayer and an absorber.
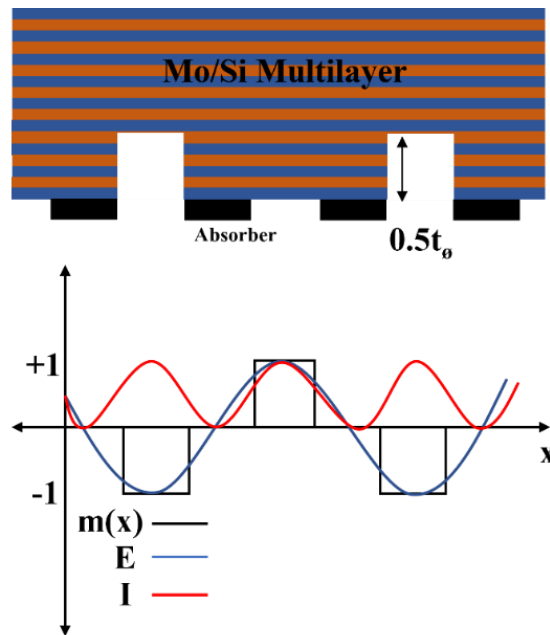
Figure 2.6: Schematic of alternating phase shifting mask for EUV lithography. The patterns are designed by etching into the multilayer mirror and an absorber layer.

Implementing alternating PSM technique for EUV lithography is challenging mainly because of the processing limitations for both, with and without the phase shifter. Additionally, complex alternating mask designs add to the existing M3D effects in EUV.

2.1.1.3   Attenuated PSM

Attenuated PSM improves the resolution of the lithography system by introducing an edge enhancement effect [26], [89]–[91]. Edge enhancement is achieved by employing an absorber layer with a small amount of transmission (reflectivity for EUVL). As shown in Figure 2.7, the electric field transitions from a positive electric field (+1) to a negative field with a phase shift. In the case where the electric field experiences loss of modulation, such as in a defocus condition, the squared intensity has a zero minimum due to the phase shift and electric field transition. Therefore, attenuated PSMs improve the depth of focus.
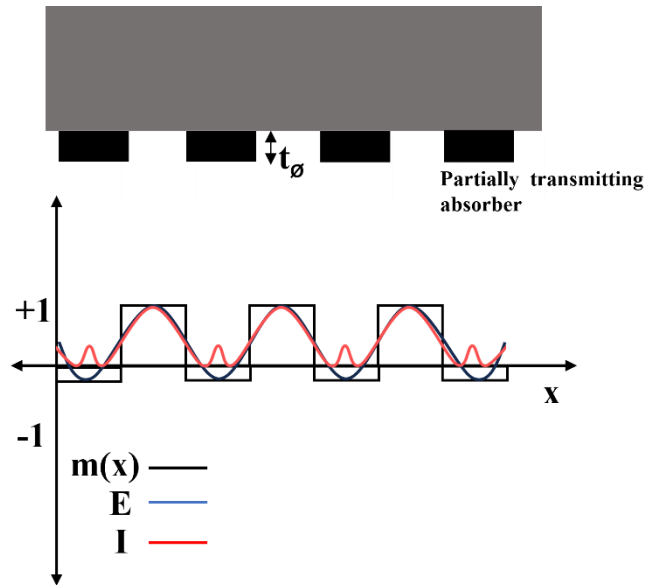
Figure 2.7: Schematic of attenuated phase shifting mask for DUV lithography. The patterns are designed using a partially transmitting absorber layer.

Typically, absorbers with 3-10% transmission are employed for DUV lithography. The phase shifted region has an intensity value corresponding to the transmission of the absorber material. The resist threshold is chosen such that the phase shifted electric field

28

does not print on wafer. In the case of EUV reticles, an attenuated phase shifting mask absorber is mounted on top of the multilayer mirror, as depicted in Figure 1.9. The resulting electric field and intensity distributions are similar to the DUV attPSM shown in Figure 2.7. The attPSM absorber thickness is a critical parameter in the mask design because of the inherent M3D effects associated with EUV, as discussed in section 1.6. However, larger phase shifts at smaller absorber thicknesses are possible as light travels twice through the absorber.

Other edge enhancement PSM techniques such as ridge or outrigger alternating PSM have similar patterning challenges as absorberless or alternating PSMs [92]. Attenuated PSMs are therefore the primary design choice for EUV reticles due to their processing simplicity.

2.2 Phase Shifting Mask Absorber

Phase shifting in EUVL can be obtained by selecting the absorber material with appropriate refractive index to obtain the desired optical performance. There are two main challenges in selecting an EUV attPSM absorber. First is identifying the materials that satisfy the complex refractive index requirement. The second challenge is determining the desired optical properties such as phase shift, mask reflectance, and thickness.

The phase shift and reflectivity requirements of an attPSM absorber influenced by factors including illumination conditions and layout design, can be translated to the absorber material properties using standard thin films theory [93]. The suitability of the elemental candidate materials can then be identified by an appropriate combination of the complex refractive index ($n - ik$) and the absorber thickness (d). Figure 2.8 plots a variety of materials using complex refractive index as $k - n$ plots [94]. While the complex

refractive index $(n - ik)$ influences both phase and mask absorber reflectivity, in this regime the influence of n on phase and k on reflectivity dominate, while lower n values lead to lower absorber thickness.

Figure 2.8: k – n plot for materials highlighting 5%, 10% and 15% transmission regions each with 180°, 200° and 220° phase shift zones (n & k values are obtained from CXRO database).

As few single component materials meet the necessary phase and reflectivity requirements, candidate attPSM absorbers are likely alloys and compounds. The resulting n & k of a composite material is dependent on the material stoichiometry. Any combination of n, k and d has an associated phase shift and absorber reflectivity that follows the relationships in Eqs. (2.3) and (2.4). Figure 2.8 also shows this relationship with 5%, 10% and, 15% reflectivity regions, and phase shift zones within each for 180°, 200° and, 220°. The choice of appropriate phase shift may be more than 180° for EUVL to compensate for the M3D effects. For example, an MoPt alloy at $n = 0.9083$, $k = 0.0317$ and $d = 42$nm will provide a phase shift $(\Delta\emptyset) = 206°$ at source wavelength $(\lambda) = 13.5$nm and, illumination angle $(\theta) = 6°$. The overall absorber reflectivity or transmission function (T) normalized to the mask blank reflectivity is 8.2%. R is the reflection function of the alloy. The design

considerations including phase shift and absorber reflectivity for attPSM absorbers are discussed in detail in Chapter 4.

$$\Delta\emptyset = \frac{4\pi d}{\lambda cos\Theta}(1-n) \tag{2.3}$$

$$k = \frac{\ln\left(\frac{1-R}{T}\right)}{2\Delta\emptyset}(n-1) \tag{2.4}$$

Apart from the attPSM absorbers, high $-k$ and index matched ($n \approx 1$) absorbers are also alternative absorber candidates for EUVL masks. High $- k$ and index matched absorbers are binary absorbers similar to the currently employed Ta-based absorbers. High $- k$ mask absorbers are single element metals or a composite with a high extinction coefficient that provide enhanced light absorption at lower absorber thickness. Index matched absorbers on the other hand have high refractive index (n close to 1). Design considerations of index matched absorbers with high extinction coefficient (high n – high k) are also discussed in Chapter 4.

2.3 Dielectric Constant Modeling

As previously mentioned, due to the optical properties of most materials at 13.5nm wavelength, the absorber material is most likely an alloy or a compound. It is more intuitive to describe composite materials in terms of their complex dielectric constant (ε) rather than the refractive index (n) and extinction coefficient (k). The dielectric constant is also known as the relative permittivity of the medium. The dielectric constant of a material is given in Eq. (2.5) [42], where D is the displacement vector and E is the external electric field.

$$D = \varepsilon E \tag{2.5}$$

When a dielectric medium encounters an external electric field E, the charged particles are displaced from their equilibrium position. This results in electric dipoles. The

act of producing electric dipoles is called polarization (P). The polarization of a material is the average number of dipole moments per unit volume and is given in Eq. (2.6), where p are dipole moments, V is volume and N is the number of charged particles (atoms/ molecules) per unit volume.

$$P = \frac{p}{V} = Np \tag{2.6}$$

The dipole moments (p) are directly proportional to the local electric field (E`) and the proportionality constant α in Eq. (2.7) is called the polarizability of the particle. Therefore, the total polarization of a dielectric material containing N particles is given by Eq. (2.8).

$$p = \alpha E` \tag{2.7}$$

$$P = N\alpha E` \tag{2.8}$$

The local electric field E` can be calculated as the sum of the external electric field and electric field of other dipoles and can be given as:

$$E` = E + \frac{P}{3\varepsilon_0} \tag{2.9}$$

The displacement vector D can also be defined as:

$$D = \varepsilon_0 E + P \tag{2.10}$$

where, ε_0 is the permittivity of free space and therefore, using Eq. (2.5) and (2.10),

$$\varepsilon E = \varepsilon_0 E + P \tag{2.11}$$

$$\varepsilon_0 \varepsilon_r E = \varepsilon_0 E + P \tag{2.12}$$

$$P = \varepsilon_0 (\varepsilon_r - 1) E \tag{2.13}$$

From Eq. (2.8) and Eq. (2.9),

$$P = N\alpha \left(E + \frac{P}{3\varepsilon_0} \right) \tag{2.14}$$

$$P = N\alpha E + N\alpha \frac{P}{3\varepsilon_0} \tag{2.15}$$

$$N\alpha E = P\left(1 - \frac{N\alpha}{3\varepsilon_0}\right) \tag{2.16}$$

$$P = \frac{N\alpha E}{1 - \frac{N\alpha}{3\varepsilon_0}} \tag{2.17}$$

Substituting P from Eq. (2.13),

$$\varepsilon_0(\varepsilon_r - 1)E = \frac{N\alpha E}{1 - \frac{N\alpha}{3\varepsilon_0}} \tag{2.18}$$

Simplifying the above equation yields the Clausius-Mossotti relationship in Eq. (2.19). The Clausius-Mossotti relationship relates the microscopic property polarizability (α) of a material to its macroscopic counterpart using the dielectric constant [95].

$$\frac{\varepsilon_r - 1}{\varepsilon_r + 2} = \frac{N\alpha}{3\varepsilon_0} \tag{2.19}$$

2.3.1 Lorentz Oscillator Model

The Lorentz oscillator model is a dipole oscillator model which is used to calculate the frequency (or wavelength) dependence of the refractive index and the absorption coefficient [96]. In the simplest form, a Lorentz oscillator can be visualized using the mass on a spring model such as shown in Figure 2.9. A mass is suspended to a rigid support using a spring and a damper. When an external force is applied, the mass would oscillate and eventually return to equilibrium because of the damper. This is analogous to an atomic model where the electron (electron cloud) is bound to the nucleus due to the electrostatic attraction as depicted in Figure 2.10. An external electric field (external force) will stretch the electron and the nucleus away from each other. Since the mass of the nucleus is

significantly larger than the electron mass, we assume that the nucleus acts as the rigid support. Therefore, an oscillating electric field will result in an oscillating electron displacement.
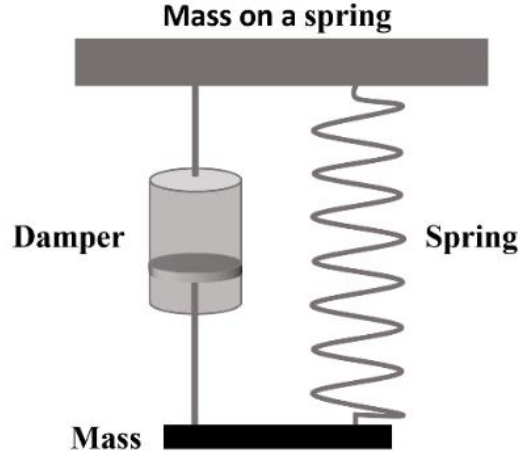
Figure 2.9: Mass on a spring model illustrating Lorentz oscillator model for dielectrics.

The mass on a spring model can be mathematically represented by the equation of motion that determines the displacement of an electron. The displacement x of an electron takes the form:

$$m_0 \frac{dx^2}{dt^2} + m_0 \gamma \frac{dx}{dt} + m_0 \omega_0^2 x = -eE \qquad (2.20)$$

where E is the electric field, m_0 is the electron mass, $-e$ is the charge on the electron and γ is the damping rate. The first term in Eq. (2.20) is the acceleration force. The second term is the frictional force that determines the loss of the system [95]. The damping factor models the loss of energy of oscillating dipoles due to collision. The final term is the restoring force that represents the force of the spring or the electrostatic attraction. The restoring force is a resonant phenomenon and hence the variable $(\omega_0)^2$, which is the resonant frequency given in Eq. (2.21), where K is the spring constant.

$$\omega_0 = \sqrt{\frac{K}{m_0}} \qquad (2.21)$$
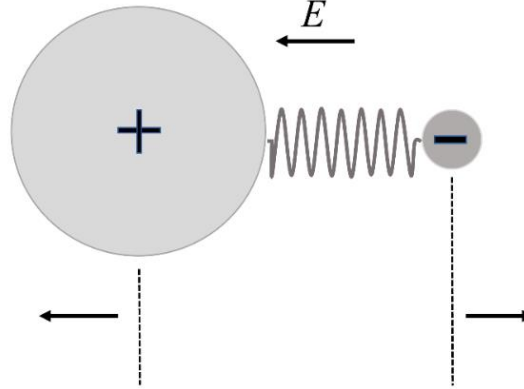
Figure 2.10: Atomic model representation using mass on a spring model in Figure 2.9.

The right-hand side of the Eq. (2.20) is the driving force, which is essentially the Lorentz force law. Here, the electric field E is time-dependent with the angular frequency ω. This can be represented as:

$$E(t) = E_0 \cos(\omega t + \phi) = E_0 \, Re\big(e^{-i(\omega t + \phi)}\big) \qquad (2.22)$$

The dipole oscillations will follow the frequency of the electric field and therefore, the time dependence of the displacement will be of the from:

$$x(t) = X_0 \, Re\big(e^{-i(\omega t + \phi')}\big) \qquad (2.23)$$

By allowing E_0 and X_0 to be complex numbers, we can incorporate the phase factors of Eq. (2.22) and Eq. (2.23) into the amplitudes. Then substituting $E(t) = E_0 e^{-i\omega t}$ in Eq. (2.20) and solving for X_0 gives:

$$X_0 = \frac{-eE/m_0}{\omega_0^2 - \omega^2 - i\gamma\omega} \qquad (2.24)$$

The time varying oscillations produce time varying dipole moments $p(t)$. On a macroscopic level, the resonant polarization can be calculated using Eq. (2.6) as:

$$P = Np = -Nex \tag{2.25}$$

$$P = \frac{Ne^2}{m_0} \frac{E}{(\omega_0^2 - \omega^2 - i\gamma\omega)} \tag{2.26}$$

From Eq. (2.10) for D, we can separate the term P into resonant frequency polarization from Eq. (2.26) and background polarization such as:

$$D = \varepsilon_0 E + P_{bk} + P_{res} \tag{2.27}$$

$$D = \varepsilon_0 E + P_{bk} + P_{res} \tag{2.28}$$

By combining Equations (2.10), (2.19) and (2.28), we can solve for relative permeability as:

$$\varepsilon_r(\omega) = 1 + \chi + \frac{Ne^2}{\varepsilon_0 m_0} \frac{1}{(\omega_0^2 - \omega^2 - i\gamma\omega)} \tag{2.29}$$

where χ is the electrical susceptibility of the dielectric material that dictates how easily a dielectric material can be polarized in the presence of an electric field. We can separate Eq. (2.29) into real and imaginary parts to obtain the real (ε_1) and imaginary (ε_2) parts of the dielectric constant as:

$$\varepsilon_1(\omega) = 1 + \chi + \frac{Ne^2}{\varepsilon_0 m_0} \frac{\omega_0^2 - \omega^2}{(\omega_0^2 - \omega^2)^2 + (\gamma\omega)^2} \tag{2.30}$$

$$\varepsilon_2(\omega) = \frac{Ne^2}{\varepsilon_0 m_0} \frac{\gamma\omega}{(\omega_0^2 - \omega^2)^2 + (\gamma\omega)^2} \tag{2.31}$$

In practice, a material has multiple resonant frequencies ω_k. The total polarization of the material and therefore, the relative dielectric constant is then given by Eq. (2.32) and (2.33), respectively. The relative dielectric constant in Eq. (2.33) accounts for all the transitions in the material. This enables calculating the dielectric constant through the entire frequency (and wavelength) spectrum.

$$P = \left(\frac{Ne^2}{m_0} \sum_k \frac{1}{(\omega_k^2 - \omega^2 - i\gamma_k\omega)} \right) E \qquad (2.32)$$

$$\varepsilon_r(\omega) = 1 + \frac{Ne^2}{\varepsilon_0 m_0} \sum_k \frac{1}{(\omega_k^2 - \omega^2 - i\gamma_k\omega)} \qquad (2.33)$$

2.3.2 The Drude Model

Metals and doped semiconductors possess a high number of free electrons. These electrons that are not bound to any atom do not experience any restoring force in Eq. (2.20). Therefore, the spring constant is 0 and hence, the resonant frequency (ω_0) in Eq. (2.20) is 0. This free electron model was first introduced by Paul Drude [97] and the dipole oscillator model that can be used to model dielectric constant in metals is called the Drude-Lorentz model. By setting the $\omega_0 = 0$, the model is reduced to Eq. (2.34), where ω_p^2 is the plasma frequency and τ is the mean collision rate.

$$\varepsilon_r(\omega) = 1 - \frac{\omega_p^2}{\omega^2 + i\omega\tau^{-1}} \qquad (2.34)$$

where,

$$\omega_p^2 = \frac{Ne^2}{\varepsilon_0 m_0} \qquad and \qquad \tau = \frac{1}{\gamma} \qquad (2.35)$$

2.3.3 The Kramers-Kronig Relationship

The Kramers-Kronig relationship shows that the real and imaginary parts of a real physical linear system are related [98], [99]. Since the dipole oscillator models discussed in the sections above are real physical systems with causal relationship, we can use Kramer-Kronig relations to derive the relationship between the real and the imaginary parts of the

dielectric constant and hence, the complex refractive index. The Kramers-Kronig relationships are given in Eq. (2.36) & (2.37), where *P* is the principal part of the integral.

$$n(\omega) = 1 + \frac{2}{\pi} P \int_0^\infty \frac{\omega' k(\omega')}{\omega'^2 - \omega^2} d\omega' \tag{2.36}$$

$$k(\omega) = -\frac{2}{\pi\omega} P \int_0^\infty \frac{\omega'^2 [n(\omega') - 1]}{\omega'^2 - \omega^2} d\omega' \tag{2.37}$$

This relationship is useful in determining the frequency (and wavelength) dependence of the optical properties of a material. If one is known over a large (infinite) frequency range, then the other can be calculated from it. This principle is applied in ellipsometry measurement techniques to obtain a precise and unique solution when determining the *n* & *k* of the sample under investigation.

3 Absorber Material Identification and Modeling

Since identifying novel absorber candidates is a two-fold challenge, we employ an approach where we first identify the materials that can satisfy the mask absorber requirements using dielectric constant modeling and the Effective Media approximation model [100]. The absorber design is considered in Chapter 4.

3.1 Effective Media Models

The complex dielectric constant (ε) can also be defined in terms of refractive index (n) and extinction coefficient (k) as given in Eq. (3.1). A heterogeneous material, obtained by mixing two or more homogeneous materials, will have an effective dielectric constant (ε_{eff}) that lies in a region (Ω) defined by dielectric constants of the homogeneous constituents and the material stoichiometry. This assumption is only true if the characteristic dimensions of the structure are small by approximately $1/10^{th}$ of the wavelength of the incident light.

$$\varepsilon = (n + ik)^2 \tag{3.1}$$

Individual layers in a periodic multilayer coating, such as employed in EUVL systems, have thickness smaller than the 13.5nm source wavelength. In case of a binary (two material) multilayer system, the effective dielectric constant $\left(\varepsilon_{eff}\right)$ is bound by the dielectric constants ε_1 and ε_2 of the constituent elements and their fractional volumes f_1 and $f_2 = 1 - f_1$ within the composite. This region (Ω) as shown in Figure 3.1 is known as Wiener bounds [101], named after Otto Wiener, who first introduced the ideal extreme bounds on the effective dielectric constants of material combination for all volume

fractions. The two bounds ($\varepsilon_\perp$ and $\varepsilon_\parallel$), derived from Eqs. (3.2) and (3.3) are the dielectric response of the material to the incident beam of light with its electric field vector perpendicular and parallel to the boundary of the structure, respectively [102].

$$\frac{1}{\varepsilon_\perp} = \frac{f_1}{\varepsilon_1} + \frac{f_2}{\varepsilon_2} \tag{3.2}$$

$$\varepsilon_\parallel = f_1\varepsilon_1 + f_2\varepsilon_2 \tag{3.3}$$

This means that any combination of two arbitrary materials with respective dielectric constants (ε_1 & ε_2) as shown in Fig. 3.1 will have any effective dielectric constant in the Ω region. Therefore, 100% volume of material with dielectric constant ε_1 will result in an effective dielectric constant $\varepsilon_{eff} = \varepsilon_1$. Similarly, 100% volume of material with dielectric constant ε_2 will result in an effective dielectric constant $\varepsilon_{eff} = \varepsilon_2$.
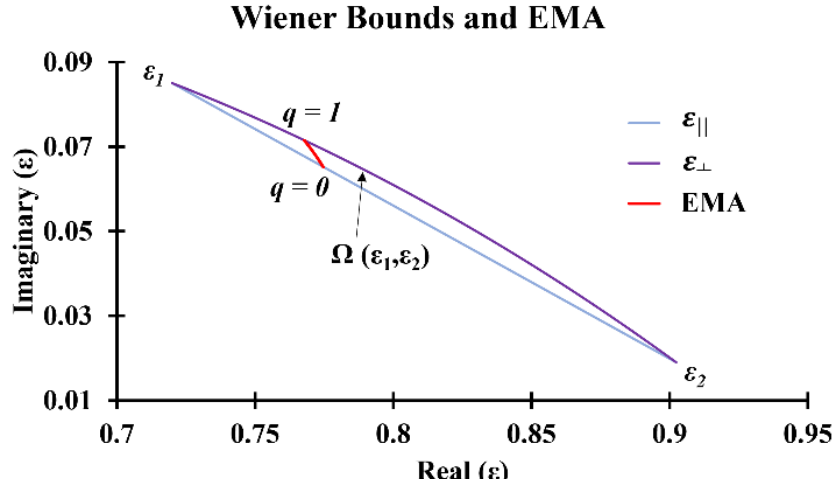
Figure 3.1: Example of Wiener bounds of two materials with arbitrary complex dielectric constants and, the EMA model for the fill fractions of $f_1 = 0.7$ and $f_2 = 1 - f_1 = 0.3$.

3.1.1 Maxwell-Garnett Model

While the effective dielectric constant of any arbitrary mixture of materials will lie in the space defined by Wiener bounds, they are only useful to identify the region of the dielectric constant (or $k-n$) spectrum. Effective medium models are then used to determine a specific ε_{eff} value for material combinations under consideration. The choice of the

40

effective media approximation model is dependent on the material combination and geometry. The two most used models are the Maxwell – Garnett [103] and the Bruggeman [104] effective media theories.

The Maxwell – Garnett model assumes that the elemental loading mediums with respective dielectric constants $(\varepsilon_2, \varepsilon_3, \ldots \varepsilon_n)$ are restrained within a separate host medium (ε_1). This model is applied when the nanomaterials are sparsely dispersed, and material interaction is limited. Therefore, this model is more appropriate when the loading materials have low fill fractions (i.e. $f_1 \gg f_2, f_3, \ldots, f_n$). The solution to the Maxwell – Garnett model is given in Eq. (3.4), where $f_1 + f_2 + f_3 + \ldots + f_n = 1$.

$$\frac{\varepsilon_{MG} - \varepsilon_1}{\varepsilon_{MG} + \varepsilon_1} = f_2 \frac{\varepsilon_2 - \varepsilon_1}{\varepsilon_2 + 2\varepsilon_1} + f_3 \frac{\varepsilon_3 - \varepsilon_1}{\varepsilon_3 + 2\varepsilon_1} + \cdots + f_n \frac{\varepsilon_n - \varepsilon_1}{\varepsilon_n + 2\varepsilon_1} \qquad (3.4)$$

3.1.2 Bruggeman Model

The Bruggeman model is more accurate when the fill fractions of the loading mediums are higher. It can be considered as a dense case of the Maxwell-Garnett approach. The Bruggeman model is self-consistent in the sense that it assumes the host medium as an elemental constituent equivalent to the loading mediums. Solving Eq. (3.5) provides the effective dielectric constant using the Bruggeman approach [105].

$$f_1 \frac{\varepsilon_1 - \varepsilon_B}{\varepsilon_1 + 2\varepsilon_B} + f_2 \frac{\varepsilon_2 - \varepsilon_B}{\varepsilon_2 + 2\varepsilon_B} + f_3 \frac{\varepsilon_3 - \varepsilon_B}{\varepsilon_3 + 2\varepsilon_B} + \cdots + f_n \frac{\varepsilon_n - \varepsilon_B}{\varepsilon_n + 2\varepsilon_B} = 0 \qquad (3.5)$$

3.1.3 Effective Media Approximation Model

The Effective Media Approximation (EMA) model introduced by D.E. Aspnes [106]–[108] combines the Maxwell – Garnett and the Bruggeman approaches by

incorporating a material depolarization factor (q). The ε_{eff} using the EMA approach can be determined using the Eq. (3.6).

$$\varepsilon_{eff} = \frac{\varepsilon_1 \varepsilon_2 + \bar{\varepsilon}(f_1 \varepsilon_1 + f_2 \varepsilon_2)}{\bar{\varepsilon} + (f_1 \varepsilon_2 + f_2 \varepsilon_1)} \tag{3.6}$$

where,

$$\bar{\varepsilon} = \frac{(1-q)\varepsilon_{host}}{q} \tag{3.7}$$

The effective dielectric constant modeled using the EMA model accounts for the dielectric behavior of the surrounding medium on the suspended nanoparticles of the loading medium through $\bar{\varepsilon}$ in Eq. (3.7). The term $(1-q)/q$ is the depolarization parameter, and it depends on the shape and orientation of the nanoparticles in the composite. Here, q is the depolarization factor and ε_{host} can either be ε_1 or ε_2 depending on the host and loading mediums. In the case of perfect mixing of spherical nanoparticles is three-dimensions, the q factor assumes the value of 1/3 and depolarization parameter becomes 2. This is also seen in the denominator of the Maxwell – Garnett and Bruggeman models, as well as in the Clausius – Mossotti equation that explains the relationship between the dielectric constant and the polarizability of the constituent nanoparticles [109].

An example of the EMA model for two arbitrary materials with volume fractions, $f_1 = 0.7$ and $f_2 = 0.3$ is shown in Figure 3.1 using the red line. The EMA model is within the Wiener bounds. Constituent complex dielectric constants (ε_1 & ε_2) at the two extremes of the Wiener bounds are realized as the ε_{eff} when either volume fractions, f_1 or $f_2 = 1$, respectively. The depolarization factor q ranges from 0 to 1. When $q = 0$, the ε_{eff} value falls on the $\varepsilon_{\parallel}$ line whereas for $q = 1$, the ε_{eff} assumes a value on the $\varepsilon_{\perp}$ line. The effective

dielectric constants of all the candidate absorber materials in this study are modeled using the EMA approach.

3.2 Material Modeling

Typically, materials employed in an EUV mask are selected based on their optical properties, specifically the *n* and *k*. As we are interested in the dielectric response of materials, we use the complex dielectric constant space by translating the *k-n* plots such as shown in Figure 2.2 using the relationship from Eq. (3.1). This is shown in Figure 3.2, which plots the materials (and material combinations) in the complex dielectric constant spectrum. It also shows the six binary (composed of two elements) refractory alloy systems connected through dotted lines specifically, the Ru-Te, Mo-Ni, Rh-Ta, Mo-Pt, Pt-Ti and the Rh-Ti [100].
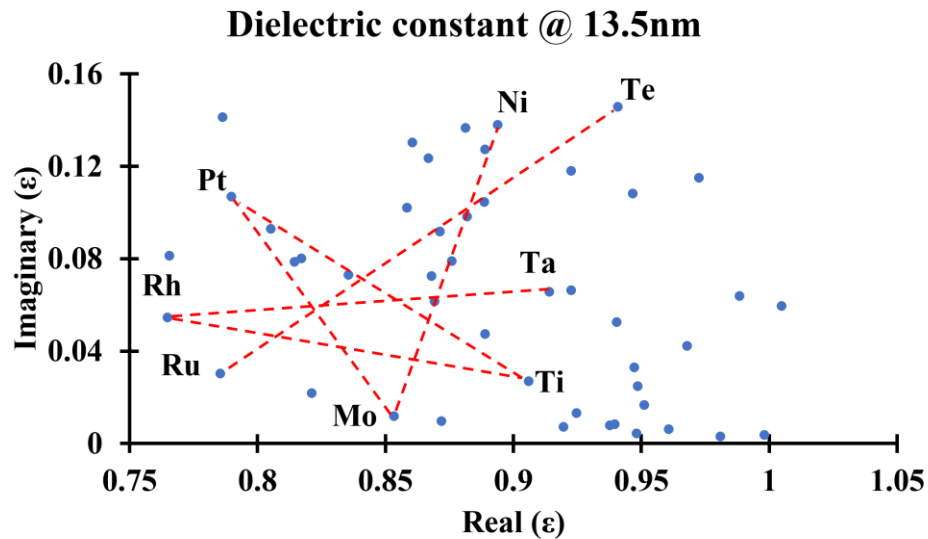
Figure 3.2: Selected material systems in the real and imaginary dielectric constant ($\varepsilon_r - \varepsilon_k$) space. Dotted red lines indicate selected metal systems.

The refractory metal elements are chosen such that they cover a large area of the mask absorber spectrum. Materials elements such as Ru, Rh and Pt are chosen to explore the low refractive index materials (low − *n*) absorber candidates. Materials with low

refractive index can exhibit phase shifting properties. Materials with high absorption at 13.5nm wavelength such Ni and Te are also selected to explore high extinction coefficient (high – k) mask absorbers candidates. Any combination of selected materials will have an effective dielectric constant in this region of interest and therefore, can be categorized as an EUV mask absorber.

EUV light at 13.5nm wavelength has high energy photons. Mask stacks illuminated with a large number of high energy photons may experience elevated operating temperatures. Heating specification also needs consideration while selecting mask absorber candidates. Material compositions that can sustain sufficiently high operating temperature without experiencing a phase change are therefore desired. The material systems chosen are adopted with thermal stability under consideration. Using the thermodynamic phase diagrams for binary-material systems [110], single phase stable alloys are selected with some systems having more than one candidate alloy. Table 3.1 lists the nine alloys chosen, along with their respective weight fractions (%wt.), volume fractions (%vol.) and thermal stability of the composition. Amorphous morphology is ideally desired for absorbers to keep the line edge roughness to a minimum. The kinetics of formation energy and morphology are not analyzed.

Fractional volumes required for Wiener bounds and the EMA model are calculated using the fractional weight and theoretical material density. The upper limit on operating temperature is 150 °C after which the Mo/Si multilayer mirror experiences intermixing [111]. All material combinations can operate at sufficiently high temperatures with $RuTe_2$ alloy having the lowest thermal stability at approximately 470 °C, where it experiences a phase change from the α solid phase to β solid phase.

Table 3.1: Alloy compositions are selected from six binary materials systems under consideration with respective weight fraction (% wt.), volume fraction (% vol.) and thermal stability (°C).

Material Composition	% wt.	% vol.		Thermally stability
		f_1	f_2	
$RuTe_2$	72% Te	16.4% Ru	83.6% Te	~ 470 °C
MoNi	37% Ni	59.6% Mo	40.4% Ni	~ 870 °C
$MoNi_4$	69% Ni	28.0% Mo	72.0% Ni	~ 1360 °C
PtTi	19% Ti	47.2% Pt	52.8% Ti	~ 1500 °C
$PtTi_3$	45% Ti	20.4% Pt	79.6% Ti	~ 1035 °C
Rh_3Ta	35% Ta	71.3% Rh	28.7% Ta	~ 2000 °C
MoPt	65% Pt	52.9% Mo	47.1% Pt	~ 1300 °C
$MoPt_2$	79% Pt	35.7% Mo	64.3% Pt	~ 1800 °C
Rh_5Ti	9% Ti	78.5% Rh	21.5% Ti	~ 1100 °C
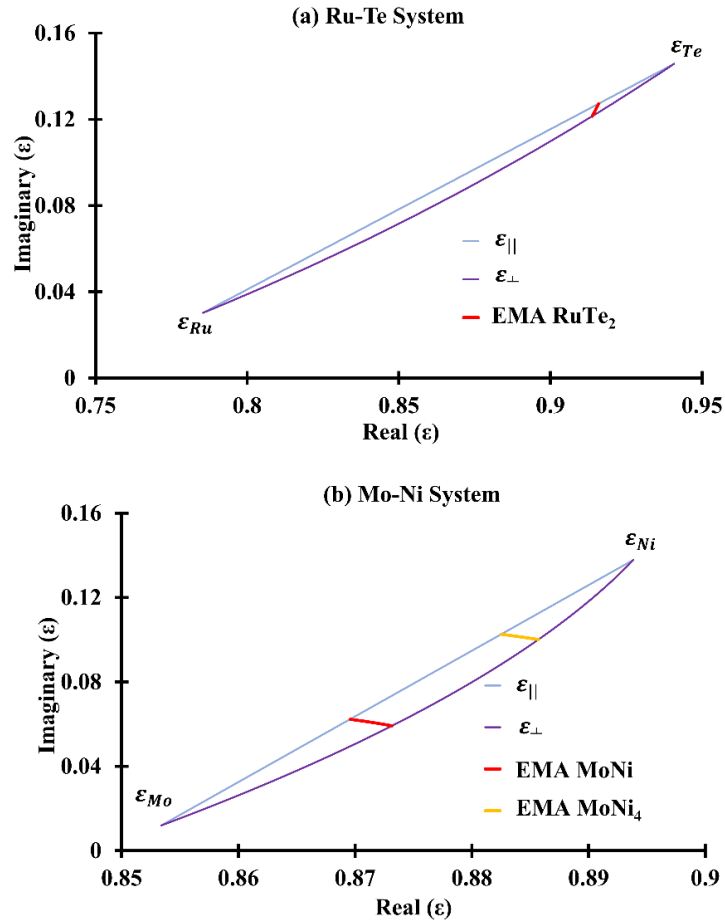
Figure 3.3: Wiener bounds for material system (a) Ru-Te, and (b) Mo-Ni. EMA models of $RuTe_2$, MoNi and $MoNi_4$ are also shown. $RuTe_2$ and $MoNi_4$ are high-k absorber candidates.

The Wiener bounds of Ru-Te and Mo-Ni material systems are shown in Figure 3.3(a) and 3.3(b), respectively. Material composites $RuTe_2$ and $MoNi_4$ have high extinction coefficient and are therefore high $- k$ mask absorber candidates. EMA models for these two absorber candidates are shown in the respective figures. The EMA modeled effective dielectric constants and refractive indices for high $- k$ absorber candidates are listed in Table 3.2.

Table 3.2: Complex effective dielectric constant (ε_{eff}) and complex refractive index of high-k absorber candidates using effective media approximation modeling (EMA) at q factor of 1/3.

Material Composition	Dielectric constant		Refractive index	
	ε_r	ε_k	n	k
$RuTe_2$	0.9152	0.1252	0.9588	0.0653
$MoNi_4$	0.8836	0.1017	0.9415	0.0540

Material combinations MoNi, PtTi and $PtTi_3$ are low $- k$ materials with relatively high refractive index. The EMA model for MoNi is shown in Figure 3.3(b). The Wiener bounds and the EMA models of absorber candidates from the Pt-Ti systems are shown in Figure 3.4. The modeled optical constants of the high $n -$ low k materials from the Mo-Ni and the Pt-Ti material systems are listed in Table 3.3.
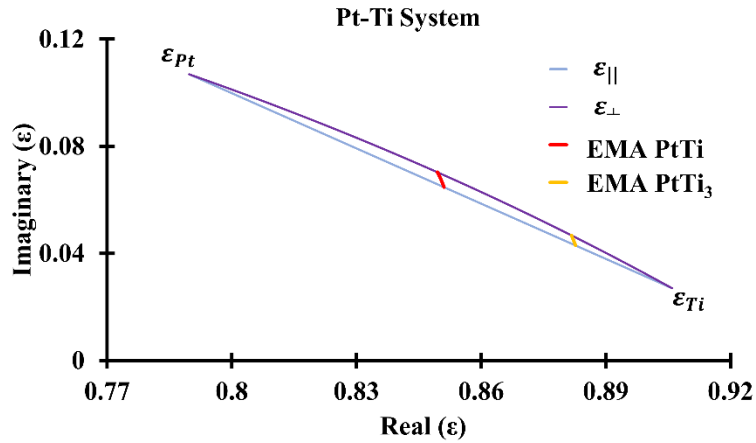
Figure 3.4: Wiener bounds of the Pt-Ti material system. EMA models for PtTi and $PtTi_3$ are also highlighted.

Table 3.3: Complex effective dielectric constant (ε_{eff}) and complex refractive index of low k – high n absorber candidates using EMA modeling at q factor of 1/3.

Material Composition	Dielectric constant		Refractive index	
	ε_r	ε_k	n	k
MoNi	0.8708	0.0612	0.9337	0.0328
PtTi	0.8505	0.0666	0.9229	0.0361
PtTi$_3$	0.8824	0.0442	0.9396	0.0235

Absorber candidates from the Rh-Ti, Rh-Ta and the Mo-Pt systems have a low refractive index with low extinction coefficient. The Wiener bounds of these three binary systems and the EMA models of the absorber candidates are plotted in Fig. 3.5(a) – (c), respectively. The corresponding optical constants are listed in Table 3.4.

The theorical bounds on the ε_{eff} at 13.5nm EUV wavelength are narrow due to the proximity of the dielectric constants (and refractive indices) of all the constituent elements. This limits the range of the ε_{eff} values for alloys within a given system. In the case of constituent elements with complex dielectric constant values even closer, the effective dielectric constant exhibits a linear relationship to the volumetric composition, as seen for Rh – Ta system in Fig. 3.5(b), where the $\varepsilon_\perp$ and $\varepsilon_{||}$ bounds completely overlap each other.

Table 3.4: Complex effective dielectric constant (ε_{eff}) and complex refractive index of low n – low k absorber candidates using effective media approximation modelling (EMA) at q factor of 1/3.

Material Composition	Dielectric constant		Refractive index	
	ε_r	ε_k	n	k
Rh$_5$Ti	0.7938	0.0492	0.8914	0.0276
Rh$_3$Ta	0.8057	0.0575	0.8982	0.0320
MoPt	0.8240	0.0577	0.9083	0.0317
MoPt$_2$	0.8128	0.0741	0.9025	0.0410

The material composites listed in Table 3.4 have low refractive indices. These materials can generate high phase shifts with high mask absorber reflectivity at low absorber thickness values.
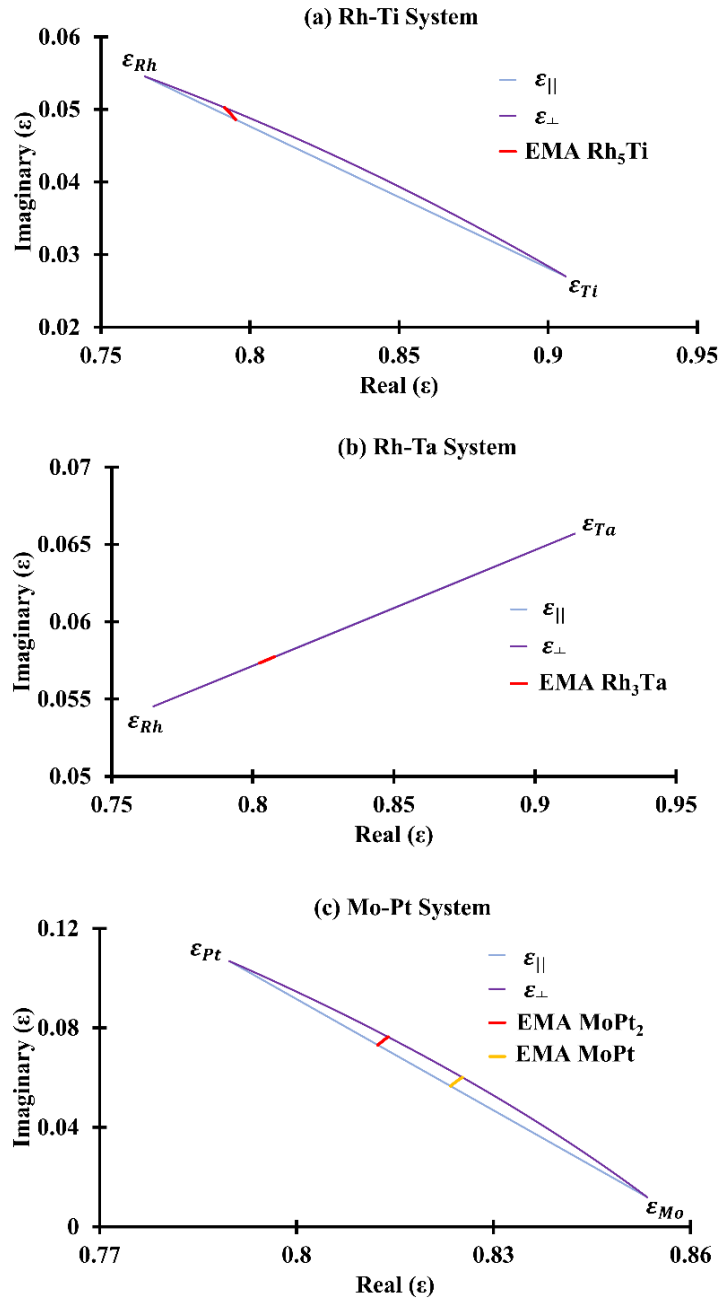
Figure 3.5: Wiener bounds of (a) Rh-Ti, (b) Rh-Ta, (c) Mo-Pt. EMA models for Rh$_5$Ti, Rh$_3$Ta, MoPt and MoPt$_2$ are also highlighted in respective figures.

3.3 Engineering Absorber Candidates

EMA modeling of composites is not only limited to alloys such as mentioned in section 3.2. Based on the stoichiometry of the composite in each material system, the optical constants for the absorber candidates can be engineered [112]. This is shown in Figure 3.6 which plots the Wiener Bounds and the EMA models for the Rh-Ti system. Four material combinations are identified, specifically at 21.5%, 29%, 56.5%, and 72% volume fractions of Ti.
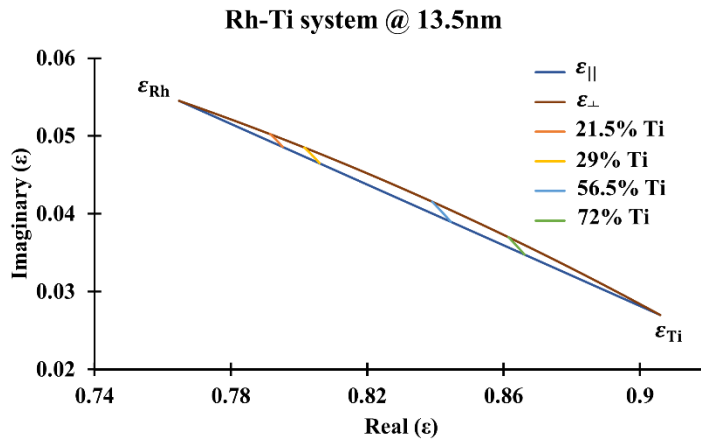
Figure 3.6: Wiener Bounds and EMA models of absorber composites from the Rh-Ti system. The EMA models are calculated at 21.5%, 29%, 56.5%, and 72% volume fractions of Ti.

The values of the optical constants vary as a function of the volume fraction of Ti (and Rh). The effective dielectric constants and the respective refractive indices calculated at $q = 1/3$ are listed in Table 3.5. Increasing the volume of Ti increases the refractive index of composite while the extinction coefficient reduces.

Table 3.5: Effective dielectric constants and refractive indices of the EMA modeled Rh – Ti composites.

	Composition	Dielectric constant		Refractive index	
Index	(%Ti)	ε_r	ε_k	n	k
(a)	21.5%	0.7938	0.0492	0.8914	0.0276
(b)	29%	0.8044	0.0472	0.8972	0.0263
(c)	56.5%	0.8426	0.0399	0.9182	0.0213
(d)	72%	0.8645	0.0355	0.9300	0.0191

Similarly, material composites from the Mo-Pt material system are also modeled through dielectric constant modeling and the effective media approximation model. The Wiener bounds and the EMA models from the Mo-Pt material system are shown in Figure 3.7. Similar to the Rh-Ti system, four material combinations have been identified. The corresponding effective dielectric constants and refractive indices of the absorber candidates from the Mo-Pt system are listed in Table 3.6 as a function of %volume of Pt. Increasing the volume of Pt leads to composites with low refractive indices and high extinction coefficients.
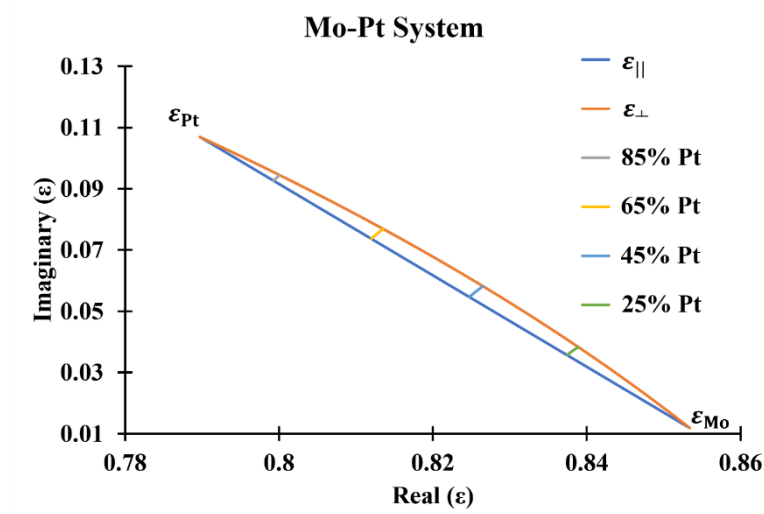
Figure 3.7: Wiener Bounds and EMA models of composites from the Mo-Pt system. The EMA models are calculated at 25%, 45%, 65%, and 85% volume fractions of Pt.

Table 3.6: Effective dielectric constants and refractive indices of the EMA modeled Mo – Pt composites.

Index	Composition (%Pt)	Dielectric constant		Refractive index	
		ε_r	ε_k	n	k
(a)	25%	0.8378	0.0365	0.9155	0.0199
(b)	45%	0.8252	0.0558	0.9089	0.0306
(c)	65%	0.8124	0.0747	0.9023	0.0413
(d)	85%	0.7995	0.0932	0.8956	0.052

3.4 EMA Model Verification

The EMA model is an approximate model that estimates the optical constants of a composite. As mentioned earlier, the EMA model is valid if the individual thin films in the composite are less than or equal to approximately 1/10th of the incident wavelength. Therefore, the EMA model employed can be validated in the UV-VIS-NearIR wavelength range. In this study, an inspection wavelength of 800nm is chosen as it is roughly at the center of the measurement spectrum. Therefore, the individual thin film thickness in a multilayer setting cannot exceed 80nm. Three material systems are used for verification, specifically the Mo-Ni, Mo-W and the Al-Ni. The Al target contains 1% Si. Physical vapor deposition (sputtering) systems are used to deposit multilayer thin films on a silicon substrate. These material systems are chosen primarily due to the availability of the sputter targets at RIT. The optical constants of the deposited thin films are measured using ellipsometry.

3.4.1 Multilayer Deposition

The multilayer samples from the three material systems are deposited using two different sputter systems. Multilayer composites from the Mo-Ni material system are deposited using a Kurt J. Lesker PVD-75B RF magnetron sputtering system at RIT Nano Power Research Lab. Figure 3.8 shows a sketch of the chamber layout of the PVD-75B sputter system. It employs three sputter guns with guns B and C possessing magnetic capabilities. All sputter guns occupy 4" sputter targets.

Ideally, the multilayer stacks are deposited in a single run. The material targets are placed on the sputter guns and the platen is rotated at a constant speed over the guns. Material sputter rates are characterized based on the sputter dynamics and tooling factors

such that the desired stack thickness is achieved. The PVD-75B system does not allow co-sputtering and hence, individual layers of the multilayer stack are deposited manually by characterizing the deposition rate for each material-gun combination. The test samples are deposited on cleaved substrates of 4" silicon wafers with <100> plane. The deposition rate is characterized by minimizing the impact of external factors such as metal-gun combination, rotational speed of the platen and pre-sputter time. All samples are deposited with the chamber base pressure set to 3.4×10^{-7} Torr.
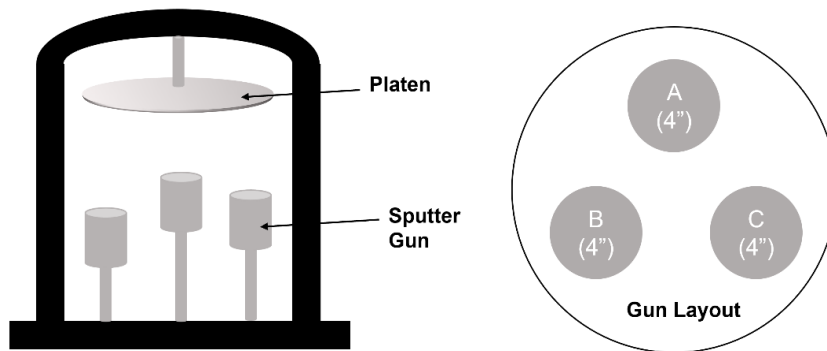
Figure 3.8: Schematic of the gas chamber of PVD -75B of Nanopower Research Lab at RIT.

For the Mo-Ni system, three multilayer samples are deposited at 20%, 50% and 90% Ni by volume. For each sample, two bilayers in Mo/Ni configuration are deposited with a total target thickness of 130nm. Table 3.7 lists the thickness values of the elements rounded to one decimal point. For example, the 20% Ni sample has four thin film layers in configuration Mo/Ni/Mo/Ni with individual layer thickness of Mo and Ni as 51.85nm and 13.15nm, respectively.

Table 3.7: Mo-Ni system composites and respective elemental thickness ratios.

%Ni	Total Mo thickness	Total Ni thickness
20%	103.7nm	26.3nm
50%	65.5nm	64.5nm
90%	13.7nm	116.3nm

The EMA models of the three composites at 800nm inspection wavelength are shown in Figure 3.9. The complex dielectric constant and the corresponding complex refractive index values are modeled at $q = 1/3$ and listed in Table 3.8.
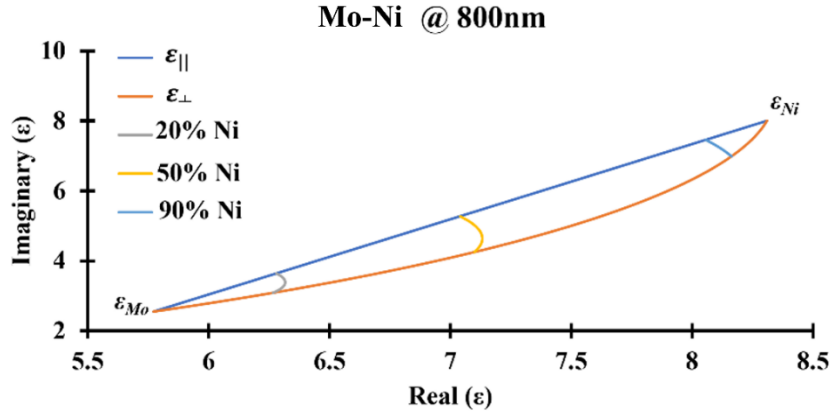
Figure 3.9: Wiener Bounds and the EMA models of the Mo-Ni system at 800nm inspection wavelength. The EMA models are calculated for 20%, 50%, and 90% volume fractions of Ni.

Table 3.8: Complex effective dielectric constants and refractive indices for EMA modelled Mo – Ni composites.

Material Composition	Dielectric constant		Refractive index	
	ε_r	ε_k	n	k
20%Ni	6.317	3.388	2.597	0.652
50%Ni	7.122	4.858	2.805	0.866
90%Ni	8.100	7.294	3.082	1.183

Multilayer thin films from the Mo-W and the Ni-Al multilayer systems are deposited using the CVC-601 DC sputter system at RIT Nanolabs. The chamber configuration of the CVC-601 sputter system is similar to the PVD-75B system. However, the CVC-601 chamber is substantially larger than the PVD-75B. This affects the pump-down time required to achieve the desired base pressure. The throw distance between the target and the substrate is also comparatively smaller than in the case of PVD-75B system.

The CVC-601 sputter system can house four sputter targets at a time. Figure 3.10 shows the gun/target layout of the CVC-601 DC sputter system. The Mo and Al films are

deposited using the 8" sputter targets. The Ni and W thin films are deposited using 4"

sputter targets occupying gun D. Similar to the PVD-75B system, the DC sputter system

does not allow co-sputtering and hence, individual layers of the multilayer stack are

deposited manually by characterizing the deposition rate for each target-gun combination.

The test samples are deposited on cleaved substrates of 4" silicon wafers with <100> plane.

The CVC-601 system requires overnight pump down due to the large chamber size. The

multilayer samples are deposited with the base pressure in the range of 5×10^{-7} Torr - 8×10^{-7} Torr.
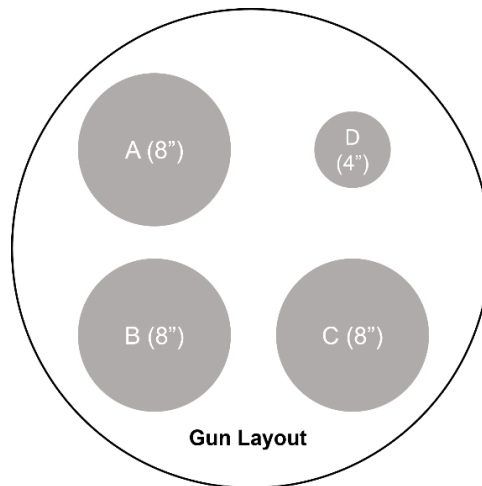
Figure 3.10: Schematic of the gun/target layout of CVC 601 DC sputter system at RIT's Nanolabs.

For the Mo-W system, two multilayer samples are deposited at 45% and 70% W

by volume. For each composite, two bilayers in the Mo/W configuration are deposited with

a total target thickness of 170nm. Table 3.9 lists the thickness values of the elements

rounded to one decimal point. For example, the 45%W sample has four thin film layers in

configuration Mo/W/Mo/W with individual layer thickness of Mo and W being 46.75nm

and 38.25nm, respectively. This choice of the total multilayer thickness is higher than the

Mo-Ni multilayers at 130nm. A higher total multilayer thickness is chosen primarily

because of the resolution capabilities of the CVC-601 system. The individual layer thicknesses are still smaller than 80nm ($1/10^{th}$ of inspection wavelength).

Table 3.9: Mo-W system composites and respective elemental thickness ratios.

%W	Total Mo thickness	Total W thickness
45%	93.5nm	76.5nm
70%	51nm	119nm

The EMA models of the two composites from the Mo-W system at 800nm inspection wavelength are shown in Figure 3.11. The complex dielectric constant and the complex refractive index values are modeled at $q = 1/3$ and listed in Table 3.10.
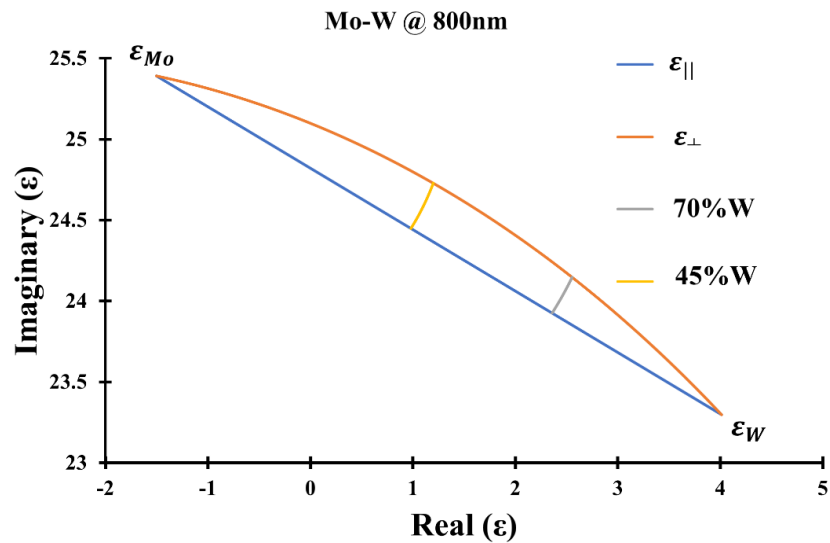
Figure 3.11: Wiener Bounds and EMA models of composites from the Mo-W system at 800nm inspection wavelength. The EMA models are calculated for 45% and 70% volume fractions of W.

Table 3.10: Complex effective dielectric constants and refractive indices for EMA modeled Mo-W composites.

Material Composition	Dielectric constant		Refractive index	
	ε_r	ε_k	n	k
45% W	1.058	24.53	3.578	3.427
70% W	2.426	23.99	3.643	3.293

Similar to the Mo-W system, two multilayer samples are verified at 45% and 75% Ni by volume from the Al-Ni material system. For each composite, two bilayers in Al/Ni configuration are deposited with a total target thickness of 170nm. Table 3.11 lists the thickness values of the elements rounded to one decimal point. For example, the 45% Ni sample has four thin film layers in configuration Al/Ni/Al/Ni with individual layer target thickness of Al and Ni being 46.75nm and 38.25nm, respectively.
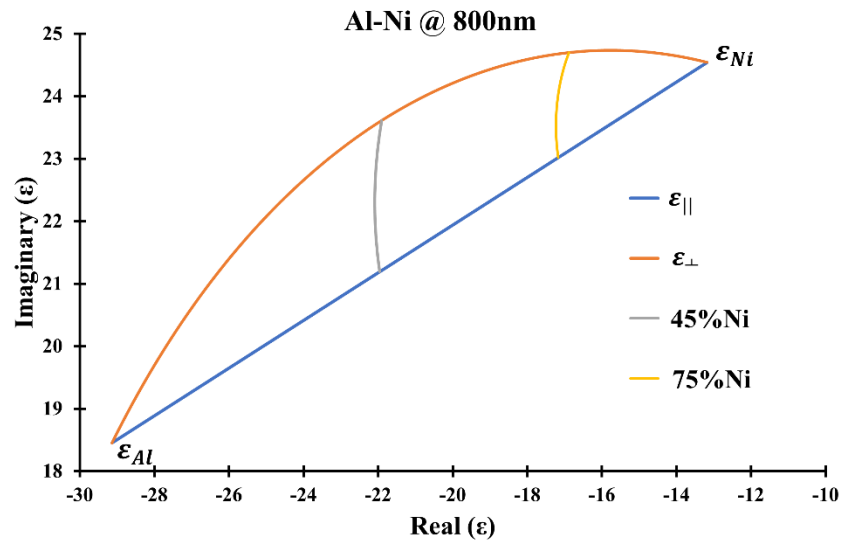
Figure 3.12: Wiener Bounds and EMA models of composites from the Al-Ni system at 800nm inspection wavelength. The EMA models are calculated for 45% and 75% volume fractions of Ni.

Table 3.11: Al-Ni system composites and respective elemental thickness ratios.

%Ni	Total Al thickness	Total Ni thickness
45%	93.5nm	76.5nm
75%	42.5nm	127.5nm

The EMA models for the two composites from the Al-Ni system at 800nm inspection wavelength are shown in Figure 3.12. The complex dielectric constant and the complex refractive index values are modeled at $q = 1/3$ and listed in Table 3.12.

Table 3.12: Complex effective dielectric constants and refractive indices of the EMA modeled Al-Ni composites.

Material Composition	Dielectric constant		Refractive index	
	ε_r	ε_k	n	k
45% Ni	-22.1	22.03	2.134	5.161
75% Ni	-77.2	23.65	2.452	4.821

3.4.3 Thin Film Composition and Analysis

The optical constants of the multilayer composites are measured using J.A. Woollam's Variable Angle Spectroscopic Ellipsometry (VASE). The measured thin films are analyzed using the J.A. Woollam's CompleteEASE software. [113], [114].

The ellipsometer measures the changes in the polarization state of the reflected light. Experimentally, two parameters are measured in a standard ellipsometry measurement specifically, ψ and Δ. This is mathematically represented as:

$$\frac{R_p}{R_s} = \tan(\psi).\,e^{i\Delta} \tag{3.8}$$

where, R_p and R_s are the Fresnel reflection coefficients of the p and s polarized light, respectively. The ellipsometry parameters $\tan(\psi)$ and Δ are the magnitude of the reflectivity ratio and the phase in polar form, respectively.

The measurements are made at multiple angles over a wide spectral range to obtain multiple data points. A large number of data points significantly improves the accuracy of the sampled parameters. Typically, one set of constants is unknown, either the film thickness or optical constants (n & k). Using the oscillator models discussed in section 2, the optical constants are modeled with an error score as an indicator of the fit quality. The error score is quantified as Mean Square Error (MSE) which is given as:

$$MSE_{NCS} = \sqrt{\frac{1}{3n-m}\sum_{i=1}^{n}\left[\left(\frac{N_{E_i}-N_{G_i}}{0.001}\right)^2 + \left(\frac{C_{E_i}-C_{G_i}}{0.001}\right)^2 + \left(\frac{S_{E_i}-S_{G_i}}{0.001}\right)^2\right]} \quad (3.9)$$

where n is the number of wavelengths and m is the number of fit parameters, $N = \cos(2\psi)$, $C = \sin(2\psi)\cos(\Delta)$ and $S = \sin(2\psi)\sin(\Delta)$.

The MSE is in-fact the Root Mean Squared Error (RMSE). As indicated by Eq. (3.9), the MSE sums the difference between the measured data (subscripted "E") and model generated data (subscripted "G") for the entire defined wavelength range. This difference is calculated in terms of parameters N, C and S derived through ψ and Δ, as mentioned above. More details on these parameters can be found in the CompleteEASE manual [114]. Low MSE indicates a better fit of data and a high model accuracy. Although a lower MSE is desired, there is no target value.

In this experiment, the samples are measured at 65°, 70° and 75° angles for a wavelength range of 300nm – 1200nm. As previously mentioned, the individual sputter rates are characterized by different sputter gun – target combinations. This is because the throw distance from the target to substrate varies for different sputter guns in the PVD-75B system. Furthermore, the sputter dynamics differ for different deposition tools. Therefore, Mo and Ni are characterized differently for the PVD-75B and the CVC-601 systems. For measuring all films through ellipsometry, a model for native oxide on the silicon (Si) substrate is generated using a bare Si sample. The thickness value of native oxide is then used for thin film modeling.

The optical constants of individual thin films are first measured using ellipsometry. These measured optical constants are used in the EMA models of the multilayer thin films

shown in section 3.4.1. The measured values of optical constants are used for EMA models as the optical constants of thin films differ from their bulk counterparts. Additionally, external factors such as chamber impurity, oxidation and tool signature may also affect the film quality. However, these conditions remain relatively constant for all the samples fabricated using the same tool and conditions.

All samples under investigation are measured using the B-Spline (Basis-spline) layer in the CompleteEASE software. B-Spline is a dispersion layer that is used to describe the complex dielectric constant of the sample, consistent with the Kramers-Kronig relationship described in section 2.3.3. Additional information on B-spline layers can be found in the CompleteEASE manual.
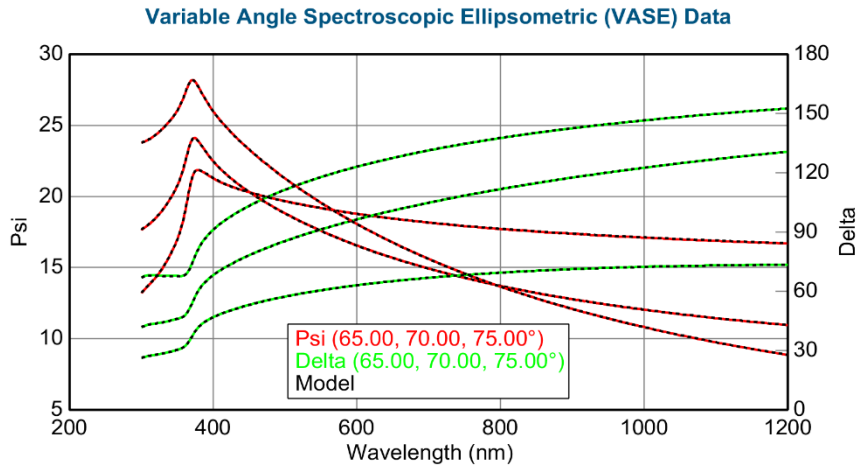
Figure 3.13: Ellipsometry data of the 33.5nm Molybdenum thin film deposited through the PVD-75B RF magnetron sputtering system. ψ and Δ are measured at 65º, 70º and 75º angles in the wavelength range of 300nm – 1200nm.

Figure 3.13 shows the ellipsometry data of a molybdenum thin film deposited through the PVD-75B RF magnetron sputtering system. The Mo film has a thickness of 33.5nm, measured using the KLA's P2 profilometer. The figure shows the measured and modeled ψ and Δ at 65º, 70º and 75º angles in the 300nm – 1200nm wavelength range. It is observed that the ellipsometer model (dotted black lines) fits the measured values. An

MSE of 0.593 indicates a good agreement between the measured and modeled values of the ellipsometer.

Ellipsometry Measurement of Mo Thin Film
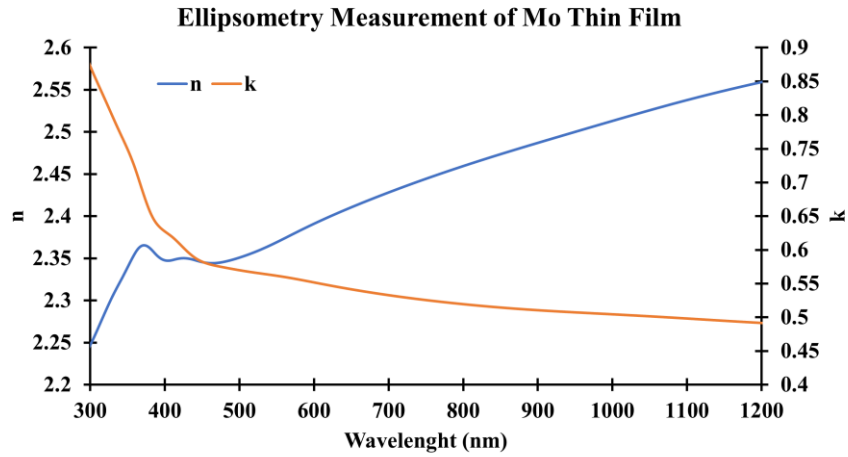
Figure 3.14: Optical constants of the 33.5nm Mo thin film. The Mo film has a refractive index $n = 2.459$ and an extinction coefficient $k = 0.519$ at 800nm inspection wavelength.

The measured optical constants corresponding to Figure 3.13 are plotted in Figure 3.14. The 33.5nm Mo thin film has a refractive index $n = 2.459$ and an extinction coefficient $k = 0.519$ at 800nm inspection wavelength.

Variable Angle Spectroscopic Ellipsometric (VASE) Data
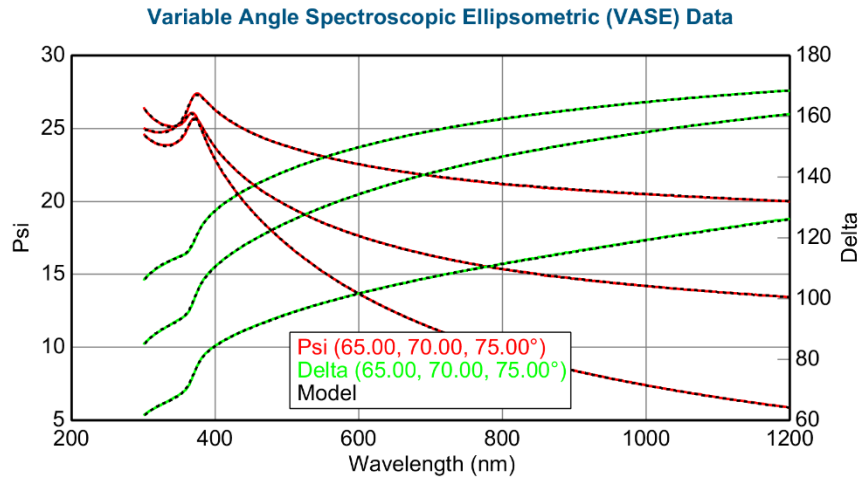
Figure 3.15: Ellipsometry data of the 20nm Nickel thin film deposited through the PVD-75B RF magnetron sputtering system. ψ and Δ are measured at 65°, 70° and 75° angles in the wavelength range of 300nm – 1200nm.

Similarly, a 20nm thin film deposited using the PVD-75B RF magnetron sputtering system is using the ellipsometer. The VASE data of the 20nm Ni film is shown in Figure 3.15 and the corresponding optical constants are plotted in Figure 3.16. The Ni film has a refractive index $n = 3.15$ and an extinction coefficient $k = 1.228$ at 800nm inspection wavelength.
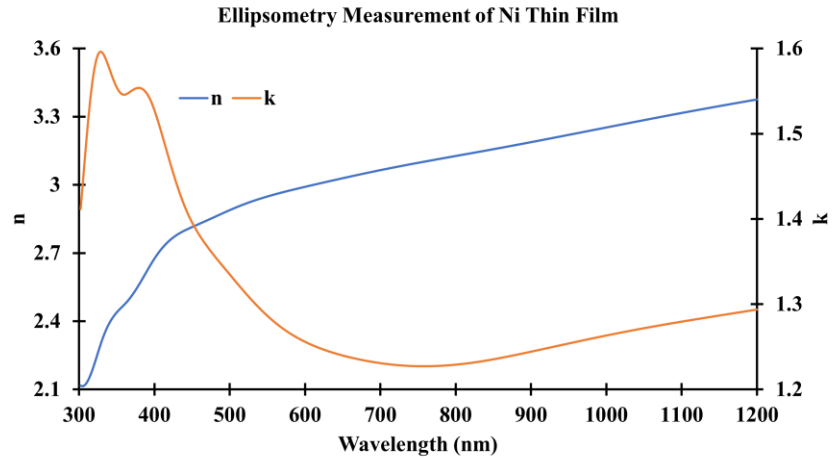
Figure 3.16: Optical constants of the 20nm Ni thin film. The Ni film has a refractive index $n = 3.15$ and an extinction coefficient $k = 1.228$ at 800nm inspection wavelength.

For the Mo-W and the Al-Ni systems, individual thin films were deposited using the CVC-601 DC sputter system. Figure 3.17 shows the VASE data for a 48.5nm Mo thin film deposited using the CVC-601 system.
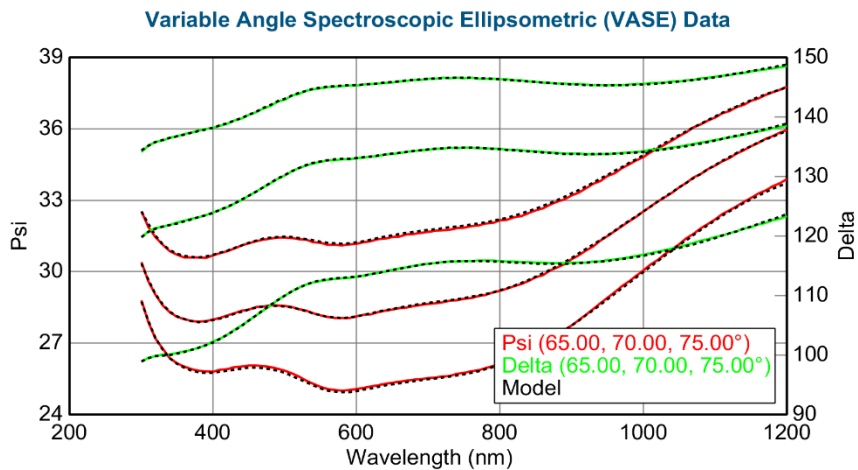
Figure 3.17: Ellipsometry data of the 48.5nm Molybdenum thin film deposited through the CVC 601 DC sputtering system. ψ and Δ are measured at 65°, 70° and 75° angles in the wavelength range of 300nm – 1200nm.

The optical constants of the 48.5nm Mo thin film measured using the ellipsometer are plotted in Figure 3.18. The Mo thin film has a refractive index $n = 3.459$ and an extinction coefficient $k = 3.669$ at 800nm inspection wavelength. The optical model MSE is 1.538.

Optical constants of Mo Thin Film - CVC 601 Sputter
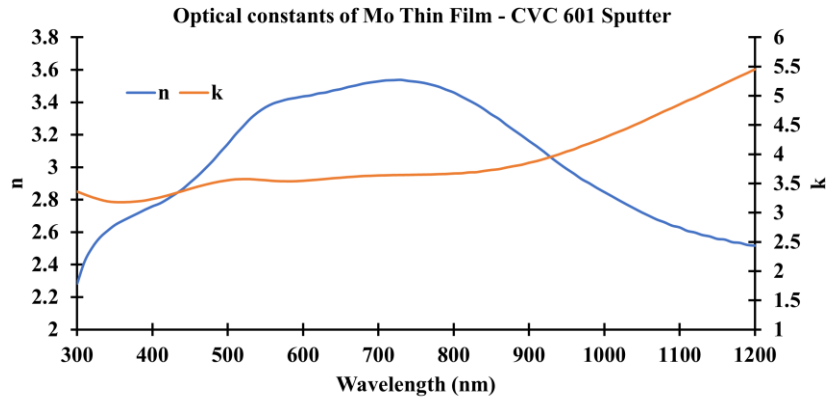
Figure 3.18: Optical constants of the 48.5nm Mo thin film. The Mo film has a refractive index $n = 3.459$ and an extinction coefficient $k = 3.669$ at 800nm inspection wavelength.

The VASE data of a 45nm W thin film are shown in Figure 3.19. The modeled values and measured values of ψ and $\varDelta$ have good agreement at all measured angles in the entire wavelength range. Therefore, a low ellipsometry model MSE = 1.408 is observed.

Variable Angle Spectroscopic Ellipsometric (VASE) Data

Psi (65.00, 70.00, 75.00°)
Delta (65.00, 70.00, 75.00°)
Model
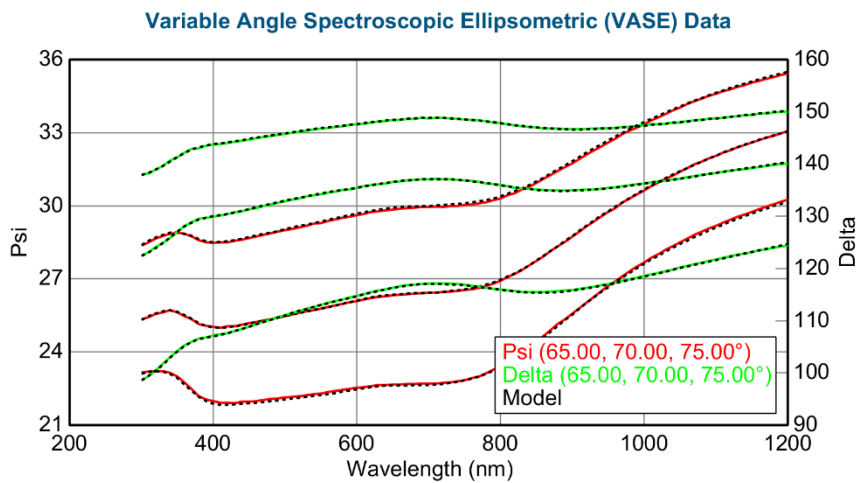
Figure 3.19: Ellipsometry data of the 45nm Tungsten thin film deposited through the CVC 601 DC sputtering system. ψ and $\varDelta$ are measured at 65°, 70° and 75° angles in the wavelength range of 300nm – 1200nm.

The W film under investigation has a refractive index $n = 3.718$ and an extinction coefficient $k = 3.132$ at 800nm inspection wavelength. The optical constants measured through ellipsometry for the entire wavelength range are shown in Figure 3.20.

Optical constants of W Thin Film - CVC 601 Sputter
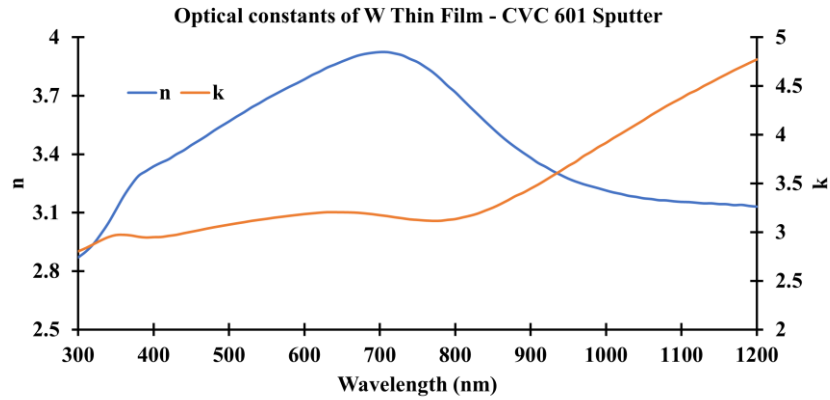
Figure 3.20: Optical constants of the 45nm W thin film. The W film has a refractive index $n = 3.718$ and an extinction coefficient $k = 3.132$ at 800nm inspection wavelength.

Figure 3.21 shows the VASE data of a 1.8μm Al thin film deposited through CVC-601 DC sputter system. Aluminum thin films are deposited using an 8" sputter target. Silicon (1%) is added to the sputter target for electrical applications as aluminum has high Si affinity. The Al thin film has a measured refractive index $n = 1.635$ and an extinction coefficient $k = 5.640$ at 800nm inspection wavelength. The modeled optical constants of deposited aluminum film are plotted in Figure 3.22.

Variable Angle Spectroscopic Ellipsometric (VASE) Data
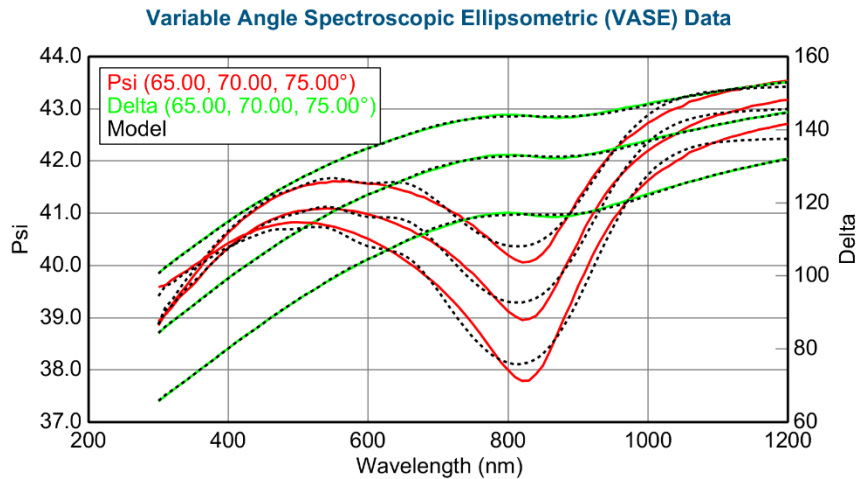
Figure 3.21: Ellipsometry data of the 1.8μm Aluminum thin film deposited through the CVC 601 DC sputtering system. ψ and Δ are measured at 65º, 70º and 75º angles in the wavelength range of 300nm – 1200nm.

The ellipsometry model MSE is 3.564. Comparatively high model MSE may be contributed to high oxidation of aluminum after exposure to atmosphere. Therefore, Al is used as the bottom layer in the Al-Ni multilayer system.
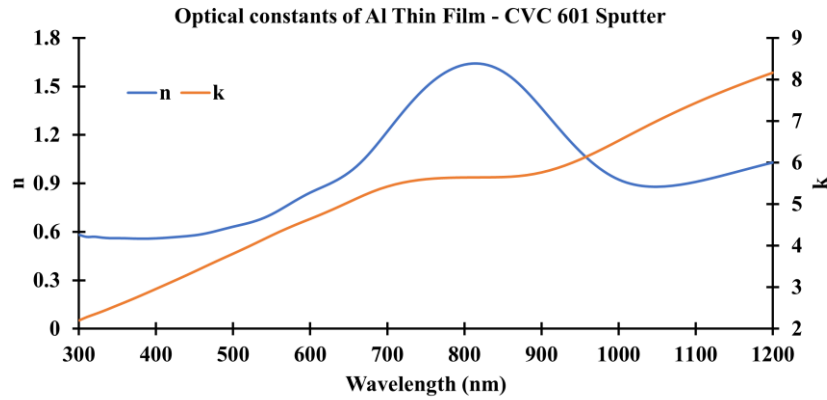
Figure 3.22: Optical constants of the 1.8μm Al thin film. The Al film has a refractive index $n = 1.635$ and an extinction coefficient $k = 5.640$ at 800nm inspection wavelength.

Finally, the optical constants of a 50nm Ni thin film deposited using the CVC 601-DC sputtering system are measured. The VASE data of the 50nm Ni film are presented in Figure 3.23. For this thin film, the measured refractive index $n = 2.708$ and the extinction coefficient $k = 4.529$ at 800nm inspection wavelength. The optical constants are plotted in Figure 3.24.
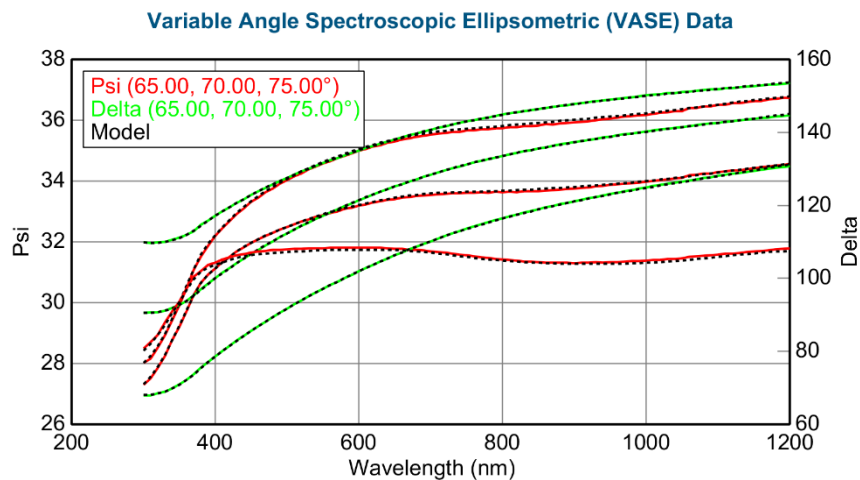
Figure 3.23: Ellipsometry data of the 50nm Nickel thin film deposited through the CVC 601 DC sputtering system. ψ and Δ are measured at 65°, 70° and 75° angles in the wavelength range of 300nm – 1200nm.

The ellipsometer model MSE for the 50nm Ni thin film 1.512. This can also be observed in Figure 3.23 where the model and measured values of ψ and Δ overlap each other at all angles in the entire wavelength range. Therefore, Ni is chosen as the top layer in the Al-Ni multilayer system.
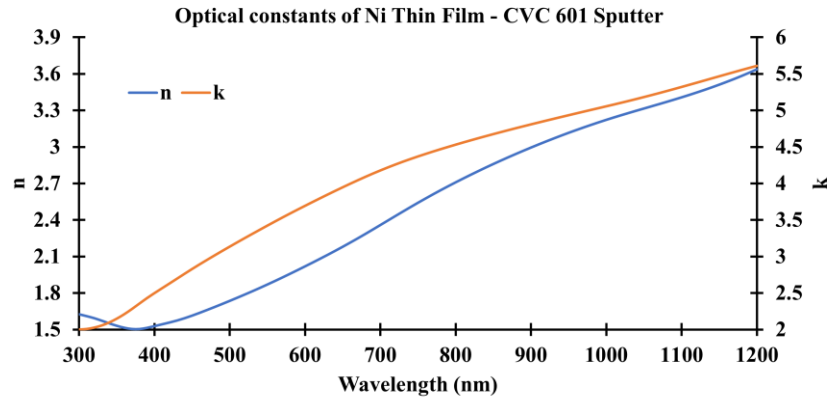
Figure 3.24: Optical constants of the 50nm Ni thin film. The Ni film has a refractive index $n = 2.708$ and an extinction coefficient $k = 4.529$ at 800nm inspection wavelength.

The measured optical constants of all the elemental thin films deposited using the PVD-75B and CVC-601 sputter systems are summarized in Table 3.13. The nickel and molybdenum thin films are deposited using both.

Table 3.13: Measured refractive index n and extinction coefficient k of elemental thin films deposited using respective sputter systems.

Material	Sputter System	Thickness	Refractive index (n)	Extinction coefficient (k)
Mo	PVD-75B (RF)	33.5nm	2.459	0.519
Ni	PVD-75B (RF)	20nm	3.15	1.228
Mo	CVC-601 (DC)	48.5nm	3.459	3.669
W	CVC-601 (DC)	45nm	3.718	3.132
Al	CVC-601 (DC)	1.8µm	1.635	5.640
Ni	CVC-601 (DC)	50nm	2.708	4.529

3.4.4 Multilayer Verification Results and Discussion

As previously mentioned in section 3.4.1, multilayers from the Mo-Ni system are deposited using the PVD-75B RF magnetron sputter system. Three multilayer configurations at 20%Ni, 50%Ni and 90%Ni are deposited as listed in Table 3.7. The optical constants of these multilayer composites are measured using the VASE ellipsometer. Similar to the single elemental thin films, the multilayer composites are measured at 65°, 70° and 75° angles in the 300nm – 1200nm wavelength range.

The VASE data for a 130nm, 20%Ni sample is presented in Figure 3.25. The measured ψ and Δ of the multilayer composite differs from its constituent elements Mo and Ni. The multilayer composite is modeled using the B-spline layer in the CompleteEASE software using the Kramers-Kronig relationship. It can be observed that the modeled and measured ψ and Δ of the 20%Ni composite have good agreement in the entire wavelength range at all angles. Therefore, a low MSE = 1.99 is observed.

Figure 3.25: Ellipsometry data of the 20%Ni multilayer composite from the Mo-Ni system deposited using the PVD 75B RF magnetron sputtering system. ψ and Δ are measured at 65°, 70° and 75° angles in the wavelength range of 300nm – 1200nm.

The optical constants of the 20%Ni sample are plotted in Figure 3.26 in the entire wavelength range. At 800nm inspection wavelength, the refractive index $n = 2.541$ and the

extinction coefficient $k = 0.651$. The measured optical constants are closer to the optical constants of the Mo thin film deposited using the PVD-75B sputter system. However, the addition of Ni increases the refractive index and the extinction coefficient of the multilayer composite as predicted by the EMA model. The measured optical constants of the 20% Ni sample are in good agreement with the EMA modeled values from Table 3.8.
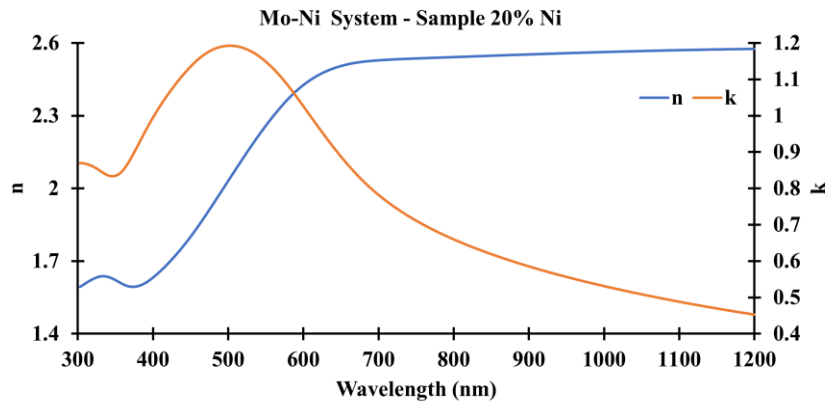
Figure 3.26: Optical constants of the 20%Ni multilayer composite from the Mo-Ni system. The multilayer composite has a refractive index $n = 2.541$ and an extinction coefficient $k = 0.651$ at 800nm inspection wavelength.

Similarly, a 50% Ni sample is also deposited using the PVD-75B system and the corresponding optical constants are measured using the VASE ellipsometer. The multilayer sample thickness measured using a profilometer is 138nm.
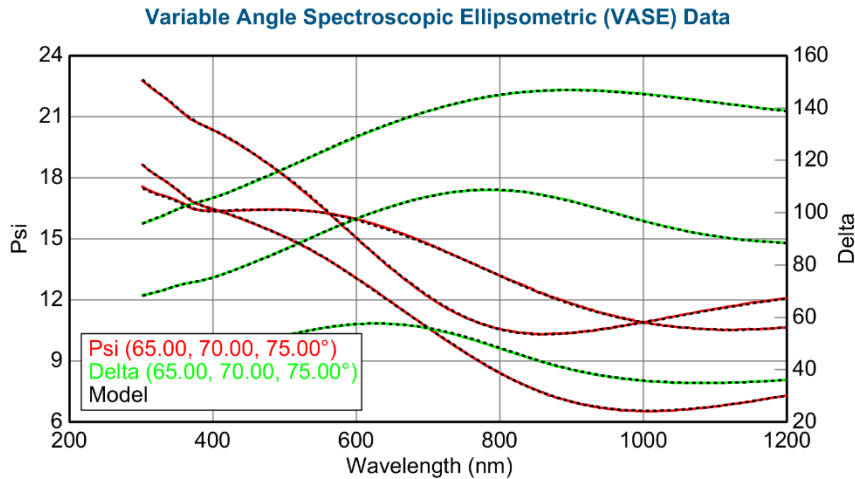
Figure 3.27: Ellipsometry data of the 50% Ni multilayer composite from the Mo-Ni system deposited using the PVD 75B RF magnetron sputtering system. ψ and Δ are measured at 65º, 70º and 75º angles in the wavelength range of 300nm – 1200nm.

The VASE data for the 50% Ni sample is presented in Figure 3.27. A model MSE of 0.754 shows good agreement between the modeled and measured values of ψ and Δ at 65°, 70° and 75° in the measurement wavelength range.
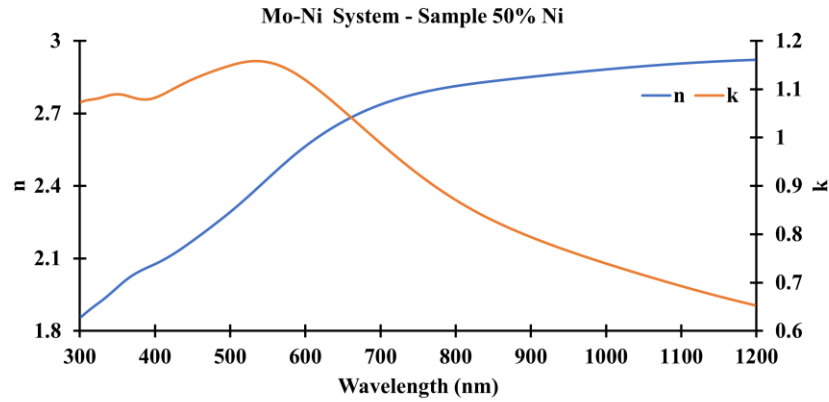
Figure 3.28: Optical constants of the 50%Ni multilayer composite from the Mo-Ni system. The multilayer composite has a refractive index $n = 2.812$ and an extinction coefficient $k = 0.866$ at 800nm inspection wavelength.

The optical constants of the 50% Ni composite corresponding to the VASE data in Figure 3.27 are presented in Figure 3.28. The composite has a refractive index $n = 2.812$ and an extinction coefficient $k = 0.870$. In comparison to the 20% Ni composite, additional Ni in the sample results in higher n & k as predicted by the EMA model. Furthermore, the EMA modeled optical constants at 800nm inspection wavelength are in good agreement the measured values.

The final composite in the Mo-Ni material system has 90% Ni by volume. The multilayer has a total thickness of 113nm with high surface roughness. The reduced thickness and the high surface roughness is attributed to the chamber contamination by a deposition run for a dielectric material despite a long pre-sputter time. Additionally, the dielectric material was deposited using the sputter head used for Ni in the PVD-75B system. Target replacement led to alteration of the deposition rate from the calibrated value.

The VASE data for the 90% Ni sample is shown in Figure 3.29. The model has a low MSE value of 0.547 highlighting extremely good fit between model and measured values of ψ and Δ.
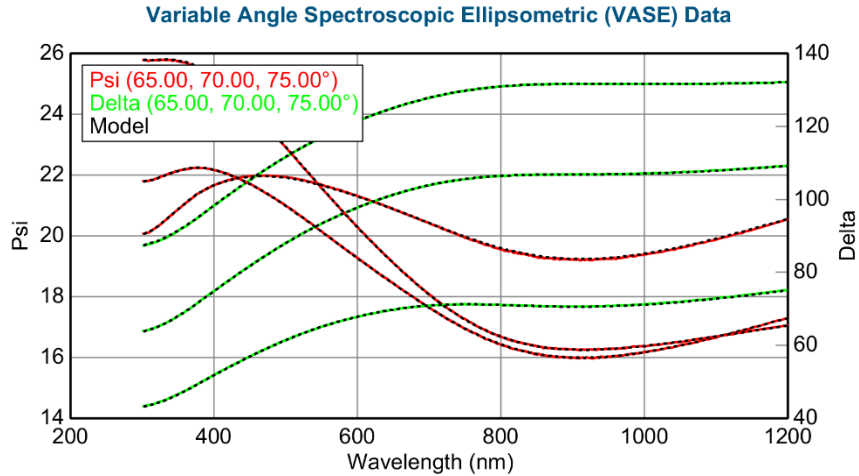
Figure 3.29: Ellipsometry data of the 90% Ni multilayer composite from the Mo-Ni system deposited using the PVD 75B RF magnetron sputtering system. ψ and Δ are measured at 65°, 70° and 75° angles in the wavelength range of 300nm – 1200nm.

The optical constants for the 90% Ni composite measured using the ellipsometer are presented in Figure 3.30. At 800nm inspection wavelength, the 90% Ni sample has a refractive index $n = 3.346$ and an extinction coefficient $k = 1.398$. Due to the chamber contamination, the measured values do not match with the EMA modeled values resulting in a poor EMA model agreement.
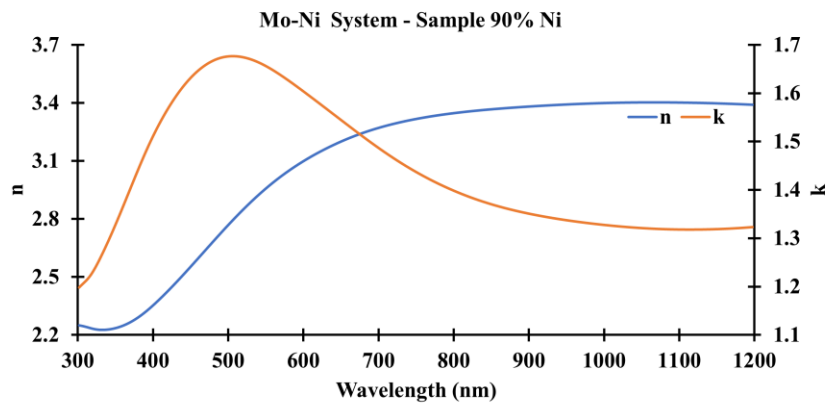
Figure 3.30: Optical constants of the 90%Ni multilayer composite from the Mo-Ni system. The multilayer composite has a refractive index $n = 3.346$ and an extinction coefficient $k = 1.398$ at 800nm inspection wavelength.

Table 3.14 summarizes the verification results of the Mo-Ni multilayer composites deposited using the PVD-75B RF magnetron sputter system. The EMA modeled complex refractive indices of the three composites are compared with the complex refractive indices of three samples measured through ellipsometry. The measured optical constants are in good agreement with the EMA modeled values for the 20% and the 50% Ni compositions.

Table 3.14: EMA model verification results of the Mo-Ni multilayer composites at 800nm inspection wavelength.

Material Composition	EMA Modeled		Measured	
	n	k	n	k
20% Ni	2.597	0.652	2.541	0.659
50% Ni	2.805	0.866	2.812	0.866
90% Ni	3.082	1.183	3.346	1.398

Multilayer thin films from the Mo-W and the Al-Ni systems are deposited using the CVC-601 DC sputter system. Compared to the PVD-75B system, the CVC-601 sputter system has a substantially large chamber. Therefore, the minimum achievable base pressure in this system is higher than the PVD-75B system. Additionally, the CVC-601 sputter system houses 8" sputter targets. Molybdenum in the Mo-W multilayer system and Al in the Al-Ni sputter system are deposited using the 8" targets. Large sputter targets and the lack of in-situ thickness monitor limits the minimum achievable thin film thickness repeatability. Therefore, a target thickness of 170nm is chosen for multilayer composites deposited using the CVC-601 system.

For the Mo-W system, two compositions listed in Table 3.10, the 45%W and the 70%W, are used for verification. The VASE data for the 45%W sample is presented in Figure 3.31. The sample has a total thickness of 170nm. The ellipsometry model of ψ and Δ shows good agreement with measured values at all angles in the entire measurement

wavelength range. The ellipsometer model has an MSE = 2.102. The comparatively higher

MSE may be attributed to the higher base pressure of the CVC-601 sputter system.
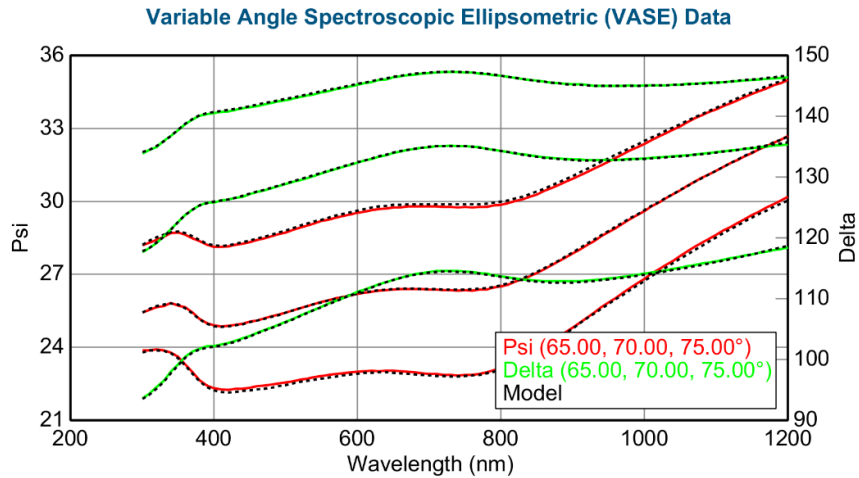
Figure 3.31: Ellipsometry data of the 45%W multilayer composite from the Mo-W system deposited using the CVC 601 DC sputtering system. ψ and Δ are measured at 65°, 70° and 75° angles in the wavelength range of 300nm – 1200nm.

The optical constants of the 45%W sample measured using the ellipsometer are

presented in Figure 3.32. At 800nm inspection wavelength, the 45%W composite has a

refractive index n = 3.579 and an extinction coefficient k = 3.289. As expected, the

measured values of the 45%W composite are between Mo and W values. Addition of W

results in an increase of refractive index n and a reduction in the extinction coefficient k.
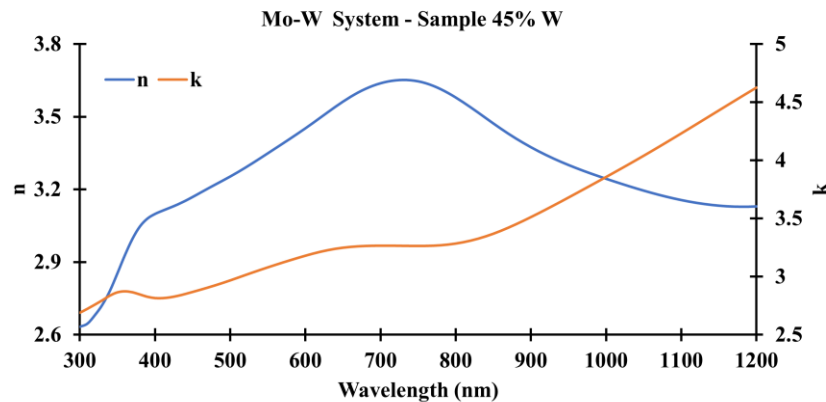
Figure 3.32: Optical constants of the 45%W multilayer composite from the Mo-W system. The multilayer composite has n = 3.579 and k = 3.289 at 800nm inspection wavelength.

In comparison to the multilayer composites deposited using the PVD-75B, the

model agreement between the EMA modeled and measured optical constants for 45%W is

low. Specifically, the measured extinction coefficient k is lower than the corresponding EMA modeled value. This can be attributed to the quality of the thin film deposition using the CVC-601 system.
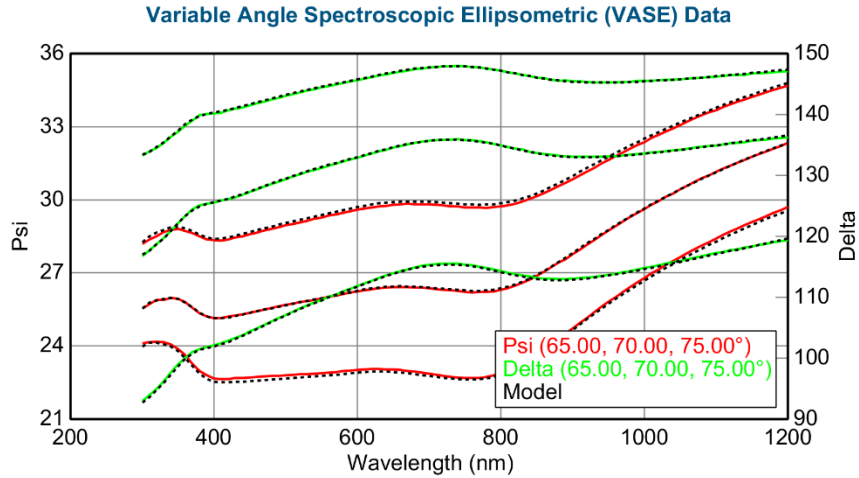
Figure 3.33: Ellipsometry data of the 70%W multilayer composite from the Mo-W system deposited using the CVC 601 DC sputtering system. ψ and Δ are measured at 65°, 70° and 75° angles in the wavelength range of 300nm – 1200nm.

The second multilayer sample from the Mo-W material system has 70% tungsten by volume composition. The total multilayer thickness measured using the P2 profilometer is 170nm. The VASE data for the 70%W composite is presented in Figure 3.33 with a model MSE = 2.427. The model MSE is comparable to 45%W composite which is also deposited using the CVC-601 system.
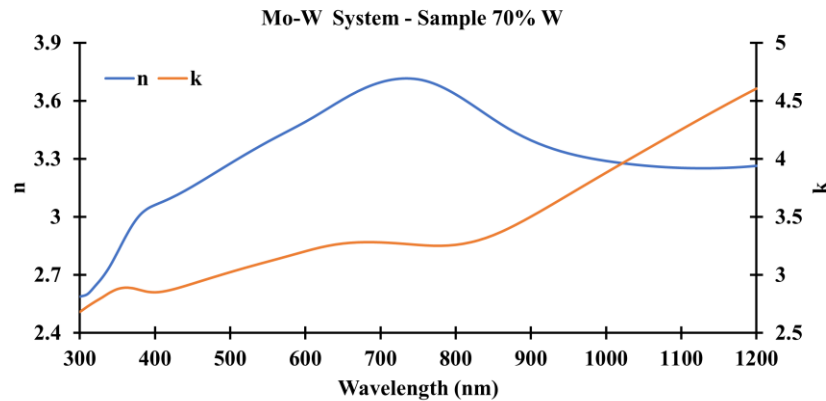
Figure 3.34: Optical constants of the 70%W multilayer composite from the Mo-W system. The multilayer composite has a refractive index $n = 3.633$ and an extinction coefficient $k = 3.206$ at 800nm inspection wavelength.

The optical constants of the 70% W composite measured using the ellipsometer are shown in Figure 3.34. The 70% W sample has a refractive index $n = 3.633$ and an extinction coefficient $k = 3.206$ at 800nm inspection wavelength. The measured values are closer to the optical constants of W due to its higher volume. Comparing the measured n and k with the EMA modeled values shows a good agreement between the two sets. Similar to the 45% W composite, the extinction coefficient is lower than expected.

Finally, the two multilayer composites from the Al-Ni material system are deposited using the CVC-601 DC sputter system for EMA model validation. The EMA model values for the 45% Ni and the 75% Ni are listed in Table 3.12.

For the 45% Ni multilayer sample, the total multilayer thickness is 163.15nm. The reduced thickness is due to Ni target cracking near the racetrack. Essentially, the Ni target was depleted during the deposition run. The VASE data for 45% Ni sample is presented in Figure 3.35. The measured and modeled values of ψ and Δ show good model fit with a model MSE = 2.005.
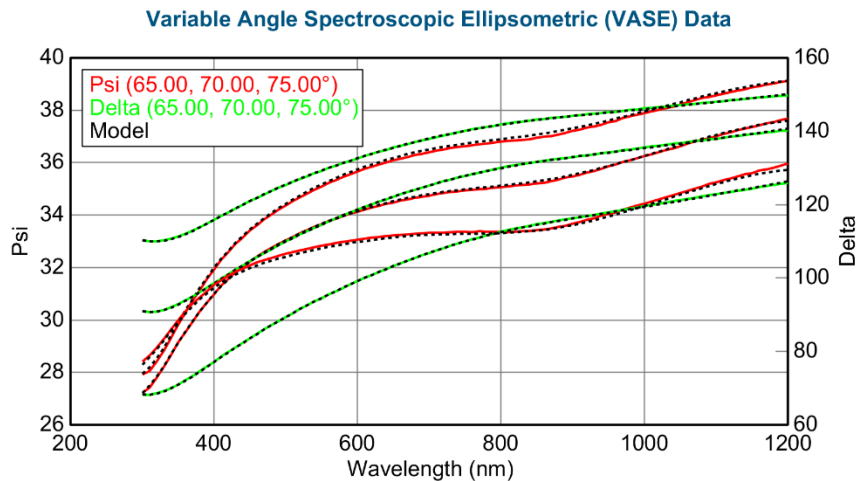
Figure 3.35: Ellipsometry data of the 45%Ni multilayer composite from the Al-Ni system deposited using the CVC 601 DC sputtering system. ψ and Δ are measured at 65º, 70º and 75º angles in the wavelength range of 300nm – 1200nm.

The measured optical constants of the 45% Ni composite are presented in Figure 3.35. The multilayer composite has a refractive index $n = 2.352$ and an extinction

coefficient $k = 4.764$. Although the measured optical constants of the composite are between the optical constants of its constituents, the measured n and k do not match the corresponding EMA modeled values. This is mainly attributed to the cracking of the Ni target, exposing the underlying sputter head with conductive paste.
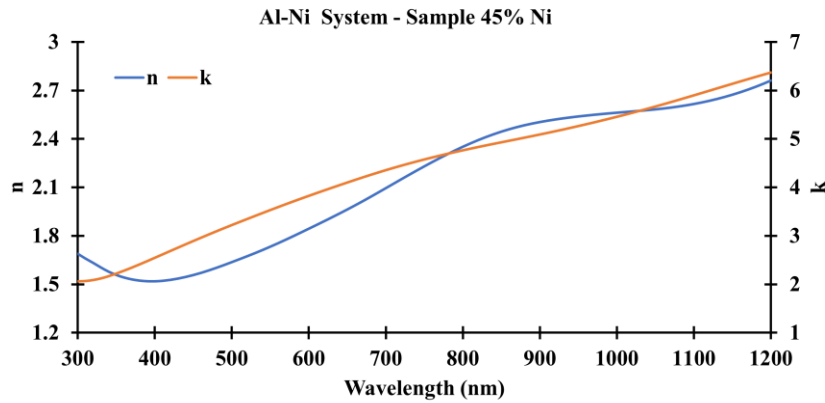
Figure 3.36: Optical constants of the 45%Ni multilayer composite from the Al-Ni system. The multilayer composite has a refractive index $n = 2.352$ and an extinction coefficient $k = 4.764$ at 800nm inspection wavelength.

The 75%Ni sample from the Al-Ni material system was deposited prior to the 45%Ni sample. Therefore, the multilayer sample was effectively deposited using the Ni target without cracking. The total multilayer thickness of the 75%Ni composite measured using the profilometer is 172.8nm.

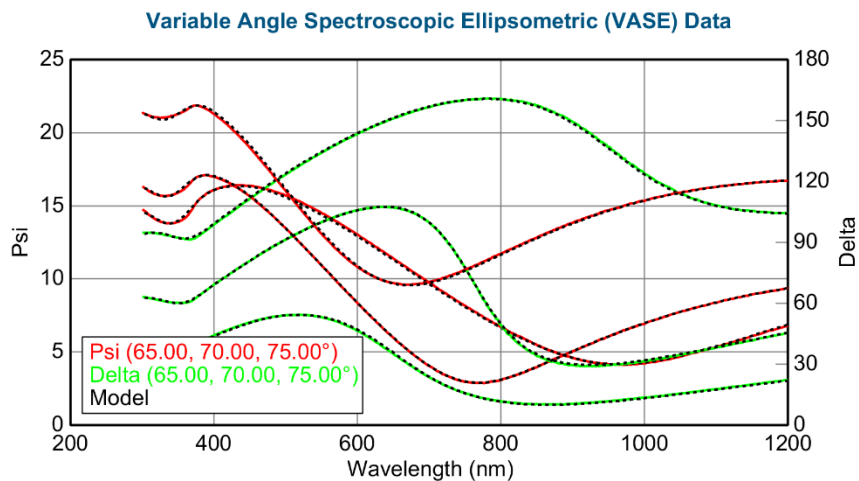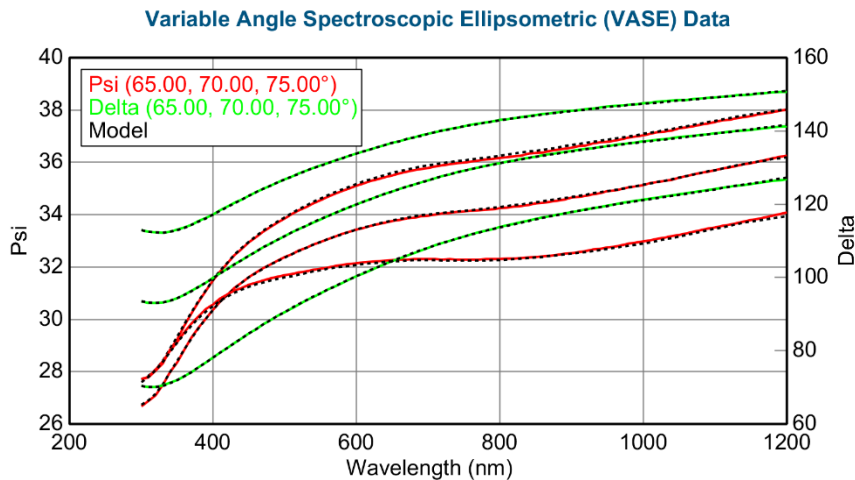**Figure 3.37: Ellipsometry data of the 75%Ni multilayer composite from the Al-Ni system deposited using the CVC 601 DC sputtering system. ψ and Δ are measured at 65°, 70° and 75° angles in the wavelength range of 300nm – 1200nm.**

The VASE data for the 75%Ni composite presented in Figure 3.37 shows good fit between the modeled and measured values of ψ and $\varDelta$ at angles in the measurement wavelength range. The model MSE = 1.5 is comparatively better than other composites deposited using the CVC-601 sputter system.
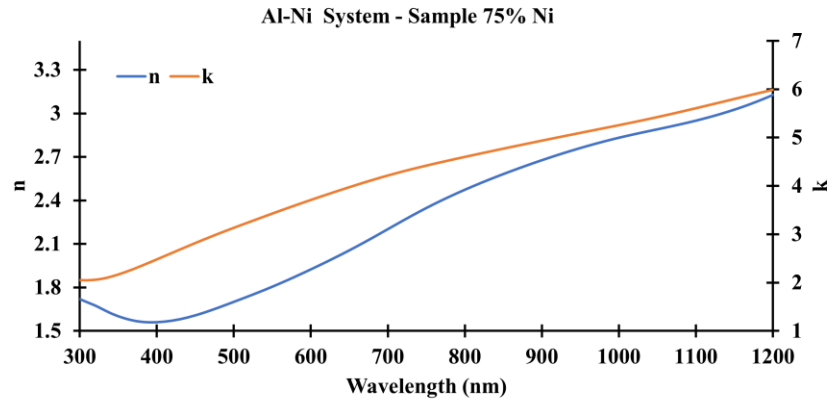
Figure 3.38: Optical constants of the 75%Ni multilayer composite from the Al-Ni system. The multilayer composite has a refractive index n = 2.473 and an extinction coefficient k = 4.600 at 800nm inspection wavelength.

The measured optical constants of the 75%Ni composite are presented in Figure 3.38. The composite has a refractive index n = 2.473 and an extinction coefficient k = 4.600. The measured n and k are heavily skewed toward the optical constants of the Ni thin film deposited through CVC-601 system due to high Ni volume. Although, the measured optical constants of the 75%Ni multilayer composite have good agreement with the corresponding EMA modeled values however, the measured extinction coefficient of the 75%Ni composite is lower than the EMA modeled extinction coefficient. This is consistent with all composites deposited using the CVC-601 DC sputter system.

Table 3.15 provides a summary of verification results for the multilayer composites from the Mo-W and the Al-Ni systems. The optical constants modeled using the effective media approximation model are compared with the measured optical constants of the four multilayer composites deposited using the CVC-601 system.

Table 3.15: EMA model verification results of the Mo-W and the Al-Ni multilayer composites at 800nm inspection wavelength.

Material Composition	EMA Modeled		Measured	
	n	*k*	*n*	*k*
45% W	3.578	3.427	3.579	3.285
70% W	3.643	3.293	3.633	3.206
45% Ni	2.134	5.161	2.352	4.764
75% Ni	2.452	4.821	2.473	4.600

The measured optical constants of the two multilayer composites from the Mo-W material system, specifically the 45%W and the 70%W show good agreement with EMA modeled values. Increasing the volume of tungsten increases the refractive index n and reduces the extinction coefficient k of the multilayer composites as predicted by the EMA model. However, the measured extinction coefficients for both the multilayer composites are lower than expected. This is attributed to the higher chamber base pressure of the CVC-601 system and its resulting quality of the deposited thin film. Additional thin film characterization may reveal the source of this behavior, which is beyond the scope of this thesis.

Two multilayer composites, the 45%Ni and the 75%Ni from the Al-Ni multilayer system are also deposited using the CVC-601 DC sputter system for EMA model validation. For the 45%Ni composite, the EMA modeled optical constants do not match the measured values. This is primarily due to the cracking of the Ni target at the racetrack during the multilayer deposition. The depletion of Ni target at the racetrack exposed the underlying sputter head and conductive paste.

The 75%Ni composite was successfully deposited prior to the 45%Ni composite. Therefore, the measured optical constants of the composite show good agreement with the

corresponding EMA modeled values. Similar to the multilayer composites from the Mo-W system, the extinction coefficient k for the 75% Ni composite is lower than the expected modeled value. Despite this inconsistency, the EMA model provides a reasonable estimation of the optical constants. The model accuracy can further be improved by improving the deposition capabilities as seen from the Mo-Ni multilayer composites deposited using the PVD-75B RF magnetron sputter system.

The optical constants are modeled using an ideal depolarization (q) factor. Precise deposition and characterization techniques can also enable accurate estimation of q factor which is essential for EUVL mask application.

The model validation at optical wavelengths shows that the EMA models have the capability to accurately estimate the optical constants if the thickness condition is fulfilled. This provides a reasonable confidence in employing the EMA model at EUV wavelengths for mask absorber modeling.

4 Absorber Design Considerations

The EUV mask absorbers can be divided into three categories, specifically the attenuated phase shifting mask absorber (attPSM), high $-k$ mask absorber and the index matched absorber ($n \approx 1$). The absorber materials are classified into one of the three categories based on their complex refractive indices as highlighted in Figure 4.1. Absorber candidate materials in the blue region that have refractive indices close to 1 are the index matched absorbers. Similarly, materials in the yellow region that have high extinction co-efficient are the high $-k$ mask absorbers. Finally, material candidates in the orange region are the attPSM absorbers as they introduce a phase shift between the reflected light from the multilayer mirror and the absorbers, respectively. The absorbers candidates can be further subcategorized as a low $-n$, mid $-n$ and a high $-n$ absorber.

Identifying the best EUV mask absorber candidate is challenging because of the tediousness and the high cost of experimental verification in EUV lithography. It is in our best interest to narrow the absorber material choices to the candidates that perform best in simulations and 3D modeling. Therefore, one of the primary objectives of this project is to develop and establish a simple framework that can identify novel mask absorber candidates. For this purpose, the candidate material combinations are first characterized through contrast-based imaging simulations and 3D image modeling of the nearfield magnitude and phase when employed as EUV mask absorbers. The best performing absorber candidates are then co-optimized using lithography metrics such as the NILS and MEEF and the relative absorber reflectivity to identify the potential mask absorbers candidates.
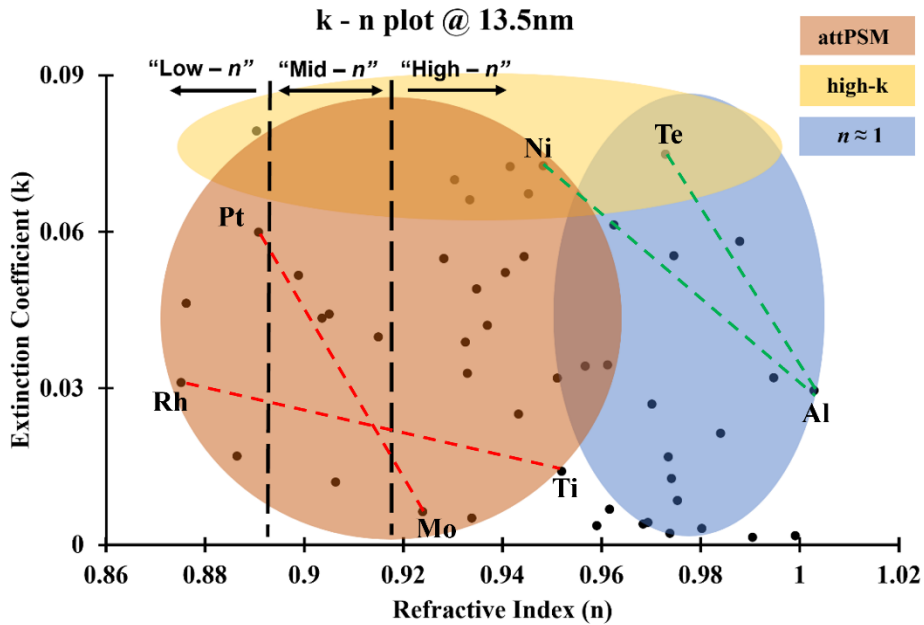
Figure 4.1: *k-n* **plot at 13.5nm highlighting absorber categories based on complex refractive index. attPSM is orange, high-*k* is yellow and index matched absorber is blue. The absorbers are also sub-classified as low-*n*, mid-*n*, and high-*n*. Dotted lines show material systems for EMA modeling of absorber candidates.**

4.1 Aerial Image Contrast

EUV mask absorber alloys modeled using the EMA model in Tables 3.2 – 3.4 are first characterized by simulating the aerial image contrast in an EUVL system using the normalized image log-slope (NILS). Figure 4.2 plots the aerial image NILS vs the mask absorber thickness for a simple case of 13nm line/space pattern with 1:1 duty ratio. As previously mentioned, the NILS serves as an ideal metric to represent the aerial image contrast and the overall imaging performance of the system. For EUVL, a NILS value above 2 is desired. The simulations are performed for a 0.33NA EUVL system at 13.5nm source wavelength and a chief ray angle of 6° using the *Prolith* simulator [115], [116]. The mask stack includes 40 bilayer pairs of Mo (3nm) and Si (4nm) on a 20nm SiO_2 substrate. The Mo/Si multilayer (ML) mirror is followed by a 2nm Ru capping layer and an absorber. The ML mirror may be further optimized to improve the mask reflectivity [117]. The mask

stacks are illuminated by a symmetric dipole source with optimized $\sigma_c = 0.8$ (σ – center) and $\sigma_r = 0.3$ (σ – radius) values, calculated using Eq. (4.1) and Eq. (4.2), respectively. The NA$_c$ and NA$_o$ are the NA of the effective NA of the condenser and objective lens, and pitch (p) is 26nm in this case.
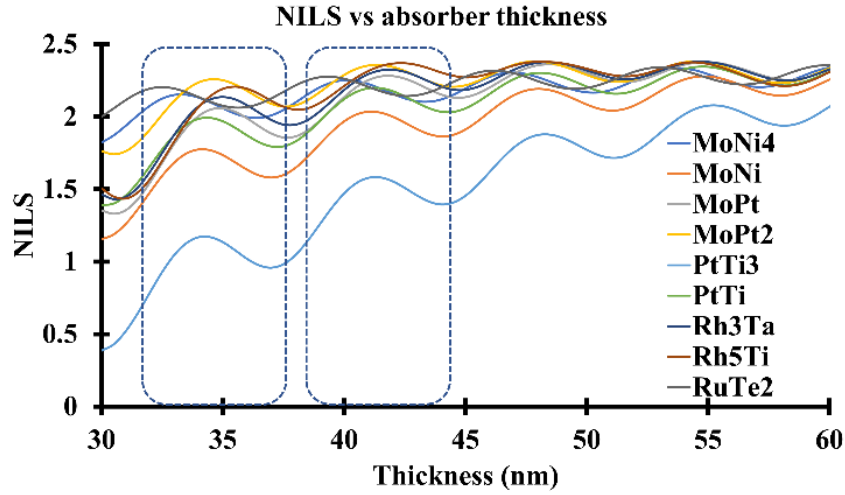
Figure 4.2: Simulated aerial image NILS vs absorber thickness of a 13p26nm L/S pattern using candidate absorber alloys. Highlighted regions show low thickness regions for optimized NILS performance.

An antireflective coating (ARC) is required for a conventional TaBN mask absorber to reduce the absorber reflectivity at inspection wavelengths. For alternative mask absorbers with low reflectivity at smaller absorber thickness, such as high – k mask absorbers, an ARC may not be necessary. In the case of attenuated phase shifting mask absorbers, high mask reflectivity is desired which can be achieved at lower absorber thicknesses. Alternative mask absorbers can therefore reduce the total mask stack thickness.

$$\sigma_c = \frac{\lambda}{2pNA_o} \tag{4.1}$$

$$\sigma_r = \frac{NA_c}{NA_o} \tag{4.2}$$

As observed in Figure 4.2, the interference effects introduced by the reflective EUVL mask absorbers are projected onto the image plane which results in a NILS swing. Therefore, plotting imaging metrics vs the absorber thickness can help determine the optimum absorber thickness corresponding to the best possible solution. Furthermore, the response of lithography metric depends on the choice of absorber material. Therefore, optical properties of the absorber material dictate the choice of absorber thickness for the best imaging performance. In Figure 4.2, two low thickness zones in approximately 5nm thickness range, from 32nm-37nm and 39nm-44nm are identified for optimum NILS response in the desired absorber thickness range. The best performing absorbers in the two respective thickness regions are presented in Table 4.1 and Table 4.2.

As previously mentioned, a NILS value above 2 is desired for an adequate image transfer in an EUVL system. The $PtTi_3$ (0.9396 - i0.0235) and MoNi (0.9337 - i0.0328) absorber candidates have a poor NILS response in low thickness regime with the $PtTi_3$ candidate having a NILS value below 2 in both the highlighted thickness regions. It may be assumed that the high n – low k absorber candidates such as $PtTi_3$ may perform poorly in NILS and the aerial image contrast [118], [119].

Table 4.1 Best NILS generating absorbers in the 32nm – 37nm thickness region along with the corresponding phase shift and reflectivity values.

Absorber @ 32nm – 37nm	Max. avg NILS	Thickness (nm)	Phase shift (º)	Reflectivity (%T)
$MoPt_2$ (n = 0.9025)	2.25	34.5	180	8%
Rh_5Ti (n = 0.8914)	2.20	35.5	206	17%
$RuTe_2$ (n = 0.9588)	2.20	32.5	71	2.2%
$MoNi_4$ (n = 0.9415)	2.15	33.5	104	14%

From the best performing absorber candidates in the 32nm-37nm thickness range listed in Table 4.1, two absorber composites, specifically the $MoPt_2$ (0.9025 – i0.0410) and

Rh_5Ti (0.8914 – i0.0276) are the low – n phase shifting absorber candidates. On the other hand, the $RuTe_2$ (0.9588 – i0.0653) and the $MoNi_4$ (0.9415 – i0.0540) absorber composites have a high extinction coefficient and are the high – k mask absorbers candidates. In the 39nm-44nm thickness range (Table 4.2), absorber composites with lowest n values among all candidate absorbers dominate. The low – n attPSM absorbers therefore produce a better NILS response in both thickness ranges, whereas the high – k mask absorbers have a comparable NILS performance in the 32nm-37nm region. All the low – n attPSM absorber candidates except the $MoPt_2$ composite generate a phase shift above 200°(~1.1π). This is consistent with studies indicating 220º (~1.2π) as the optimal phase shift for low – n EUV attPSM absorbers [120]. The additional 40º (~0.2π) phase shift required is hypothesized to correct for the M3D effects associated with the EUVL masks [121]. The absorber design requirements, including optimum phase shift for attenuated phase shifting masks, are considered in section 4.3. The optimum absorber phase shifts are identified through co-optimization of lithography metrics along with the nearfield 3D performance modeling.

Table 4.2 Best NILS generating absorber candidates in the 39nm – 44nm thickness region along with the corresponding phase shift and reflectivity values.

Absorber @ 39nm – 44nm	Max. avg NILS	@Thickness (nm)	Phase shift (º)	Reflectivity (%T)
Rh_5Ti ($n = 0.8914$)	2.36	42.5	247	12.2%
$MoPt_2$ ($n = 0.9025$)	2.35	41.5	222	4.7%
Rh_3Ta ($n = 0.8982$)	2.32	42.0	229	9%
$MoPt$ ($n = 0.9083$)	2.28	42.0	206	9.2%

The π (180º) phase shift associated with the $MoPt_2$ alloy may be a result of the relatively higher extinction coefficient compared to the other low – n absorber candidates. Therefore, in the lower thickness region, a high – k absorber may be desired for a better aerial image NILS.

4.2 Nearfield Imaging Performance

In a through-pitch layout, isolated features are extremely sensitive to M3D effects. Large best-focus shifts between the isolated and the dense/semi-dense features lead to smaller process windows. The use of alternative mask absorber technologies has shown improvement in the process window conditions by improving the common depth of focus between different pitch patterns at the mask [122]. Therefore, the alternative mask absorbers identified in the previous sections are characterized by 3D image and lithographic performance modeling through nearfield distribution and phase responses.

The nearfield images identify the contribution of the illumination conditions and mask stack on the M3D effects. Figure 4.3 shows the nearfield distribution (plot of nearfield of the nearfield (intensity) inside an EUV mask) for a 13nm isolated feature at 100nm pitch (13p100nm) using the Rh_5Ti (low $-$ n) absorber candidate at 35.5nm optimized thickness from Table 4.1. The white dashed line indicates the top of the multilayer mirror, and the blue dashed line shows the top of the mask absorber layer. The yellow arrow indicates the direction of illumination.
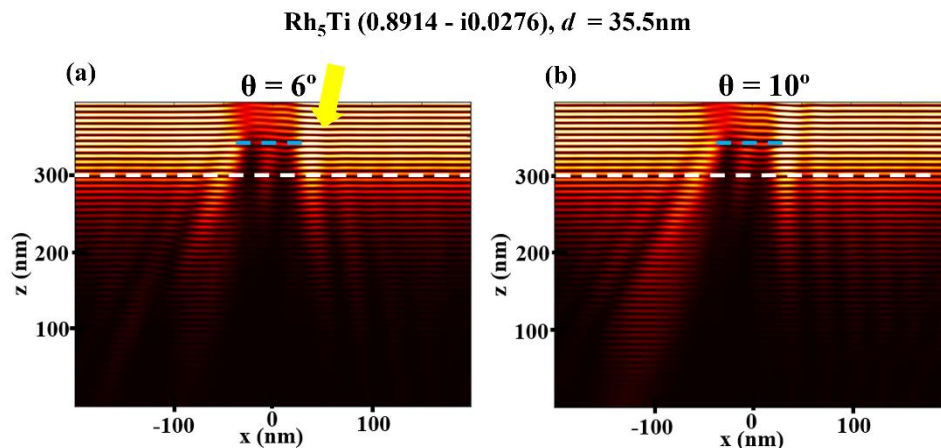
Figure 4.3: Nearfield distribution for 13p100nm isolated feature using 35.5nm Rh_5Ti absorber at propagation angle θ (a) 6° and (b) 10°. The white dashed line indicates top of mirror (302 nm) and blue dashed line indicates top of absorber corresponding to thickness d.

The two nearfield distributions in Figure 4.3 are plotted at propagation angle (θ) =

6° and 10° to investigate the impact of illumination angle. The simulations are performed

on the *DrLitho* simulator suite [123], [124]. As observed in the multilayer region, a larger

propagation angle leads to more shadowing. The low – n attenuated phase shifting mask

absorber experiences lower shadowing compared to the conventional TaBN absorber in

Fig. 1 – (b) at θ = 6°. Higher distribution intensity imbalance is also observed in the

absorber layer (between white and blue dashed lines) at the larger propagation angle (θ =

10°) in comparison to the smaller propagation angle (θ = 6°).
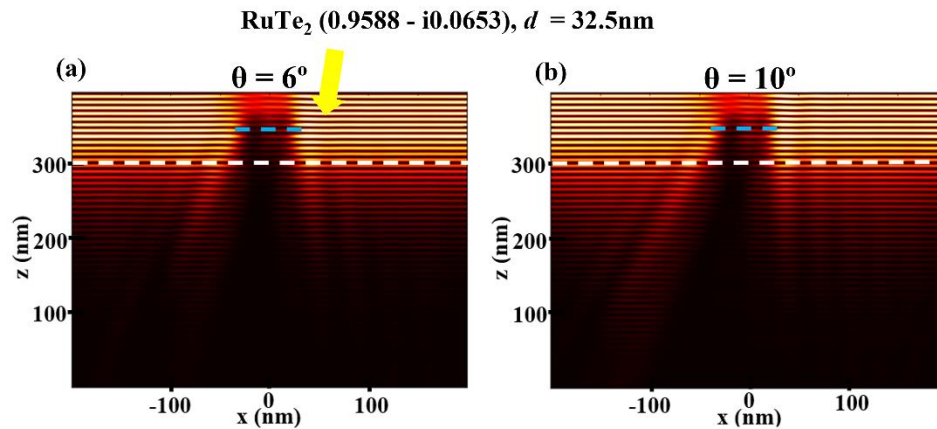
Figure 4.4: Nearfield distribution for 13p100nm isolated feature using 35.5nm RuTe$_2$ absorber at propagation angle θ (a) 6° and (b) 10°. The white dashed line indicates top of mirror (302 nm) and blue dashed line indicates top of absorber corresponding to thickness d.

The nearfield distributions are also plotted for the high – k (RuTe$_2$) mask absorber

candidate in Figure 4.4 at 32.5nm optimized absorber thickness from Table 4.1. The

nearfield distributions are plotted at propagation angles θ = 6° and 10°, respectively. The

high – k mask absorber candidate experiences greater shadowing than the low – n candidate

in Figure 4.3 even at lower absorber thickness. Similar to the low – n absorber candidate,

the shadowing effect is greater at the larger propagation angle. This is due to the enhanced

light absorption of the high – k absorber candidate. However, the distribution intensity

imbalance in the absorber region is also comparatively low at both the propagation angles.

To investigate the intensity imbalance in the low − n (Rh$_5$Ti) and the high − k (RuTe$_2$) mask absorbers, a top-down view of reflected nearfield intensities is plotted for both at 10° propagation angle in Figure 4.5(a) and (b), respectively. The reflected nearfield intensity plots are generated for respective optimized absorber thicknesses from Table 4.1. The low − n attenuated phase shifting absorber candidate has higher absorber reflectivity. A high reflectivity phase shifting masks may result in sidelobes for line/space patterns [58], [119]. This can also be observed in the multilayer region of Figure 4.5(a), that shows high reflectivity regions adjacent to mask line (dark region) for the low − n absorber candidate. Additionally, the low − n absorber has a non-uniform intensity distribution in the absorber region (dark region). In comparison, the high − k absorber candidate in Figure 4.5(b) has a uniform intensity distribution in the absorber region. This is due to the higher light absorption capability of the high − k mask absorber.
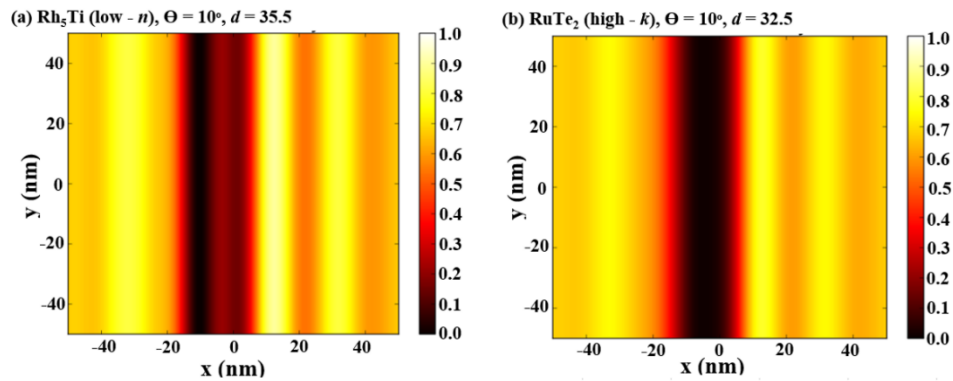
Figure 4.5: Reflected nearfield intensity response for a 13p100nm isolated feature. (a) Rh$_5$Ti (low − n) and (b)RuTe$_2$ (high − k) absorber candidates at incidence angle (θ) = 10°. Higher intensity imbalance in absorber (dark) region is observed for low n absorber.

The nearfield distribution response of the absorber candidates in the higher thickness region from Table 4.2 is also investigated for comparison. Figure 4.6 shows the nearfield distribution intensity of two low − n mask absorber stacks using the 42.5nm Rh$_5$Ti and 41.5nm MoPt$_2$ absorber candidates. The intensity responses are plotted at a 10° propagation angle.

In Figure 4.6, the Rh_5Ti absorber has slightly more intensity imbalance within the absorber region. In contrast, the $MoPt_2$ absorber candidate experiences more shadowing. The Rh_5Ti absorber candidate has a lower extinction coefficient k in comparison to the $MoPt_2$ absorber candidate. The higher extinction coefficient of $MoPt_2$ composite is due to the presence of Pt. Therefore, the extinction coefficient k determines the trade-off between the intensity imbalance and the shadowing for mask absorber candidates. The lower k values result in a reduced shadowing effect but at the cost of high intensity imbalance within the absorber. Additionally, comparing the two Rh_5Ti absorber candidates at different thicknesses from Figures 4.3(a) and 4.6(a) shows a similar performance but a higher shadowing effect is observed for the higher thickness absorber candidate in Figure 4.6(a). Therefore, the absorber thickness also introduces a trade-off between the shadowing effect and the intensity imbalance in the absorber candidate. A higher absorber thickness corresponds to a low intensity imbalance in the absorber but at a cost of more shadowing.
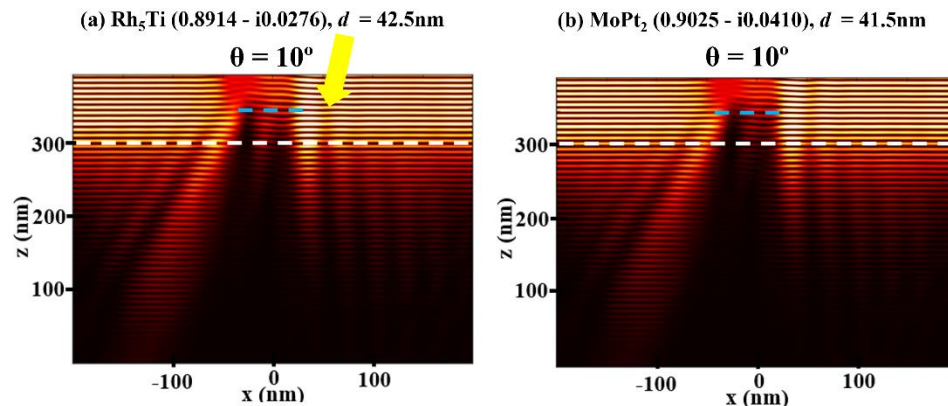
Figure 4.6: Nearfield distribution for 13p100nm isolated feature using (a) 42.5nm Rh_5Ti (a) 6° and (b) 41.5nm $MoPt_2$ absorbers at propagation angle θ = 10°. The white dashed line indicates top of mirror (302 nm) and blue dashed line indicates top of absorber corresponding to thickness d.

The simulated reflected nearfield intensities are also investigated for contact-holes pattern to visualize the absorber performance under EUVL illumination conditions. Figure 4.7 plots the simulated reflected nearfield intensities for a dense 20P40nm contact-holes

pattern using a 61nm TaBN absorber. The reflected nearfield intensities are plotted in a top-down view at 6° and 10° propagation angles. The ideal intensity response should have a uniform intensity distribution throughout the 20nm contact hole opening in x- and y-directions. For the TaBN absorber, a high intensity loss is the open contact region is visible even at 6° propagation angle. The intensity loss in the contact-hole region is even greater when the propagation angle is increased to 10°. This is a result of the partial blocking of light due to oblique illumination setting. The loss of light at larger illumination angles indicate a significant impact of illumination conditions at the mask plane that can lead to M3D effects such as image pattern shifts and CD non-unifromity [58]. A mask absorber with reduced thickness can help alleviate some of these effects.
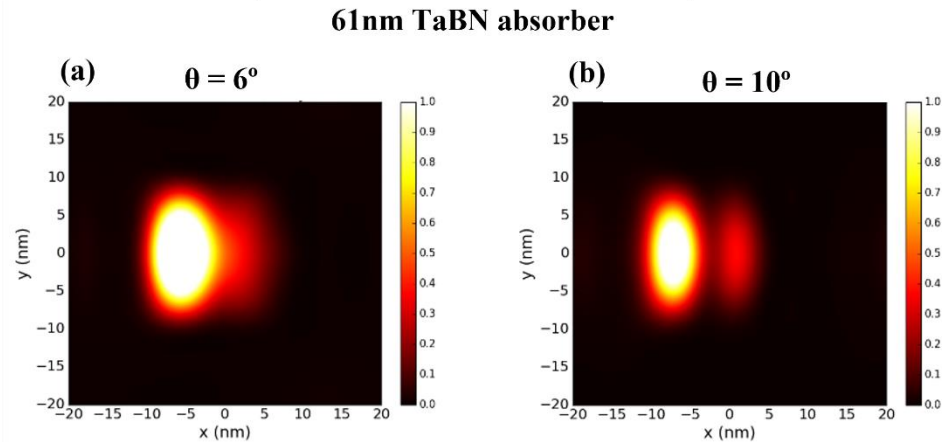
61nm TaBN absorber

Figure 4.7: Reflected nearfield intensities for a 40nm pitch contact-holes pattern with a 20nm opening imaged using 61nm TaBN absorber at propagation angle θ (a) 6° and (b) 10°.

Figure 4.8 plots the reflected nearfield intensity of a dense 20P40 contact-holes pattern simulated using the $low-n$ Rh_5Ti absorber candidate at 42.5nm optimized absorber thickness from Table 4.2. The nearfield intensities are plotted at $θ = 6°$ and 10° propagation angles. In comparison with the TaBN absorber from Figure 4.7, the reflected nearfield intensities observed for the Rh_5Ti mask absorber candidate show a significant improvement. The intensity loss in the contact-hole region is substantially lower at both

the propagation angles. As hypothesized, a reduction in absorber thickness reduces the impact of angular illumination at the mask.

42.5nm Rh₅Ti absorber
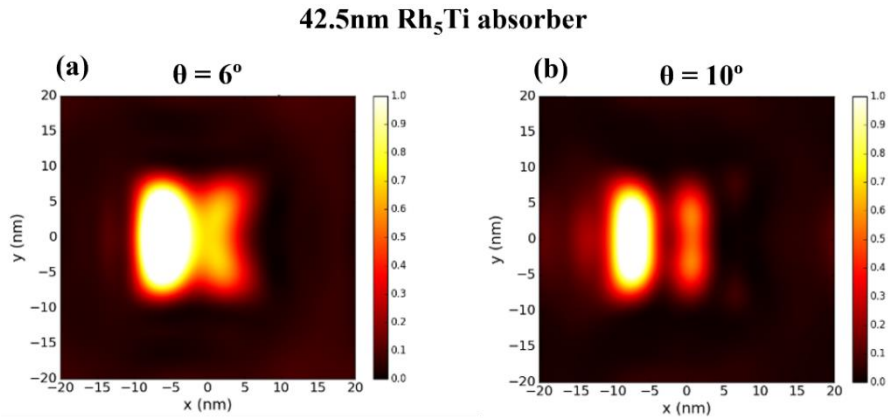
Figure 4.8: Reflected nearfield intensities for a 40nm pitch contact-holes pattern with a 20nm opening imaged using 42.5nm Rh₅Ti absorber at propagation angle θ (a) 6° and (b) 10°.

To investigate the influence of optical properties of the absorber candidate, Figure 4.9 plots the simulated reflected nearfield intensity of the $MoPt_2$ absorber candidate at 41.5nm optimized absorber thickness from Table 4.2. Again, the reflected intensities are plotted at the 6° and 10° propagation angles. While the reflected intensity plots are normalized, it can be deduced that Rh_5Ti and $MoPt_2$ absorber candidates perform better in comparison to the TaBN absorber due to a larger standing wave effect. This is mainly due to the reflective materials used for the attPSM absorber candidates.

41.5nm MoPt₂ absorber
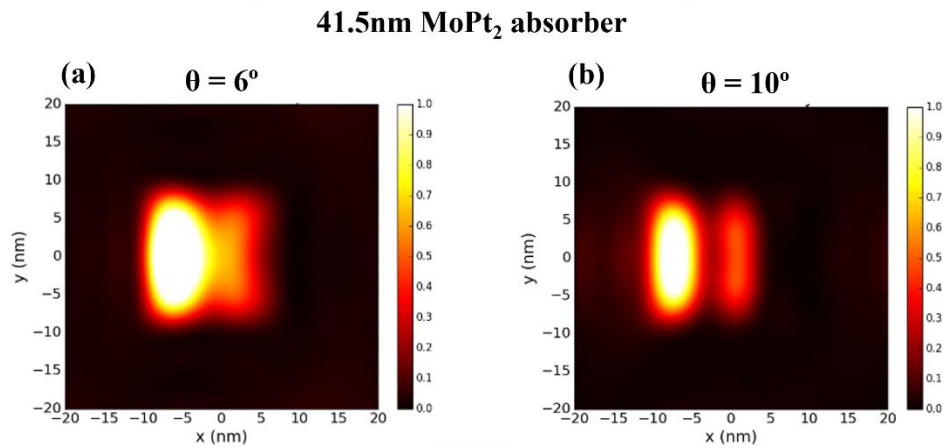
Figure 4.9: Reflected nearfield intensities for a 40nm pitch contact-holes pattern with a 20nm opening imaged using 41.5nm MoPt₂ absorber at propagation angle (a) 6° and (b) 10°.

It is therefore concluded that the absorber candidates with a higher extinction coefficient result in a low intensity imbalance in the absorber region but a higher intensity loss in the open regions. Therefore, the absorber canidates with low *k* may be preferred for dense patterns whereas a higher *k* attPSM absorber candidates may be preferred for isolated patterns. The nearfield images for all the other absorber candidates from Tables 4.1 and 4.2 can be found in the appendix along with the python script used to generate them using the *DrLitho* software suite.

Similarly, the simulated nearfield phase responses of the absorber candidates from Tables 4.1 and 4.2 are investigated at varying propagation angles. A phase response such as observed for an ideal Kirchhoff model is desired. This is shown in Figure 4.10 for an arbitrary absorber, designed to generate 180º phase shift. The phase instantaneously transitions by 180º at the absorber edges.
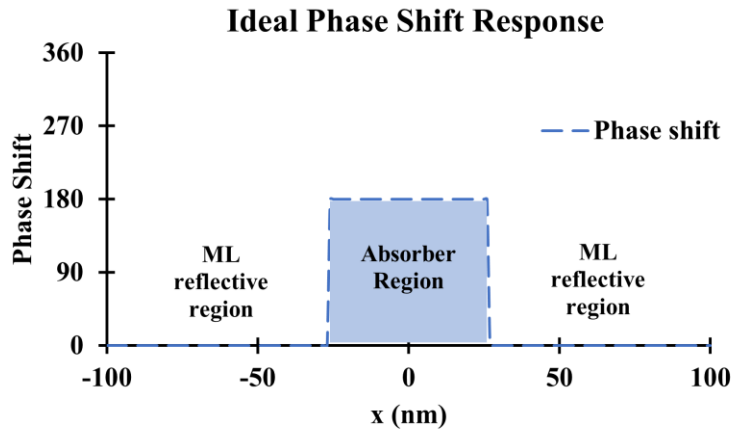
Figure 4.10: Ideal phase shift response of an attenuated phase shifting mask absorber designed to generate 180º phase shift. The blue region indicates absorber region. The phase shift is the reflective multilayer region is 0º.

Figure 4.11 plots the simulated phase shift response of the mask absorber candidates at optimized absorber thickness from Table 4.1. The phase shift responses are observed for a 13nm isolated absorber feature (13p100) at propagation angles $(\theta) = 6°$ and 10º. The absorber candidates are expected to generate phase shifts at the listed optimized

absorber thickness in Table 4.1. For example, the MoPt$_2$ absorber candidate at a thickness of 34.5nm is expected to generate 180º phase shift such as shown in Figure 4.10.

Nearfield phase of candidate mask absorbers from Table 4.1
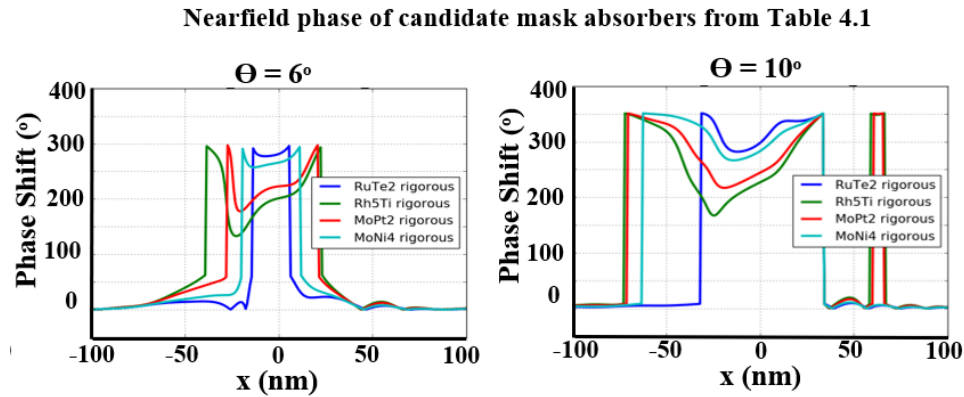
Figure 4.11: Nearfield phase response for a 13p100nm isolated feature of (a) MoPt$_2$ (red), Rh$_5$Ti (green), RuTe$_2$ (dark blue) and MoNi$_4$ (light blue) from Table 4.1 at propagation angles (θ) = 6º and 10º.

In Figure 4.11, the phase jumps at the absorber edge of the absorber candidates at θ = 6º are quite large in comparison to the ideal phase responses. The phase jumps of 360º at θ = 10º are due to the limitation of the plotting range and do not impact the imaging performance of the absorber. However, the phase transition at the absorber edge and the shape of the phase response in the absorber region are of particular importance. The phase transitions at different locations for different absorber candidates. Additionally, the absorber candidates have a non-uniform phase response in the absorber region. These factors greatly depend on the angle of illumination. The phase deformation observed in the absorber region is mainly due to the non-ideal light interference at oblique illumination angles corresponding to intensity imbalances in the nearfield distribution plots. The more reflective low – n attPSM absorber candidates, specifically the Rh$_5$Ti and the MoPt$_2$ have large phase deformation in the absorber region at 6º propagation angle.

The high – k mask absorber candidates, specifically the RuTe$_2$ and the MoNi$_4$ generate a significantly large phase shift at the 6º propagation angle in comparison to the

theoretical expected phase shifts listed in Table 4.1. However, the phase response in the absorber region is uniform. This is consistent with the results of nearfield distribution intensity plots, where the high – k absorber candidates exhibit low intensity imbalance in the absorber region.

The phase response results observed in Figure 4.11 impose a lower limit on the absorber thickness. The low – n candidates generate a non-ideal phase jump at the absorber edge and a non-uniform phase response in the absorber region. On the other hand, the high – k mask absorber candidates generate unexpectedly large phase shift due to increased absorber reflectivity at reduced absorber thickness. Furthermore, increasing the propagation angle may negatively impact the phase response of the mask absorbers.
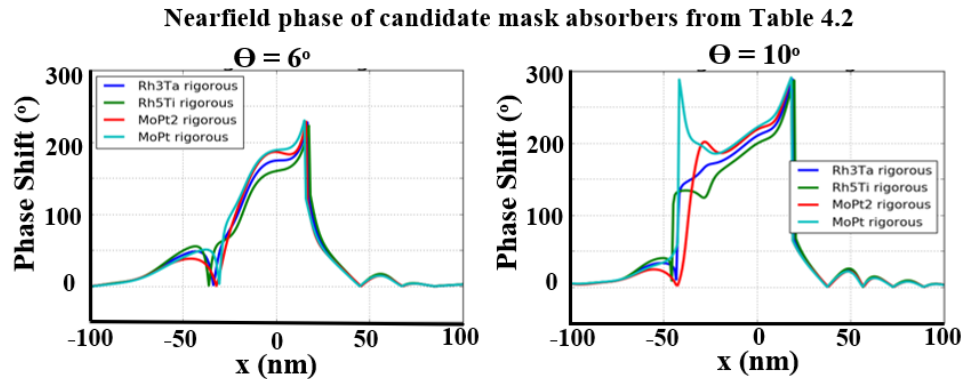
Figure 4.12: Nearfield phase response for a 13p100nm isolated feature of (a) Rh₅Ti (green), (b) MoPt₂ (red), (c) Rh₃Ta (dark blue) and (d) MoPt (light blue) from Table 4.2 at propagation angles (θ) = 6° and 10°.

To investigate the impact of the absorber thickness, the simulated phase shift response of the identified absorber candidates with higher optimum absorber thickness from Table 4.2 are shown in Figure 4.12. The phase responses are shown at a propagation angle $(\theta) = 6°$ and $10°$, respectively. Comparatively, the phase deviations at the absorber edge with higher absorber thickness are low, specifically at $\theta = 6°$. Additionally, the impact of intensity imbalance in the absorber region is also significantly suppressed at larger absorber thickness. At propagation angle $\theta = 10°$, all the absorber candidates except the

MoPt absorber produce a stable phase response with comparatively smaller phase jumps at the absorber edge. The intensity imbalance associated with a larger illumination angle is also minimal in this thickness range. Based on these results, it is concluded that the optimum thickness for alternative absorbers is in the range of 40-45nm.

4.3 Mask Absorber Design Considerations

The EUV mask absorber design is heavily influenced by the choice of absorber material. Optical design requirements of the attPSM absorbers and the index-matched absorbers are first considered. An equally important consideration of absorber patterning capability is presented later.

4.3.1 Attenuated Phase Shifting Mask

To understand the attPSM absorber requirements, absorber candidates from the Rh-Ti and the Mo-Pt material systems, highlighted by the dotted red lines in Figure 4.1, are used. The EMA models from the Rh-Ti system are presented in Figure 3.6 and the modeled refractive indices are listed in Table 3.5. The EMA models and the corresponding optical constants for the Mo-Pt system are provided in Figure 3.7 and Table 3.6, respectively. The two low $-n$ absorber candidates, specifically 21.5% Ti and 65% Pt are chosen for analysis. The 21.5% Ti has a complex refractive index $(n - ik) = 0.8914 - i0.0276$ whereas, the 65% Pt composite has a complex refractive index $(n - ik) = 0.9023 - i0.0413$.

The attenuated phase shifting mask design is identified by determining the optimum mask absorber reflectivity. The optimum absorber reflectivity is in turn determined through the co-optimization of the relative absorber reflectivity and lithography metrics. The NILS is used as a representation of the aerial image contrast. The MEEF is also utilized as a critical lithography metric when designing mask absorbers. The relative absorber

reflectivity is calculated using the *TFCalc* software by modulating the absorber thickness and then normalizing it to the multilayer reflectivity [125]. A multilayer mirror consisting of 40 bilayer pairs of Mo/Si (3nm/4nm) capped with a 2nm Ruthenium capping layer is utilized for reflectivity calculations. It is worth noting that the reflectivity values can be further optimized by regulating the Mo/Si bilayer periodicity within the multilayer mirror.

4.3.1.1   Line/Space Patterns

Figure 4.13 shows a schematic of the absorber optimization scheme used for 1D line/space patterns. Optimized dipole sources calculated using Eq. (4.1) and Eq. (4.2) are used to illuminate the L/S patterns. A 26nm pitch (P26), P28 and P30 at 1:1 DR are used as test cases. Table 4.3 lists the optimized σ_c and σ_r values for respective pitches.
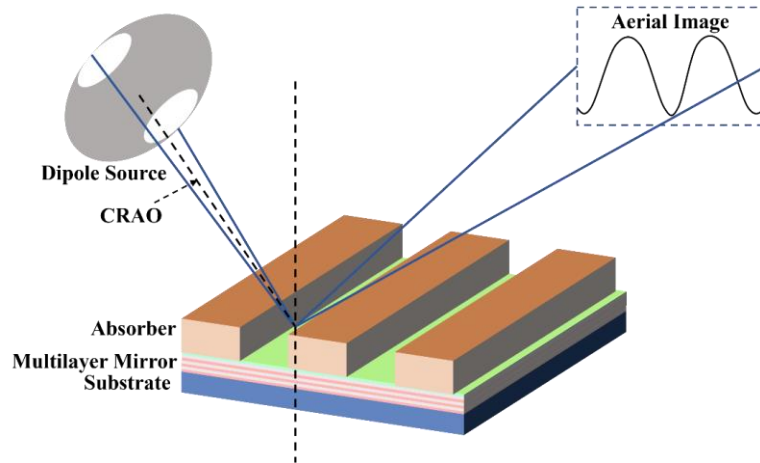
Figure 4.13: Schematic of absorber optimization scheme for 1D line/space pattern. Dipole sources optimized for σ_c and σ_r are used. The mask plane is illuminated at a chief ray angle = 6°

Table 4.3: σ_c and σ_r of optimized dipole sources used for 1D line/space patterns.

Pattern pitch	σ_c	σ_r
26nm	0.786	0.31
28nm	0.730	0.31
30nm	0.681	0.31

In Figure 4.14, the aerial image NILS is plotted against the absorber thickness and the relative absorber reflectivity for the 21.5% Ti absorber candidate. The NILS is plotted at all three pitch values in the 25-55nm absorber thickness range. As observed, the absorber reflectivity increases with a reduction in the absorber thickness. Furthermore, the thickness modulation induced interference effects produces a swing in the absorber reflectivity. This reflectivity swing is in turn translated onto the swing of lithography metrics which is also seen in Figure 4.2. In the desired absorber thickness range (~ 35-50nm), the NILS peaks at all pitches are in phase with the absorber reflectivity peaks. Therefore, a relatively high absorber reflectivity in this thickness range may yield high aerial image contrast.
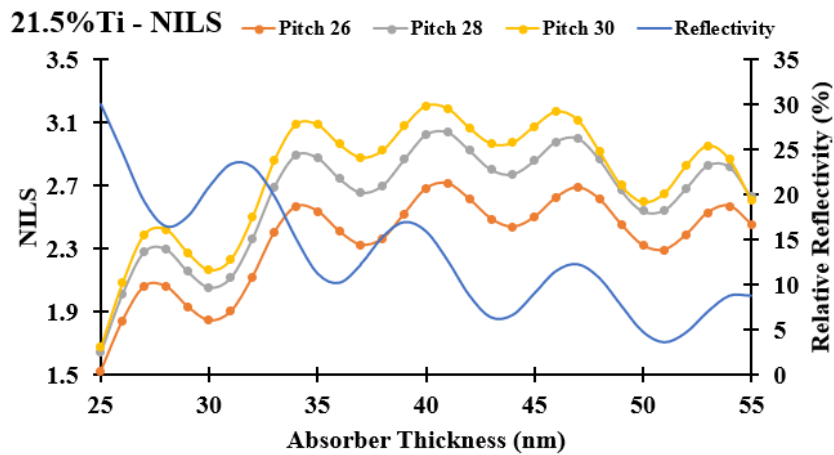
Figure 4.14: Simulated NILS vs absorber thickness and relative reflectivity of the 21.5%Ti, low − n absorber candidate from the Rh-Ti material system for P26, P28 and P30 L/S pattern at 1:1 DR.

Similarly, Figure 4.15 plots the mask error enhancement factor (MEEF) against the absorber thickness and the relative absorber reflectivity for the 21.5% Ti absorber candidate for the same pitch values. In the absorber thickness range of interest, the MEEF swing at all pitches are out of phase with the relative absorber reflectivity and it decreases with an increase in the absorber reflectivity. Therefore, choosing an absorber thickness corresponding to a reflectivity peak will result in high aerial image NILS and low MEEF for 21.5% Ti low − n absorber candidate. For example, an absorber thickness of 40nm in

the case of 21.5% Ti composite will result in a high NILS and a low MEEF at approximately 16% relative absorber reflectivity and at 233º phase shift.
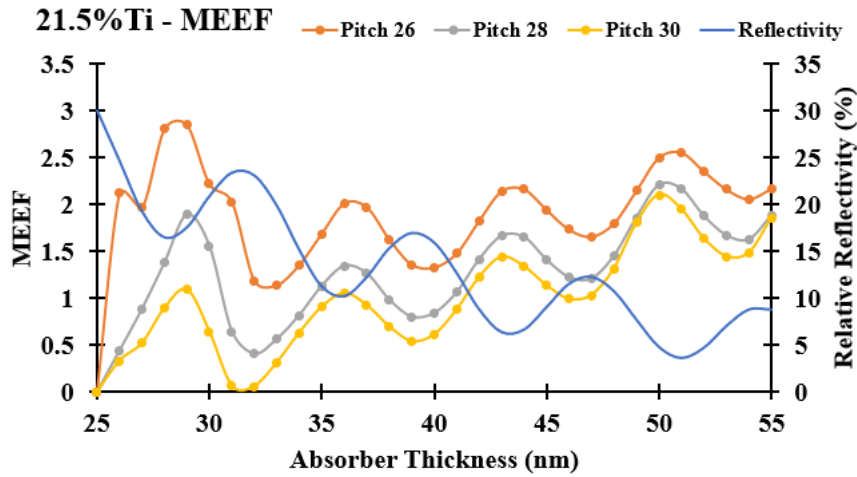
Figure 4.15: Simulated MEEF vs absorber thickness and relative reflectivity of the 21.5%Ti, low – *n* absorber candidate from the Rh-Ti material system for P26, P28 and P30 L/S pattern at 1:1 DR.

The co-optimization approach using the NILS and the MEEF is adopted for the 65% Pt composite from the Mo-Pt material system. The 65% Pt composite has a higher *n* and *k* in comparison to the 21.5% Ti composite. Figure 4.16 shows the NILS through absorber thickness and the relative absorber reflectivity at the three pitch values for the 65% Pt absorber candidate. The relative absorber reflectivity is comparatively lower than the 21.5% Ti candidate due to the higher extinction coefficient of the 65% Pt composite.
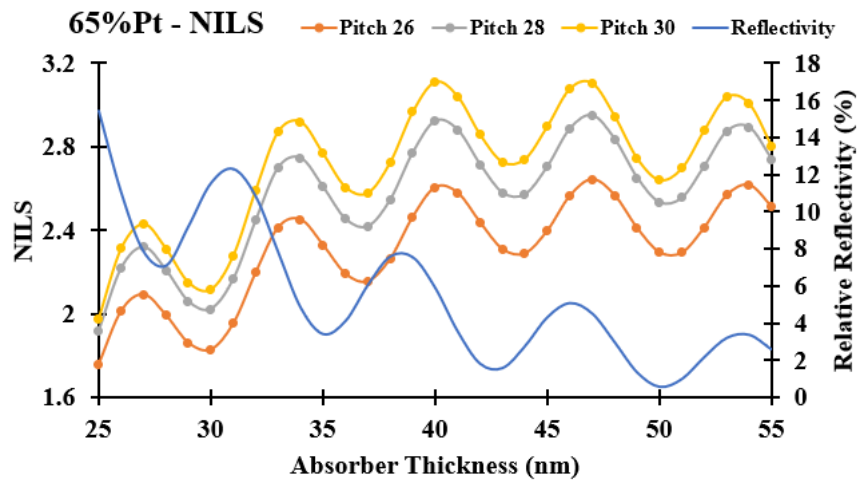
Figure 4.16: Simulated NILS vs absorber thickness and relative reflectivity of the 65%Pt, low – *n* absorber candidate from the Mo-Pt material system for P26, P28 and P30 L/S pattern at 1:1 DR.

From Figure 4.16, it is observed that the NILS is in phase with the relative absorber reflectivity at all pitches in the desired thickness range. In comparison to the 21.5%Ti, the NILS peaks are shifted with respect to reflectivity. The shift in NILS is correlated to the refractive index of the absorber candidate and therefore, it is influenced by the phase shift. In the case of 65%Pt candidate, an absorber thickness corresponding to a reflectivity peak will result in a high aerial image NILS.
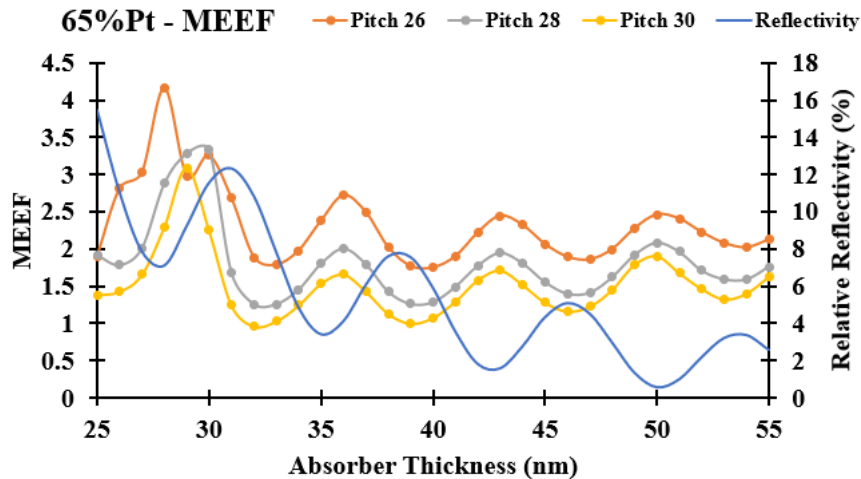
Figure 4.17: Simulated MEEF vs absorber thickness and relative reflectivity of the 65%Pt, low – *n* absorber candidate from the Mo-Pt material system for P26, P28 and P30 L/S pattern at 1:1 DR.

Figure 4.17 shows the MEEF vs absorber thickness and the relative absorber reflectivity at the three pitch values for the 65%Pt composite. Similar to the 21.5%Ti composite, the MEEF and the absorber reflectivity are fortuitously out of phase with each other. Therefore, an absorber thickness corresponding to a reflectivity peak will result in a high NILS and a low MEEF value for the line/spaces patterned using the 65%Pt composite. For example, a 40nm 65%Pt composite generates optimum NILS and MEEF at approximately 6% relative absorber reflectivity and a 210° phase shift. It should be noted that the MEEF can be further reduced by optimizing the illumination source shape and the mask stack. This study employs a 35nm generic EUV resist on a generic EUV hard mask. Nonetheless, a similar MEEF behavior may be expected for an optimized mask stack.

Patterning line/spaces with low − *n* absorber candidates result in a NILS response that is in phase with the absorber reflectivity and a MEEF response that is out of phase with the absorber reflectivity. Therefore, an appropriate absorber thickness corresponding to an absorber reflectivity peak may be selected. In the examples listed above, the corresponding phase shifts for both composites are higher than 180° as discussed earlier.

4.3.1.2   Contact-Holes Pattern

The optimization scheme for the contact-holes pattern is presented in Figure 4.18. Quadrupole sources optimized for σ_c and σ_r are used to illuminate the contact-holes at P36 and P40. In the case of contact-holes, σ_c and σ_r are calculated using Eqs. (4.3) and (4.2), respectively and are tabulated in Table 4.4.
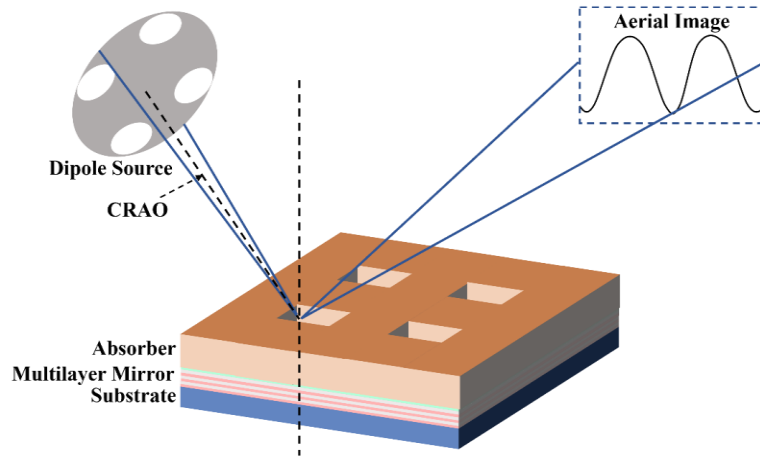
Figure 4.18: Schematic of absorber optimization scheme for a contact-hole pattern. Quadrupole sources optimized for σ_c and σ_r are used. The mask plane is illuminated at a chief ray angle = 6°

$$\sigma_c = \frac{\lambda}{\sqrt{2}pNA_o} \tag{4.3}$$

Table 4.4: σ_c and σ_r of optimized dipole sources used for the contact-holes patterns.

Pattern pitch	σ_c	σ_r
36nm	0.803	0.31
40nm	0.723	0.31

Figure 4.19 and Figure 4.20 show the simulated aerial image NILS and MEEF vs the mask absorber thickness and the relative absorber reflectivity for contact-holes patterns (P36 and P40) simulated using the 21.5% Ti absorber candidate, respectively.
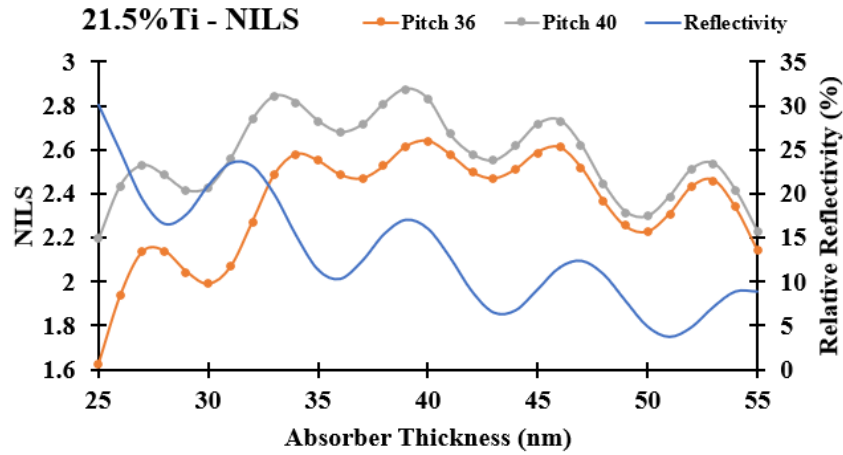
Figure 4.19: Simulated NILS vs absorber thickness and relative reflectivity of the 21.5%Ti, low – *n* absorber candidate from the Rh-Ti material system for P36 and P40 CH pattern at 1:1 DR.

Similar to the line/space patterns, the NILS and the absorber reflectivity are in phase with each other in the desired absorber thickness range. Therefore, an absorber thickness corresponding to a reflectivity peak will result in a high aerial image NILS. Additionally, in the desired thickness range, the NILS trend increases with the reflectivity. Therefore, a high reflectivity is desired for an optimum aerial image NILS.
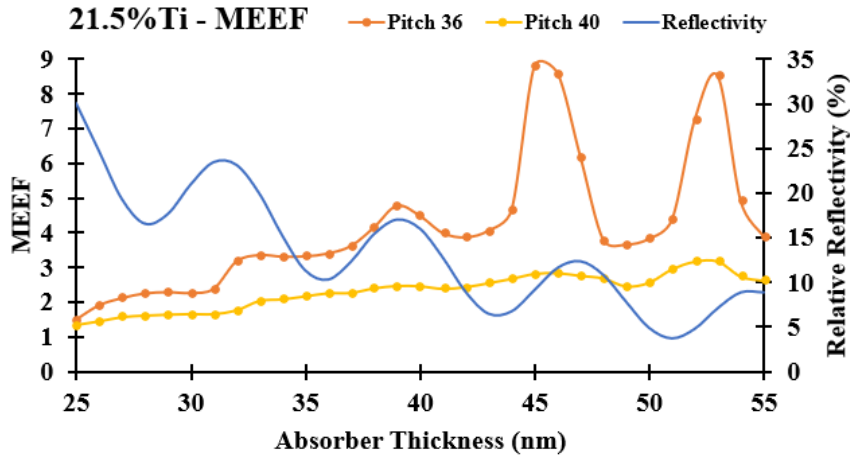
Figure 4.20: Simulated MEEF vs absorber thickness and relative reflectivity of the 21.5%Ti, low – *n* absorber candidate from the Rh-Ti material system for P36 and P40 CH pattern at 1:1 DR.

The MEEF in case of contact-holes is in phase with the relative absorber reflectivity. Additionally, the MEEF decreases with an increase in reflectivity. Therefore, high absorber reflectivity (at low absorber thickness) may be desired for a low MEEF in case of contact-holes.
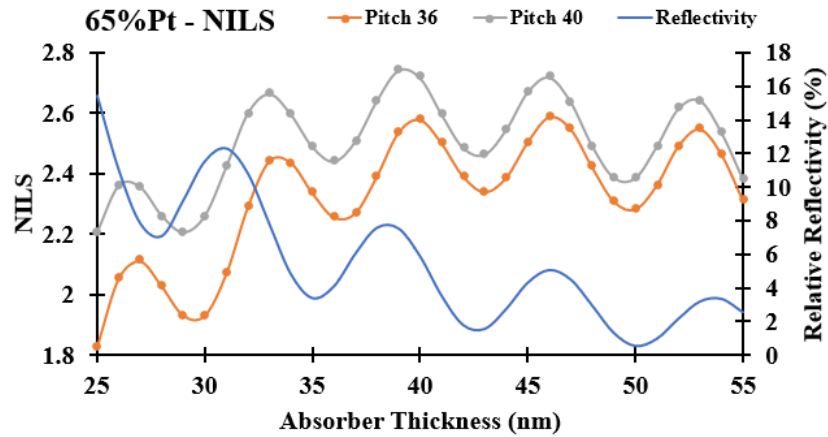
Figure 4.21: Simulated NILS vs absorber thickness and relative reflectivity of the 65%Ti, low – _n_ absorber candidate from the Mo-Pt material system for P36 and P40 CH pattern at 1:1 DR.

Absorber design co-optimization for contact-holes pattern is also investigated for the 65%Pt composite. The NILS/MEEF vs absorber thickness and the relative reflectivity generated through the 65%Pt composite are shown in Figure 4.21 and 4.22, respectively.
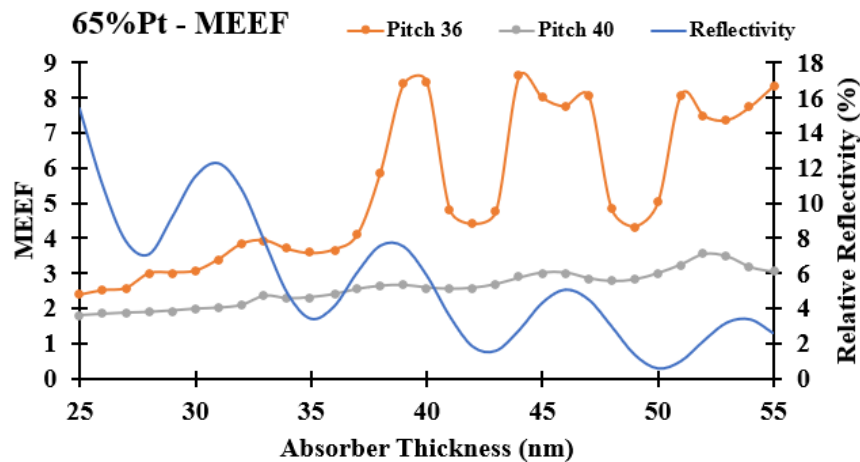
Figure 4.22: Simulated MEEF vs absorber thickness and relative reflectivity of the 65%Pt, low – _n_ absorber candidate from the Mo-Pt material system for P36 and P40 CH pattern at 1:1 DR.

The aerial image NILS and MEEF behavior for the 65%Pt composite is consistent with the 21.5%Ti candidate. The NILS and the MEEF both are in phase with the absorber

reflectivity for dense contact-holes pattern at P36 and P40 in the desired low absorber thickness. Therefore, in the case of contact-holes, an absorber thickness that results in an absorber reflectivity peak may be chosen for high aerial image NILS, if the corresponding MEEF is within the defined tolerance value. As in the case with line/space pattern, the MEEF can be reduced by optimizing the source shape and mask stack. Therefore, an appropriate absorber thickness that results in the desired imaging performance can be identified using the optimum absorber reflectivity. For both line/space and contact-holes patterns, a relatively high absorber reflectivity results in high NILS and low MEEF values.

4.3.1.3   False Contacts

Although a high absorber reflectance is desired for an optimum NILS and MEEF performance, caution must be exercised in determining the appropriate absorber reflectivity to avoid printing false contacts that may lead to stochastic failures [126].
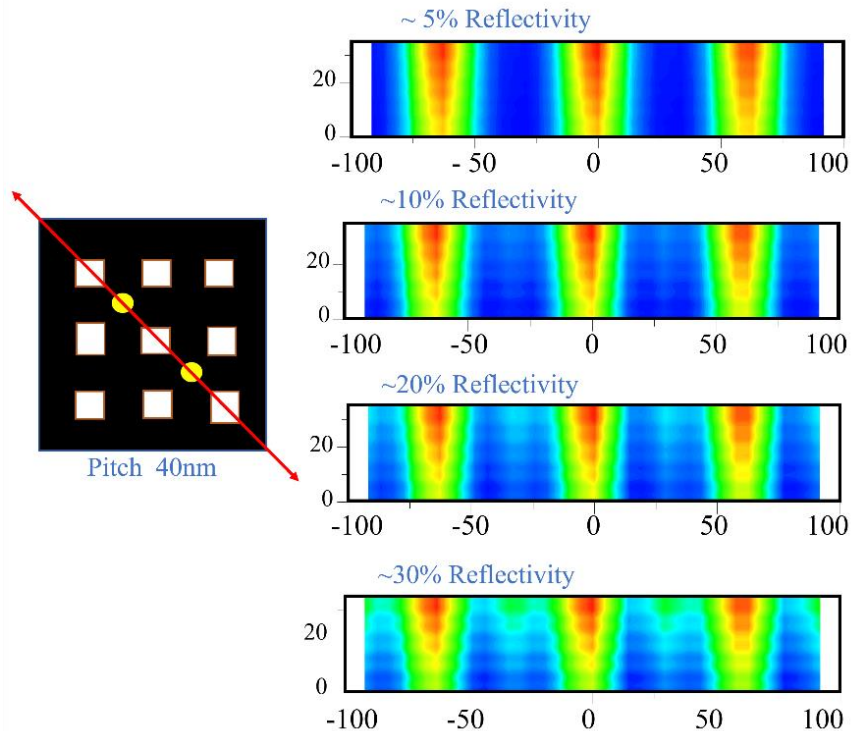
Figure 4.23: Contact-holes imaged on a 35nm generic EUV resist using *Prolith* Simulator. The measurements are observed diagonally as indicated by the red arrow. False contacts appear between the corners of the contacts as depicted by yellow circles.

The effect of false contact holes is demonstrated in Figure 4.23 by plotting the image in the resist as the absorber reflectivity is increased from 5% to 30%. The 20P40 dense contact-hole pattern is simulated by a quadrupole source using the 21.5% Ti absorber candidate. False contacts at diagonal locations (red cutline) begin to appear in the resist for the relative reflectivity values of 20% and above, as indicated by yellow spots. As the absorber reflectivity increases, the intensity of the false contacts (FC) increases and, the relative aerial image (AI) intensity associated with the clear areas of the contact-holes decreases. This can be characterized by using the false contact ratio (FCR) given in Eq. (4.4).

$$FCR = \frac{AI\ Intensity}{FC\ Intensity} \tag{4.4}$$

Figure 4.24 plots the FCR vs absorber thickness and the relative absorber reflectivity for the 21.5% Ti absorber candidate. The FC ratio should be as large as possible to reduce the probability of stochastic failures. Therefore, a trade-off exists between the imaging performance and the FCR ratio. For the low $-n$ absorber candidates, absorber thickness corresponding to reflectivity peaks is desired for optimum imaging performance.
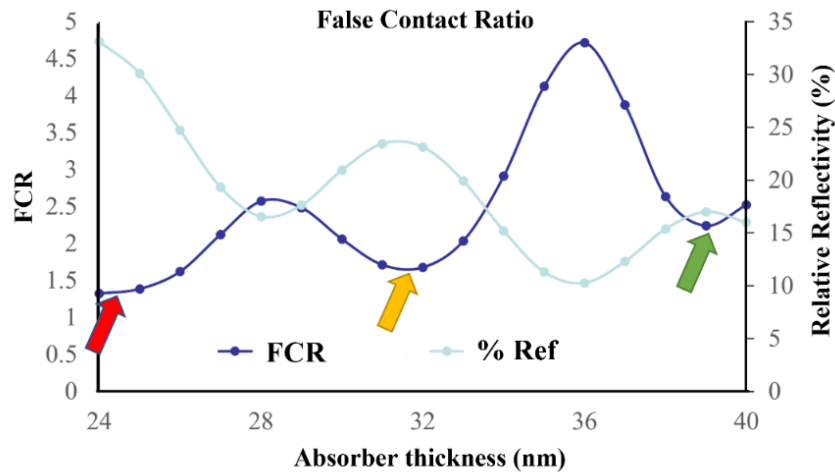
Figure 4.24: False contact intensity characterization using the FCR ratio. A larger FCR ratio is desired to reduce the probability of stochastic failures.

In the example presented in Figure 4.24, three reflectivity peaks are observed. Choosing an absorber thickness near the reflectivity peak as indicated by the green arrow shows a high FCR in comparison to the other two reflectivity peaks. In the case of line/space patterns, sidelobes begin to appear at high absorber reflectivity. From examples above, an optimum absorber reflectivity for EUV lithography is in the range of approximately 10 – 20%. This is also consistent with reflectivity values in Tables 4.1 and 4.2. This range is higher than the conventional optical lithography where the attenuated phase shifting masks have approximately 6% transmission. The choice of optimum absorber reflectivity will dictate the mask absorber thickness and the resulting phase shift.

4.3.1.4   Optimum Phase Shift

The co-optimization of the absorber reflectivity with aerial image NILS and MEEF presented in sections 4.3.1.1 and 4.3.1.2 is applied to the line/space and contact-holes patterns using all the modeled absorber candidates from the Rh-Ti and the Mo-Pt material systems listed in Tables 3.5 & 3.6. Optimized dipole and quadrupole illumination sources are used to simulate the line/space and the contact-hole patterns, respectively. An absorber thickness resulting in a high NILS and a low MEEF at the evaluated pitches (P26, P28, P30 for the line/space patterns and P36, P40 for the contact-hole patterns) is selected from the low thickness range of 30-45nm for all absorber candidates. The resulting phase shifts are plotted against the refractive index (n) of the absorber candidate in Figure 4.25.

From Figure 4.25, it can be observed that the phase shift values are higher than 180º (π) for most absorber candidates. It is also observed that the phase shift at the optimum absorber thickness decreases with an increase in the refractive index of the absorber material. This leads us to the conclusion that modulating n changes the correlation between

the lithography metrics and the absorber reflectivity and hence, influences the phase shift. The phase shift at the optimized absorber thickness for contact-holes is higher than for line/space pattern. This can be attributed to the change in the diffraction angle at the mask for different patterns. Therefore, the absorber material as well as the mask pattern influences the phase shifting requirement for the EUV attenuated phase shifting mask.
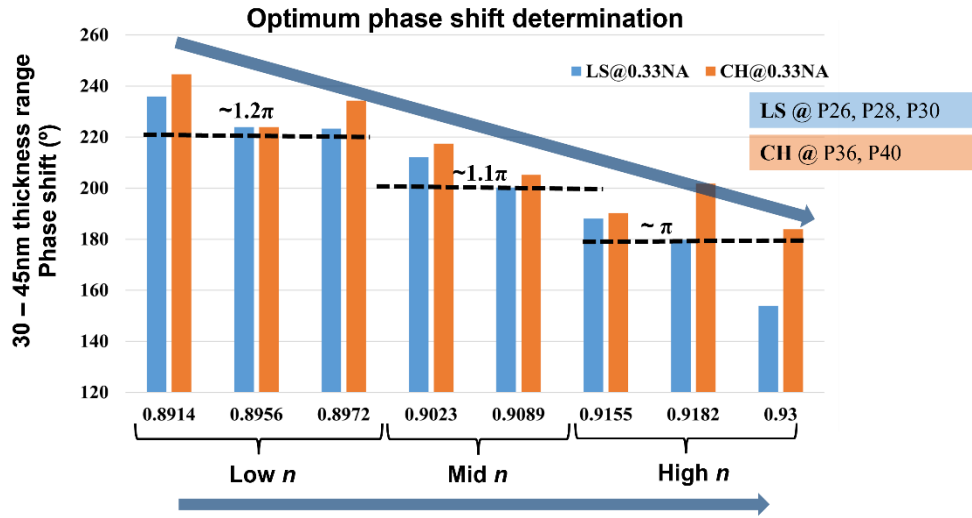
Figure 4.25: Optimum phase shift in 30-45nm absorber thickness range vs absorber refractive index of the absorber candidates from the Rh-Ti and the Mo-Pt material systems. Optimum phase shift for P26, P28 and P30 for line/space pattern is compared with P36 and P40 contact-hole pattern at 0.33NA.

The phase shift at optimum absorber thickness of line/space patterns simulated at 0.33NA (P26, P28 and P30) are also compared to the line/space patterns simulated with 0.55 high-NA anamorphic EUV (P14, P16 and P18). The σ_c and σ_r values of the dipole sources for a 0.55NA system at the corresponding pitches are listed in Table 4.5 and the results are shown in Figure 4.26.

Table 4.5: σ_c and σ_r of optimized dipole sources used for 1D line/space patterns at 0.55NA anamorphic EUV.

Pattern pitch	σ_c	σ_r
14nm	0.876	0.19
16nm	0.767	0.19
18nm	0.681	0.19

In Figure 4.26, apart from the refractive index dependence of the phase shift, it is also observed that the phase shift at optimized absorber thickness for the 0.55NA anamorphic EUV system is higher than at 0.33NA conventional EUV system. This effect is also attributed to the change in the diffraction angle at the mask due to the change in the numerical aperture of the objective lens.
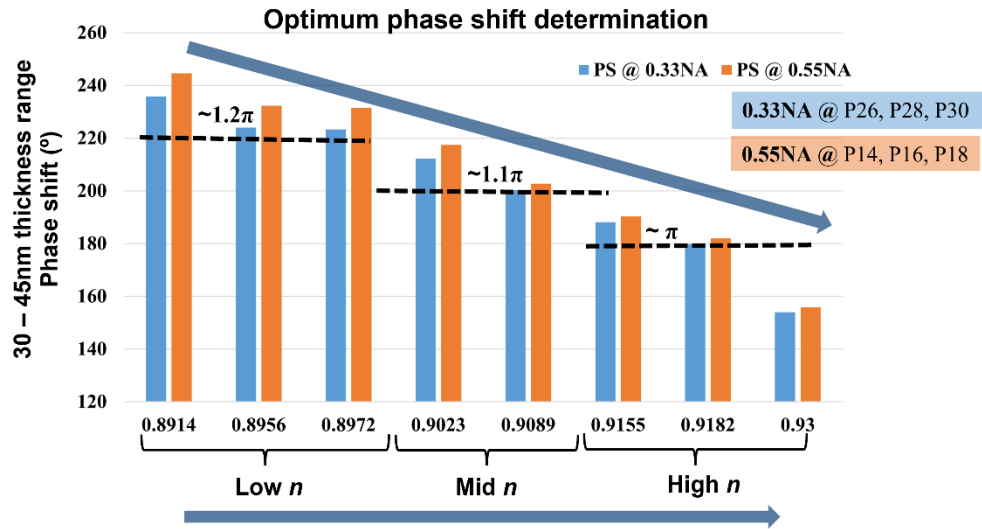
Figure 4.26: Optimum phase shift in 30-45nm absorber thickness range vs absorber refractive index of the absorber candidates from the Rh-Ti and the Mo-Pt material systems. Optimum phase shift for P26, P28 and P30 at 0.33NA is compared with P14, P16 and P18 at 0.55NA.

From Figures 4.25 and 4.26, it can be concluded that the optimum phase shift for the attenuated phase shifting mask in EUV lithography is case specific and must be evaluated. The phase shifting requirement will depend on multiple factors including the absorber material, mask pattern, NA and the absorber reflectivity. For the low $-n$ absorber candidates, the optimum phase shift is in the range of 1.2π (220º) which is consistent with the literature. With the choice of a low $-n$ high reflective mask absorber, special attention must be given to the absorber reflectivity to avoid printing false contacts/sidelobes and reduce the probability of stochastic failures.

The low $-n$ mask absorbers provide high aerial image contrast at low absorber thickness, reducing the impact M3D effects. However, the low $-n$ mask absorbers suffer

from a high pattern induced best-focus variations [127]. Essentially, the best-focus values largely differ for isolated features in comparison to semi-dense and dense mask patterns [128], [129], [121], [130], [131]. Applying a mask bias may not be able to correct the large best-focus shifts at smaller pitches. SRAF insertion may need to be considered for high pattern fidelity and thus increasing the mask complexity.

4.3.2 Index Matched Absorbers

Index matched absorbers with a high k reduce the large best-focus shifts observed in case of low $-n$ attenuated phase shifting mask absorbers [132]. They also reduce contrast fading observed in a multipole imaging setting. Contrast fading is shown in Figure 4.27 for a dipole illumination. In this example, the aerial image formed through the yellow pole does not overlap the aerial image resulting from the red pole. The resulting aerial image formed through the contributions of both poles has lower overall aerial image contrast.
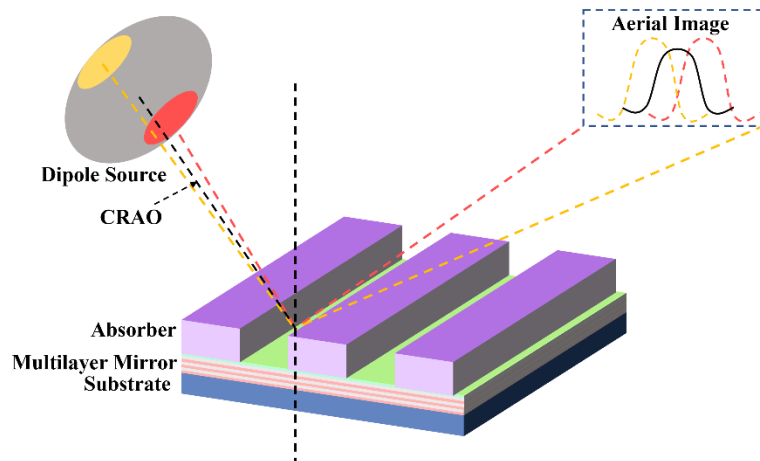
Figure 4.27: Contrast fading observed in the case of dipole illumination. Aerial image from individual poles do not overlap. Index matched absorbers reduce contrast fading.

On the other hand, index matched materials have a relatively low extinction coefficient resulting in lower light absorption at reduced absorber thickness. The index matched absorbers therefore have an inherently low aerial image contrast. For that purpose,

two material systems specifically, the Al-Ni and the Al-Te have been identified. The material systems are highlighted by the dashed green lines in Figure 4.1. Aluminum has a refractive index *n* greater than 1 at 13.5nm wavelength, whereas Ni and Te have high extinction coefficients. Luong et.al. has provided a detailed discussion on the absorber composites from the Al-Ni material system. However, material composites from the Al-Te material system may be better absorber candidates, first because Te has higher *n* & *k* at 13.5nm wavelength, and second Te has shown better volatility in dry etching through RIE. The patterning capabilities for absorber candidates are discussed in detail later.
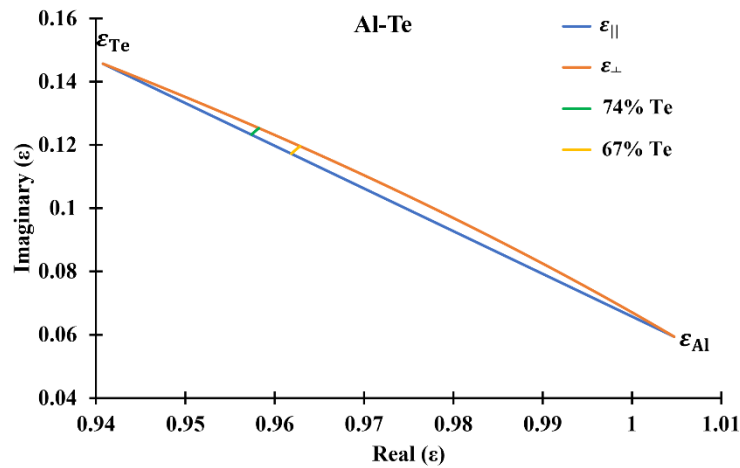
Figure 4.28: The EMA model of absorber candidates from the Al-Te material system. Two material candidates at 67% and 74% Te by volume are identified.

The Wiener bounds and the two EMA models from the Al-Te material system are highlighted in Figure 4.28. Composites with a higher extinction coefficient are presented. The EMA modeled optical constants are listed in Table 4.6. The imaging performance of the two candidates may be comparable due to the proximity of the optical constants.

Table 4.6: Effective dielectric constants and refractive indices EMA modeled of Al-Te composites.

Material Composition	Dielectric constant		Refractive index	
	ε_r	ε_k	*n*	*k*
67%Te	0.9621	0.1180	0.9827	0.0600
74%Te	0.9576	0.1239	0.9806	0.0632

4.3.2.1   Absorber Design

In the case of index matched absorbers, the 74% Te composite (higher extinction co-efficient) is selected for thickness optimization due to higher absorption. For consistency with the attenuated phase shifting mask design, a similar approach for the index matched absorbers has been adopted. The NILS and MEEF co-optimization of the 74% Te absorber candidate for 1:1 DR line/space pattern at P26 is shown in Figure 4.29. The NILS response of this candidate is higher than 2 throughout the observed thickness range (30 – 55nm) except for the first valley near 34nm absorber thickness. The high extinction co-efficient of the candidate absorber enables high aerial image contrast at lower absorber thickness. It is also observed that the NILS and the MEEF are out of phase with respect to one another. Therefore, an appropriate choice of absorber thickness can yield the desired imaging performance. The 74% Te absorber composite has two absorber thicknesses at 38nm and 45nm corresponding to the respective NILS peaks and MEEF valleys in the low absorber thickness range.
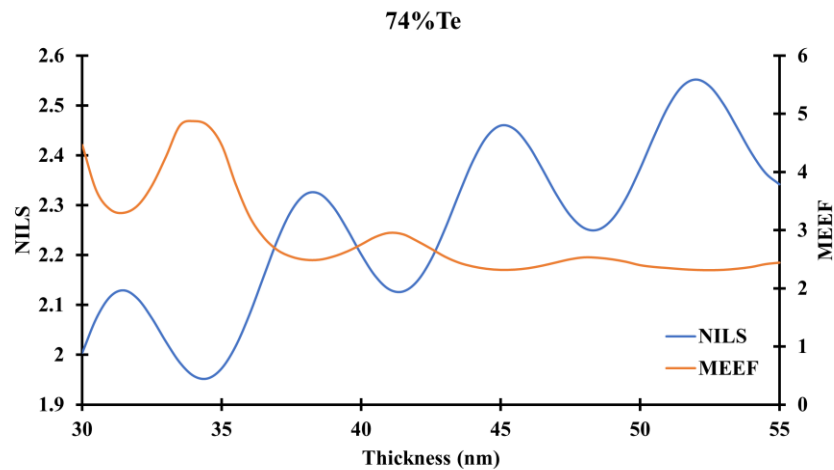
Figure 4.29: Simulated NILS and MEEF co-optimization of the 74% Te absorber for P26 with 1:1 DR. Two thicknesses at 38nm and 45nm can be identified.

Figure 4.30 shows the nearfield intensity responses of the 74% Te candidate at 45nm absorber thickness plotted at 6º and 10º propagation angles for a 20P40 dense contact hole

pattern. As the 74% Te absorber candidate has a higher extinction coefficient compared to the Ta-based and the low $-n$ absorber, the reflected intensity is lower. However, the relative intensity loss in the open region is lower than the intensity loss in the case of the Ta-based absorber. This is clearly evident at the larger propagation angle. The reflected nearfield intensity plots for a 61nm TaBN absorber and a 42.5nm low $-n$ Rh$_5$Ti absorber are provided in Figures 4.7 and 4.8, respectively. Therefore, the index matched absorbers may have a reduced impact of the illumination and layout conditions on the ML reflectivity. The low $-n$ absorber has the best performance at both angles. The amount of light loss observed for the index matched absorber candidate is higher in comparison. However, the light loss in case of $n \approx 1$ absorber can be reduced by using a thinner absorber.

45nm 74% Te Absorber
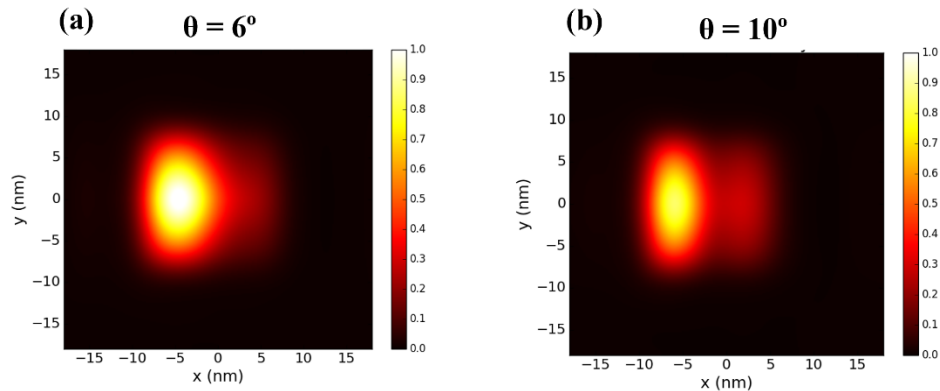
Figure 4.30: Reflected nearfield intensities for a 40nm pitch contact-holes pattern with a 20nm opening imaged using the 74%Te absorber candidate at propagation angle θ (a) 6º and (b) 10º.

4.4 Absorber Patterning

EUV mask manufacturing is primarily a two-step process. First is the multilayer mask blank deposition which is then followed by patterning the mask absorber. Mask absorber patterning is a key process that determines the ever-stringent mask design requirements such as CD bias uniformity, line width roughness (LWR), sidewall angles and low surface roughness.

4.4.1 Existing Technology

The current state-of-the-art EUV mask uses a Ta-based absorber stack. The absorber stack on top of the Ru capping layer consists of a lower Ta-based absorber and an upper Ta-based anti-reflection coating. For patterning, the absorber stack is coated with a chemically amplified e-beam resist. The photoresist is exposed using an e-beam mask writer, typically in the range of 50 KV. Following resist development, the underlying absorber layer is then etched via a plasma-based etch process. Reactive Ion Etching (RIE) is usually used with CF_4 and/or Cl_2 gas based chemical assistance [133]–[135]. The residual photoresist is then stripped through wet etching techniques. The Ru capping layer that prevents oxidation of the underlying multilayer mirror also functions as a hard-mask (HM) with high etch selectivity to the Ta-based absorber. A TaN:Ru etch selectivity of 100:1 has been previously reported [136]. High etch selectivity between the absorber stack and the multilayer mirror can enable the desired large process windows for over-etching.

Introducing novel absorber stacks therefore needs consideration of the patterning processes to meet the standard requirements. We investigate two main patterning approaches that can be implemented for novel EUV mask absorbers, specifically the subtractive and the additive pattering techniques.

4.4.2 Subtractive Patterning

The existing mask patterning technology for a Ta-based mask absorber described above is a subtractive patterning technique. A typical process flow for the subtractive patterning technique is shown in Figure 4.31. In the case of alternative absorber candidates, the absorber material is typically a metal or a metal composite. The metal absorber is etched using a plasma-based etching technique such as inductively coupled plasma reactive ion-

etch (ICP-RIE). RIE is a physical etching technique with chemical assistance. In RIE, the chemical gas forms a volatile compound with the metal, making it a highly selective etching process while the physical aspect of the etching technique enables anisotropic profiles.
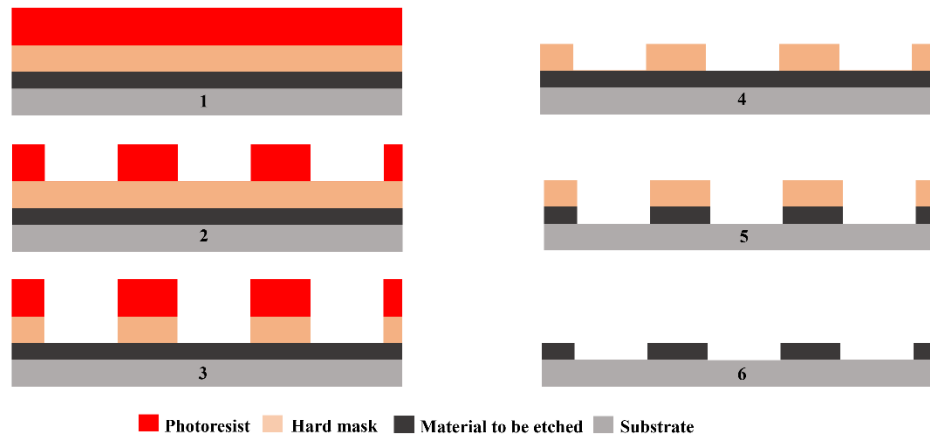
Figure 4.31: Subtractive patterning process. The numbers indicate the process flow sequence. Red layer is the photoresist, orange layer is the hard mask, dark gray is the material to be etched and light grey is the substrate.

Most of the metals discussed in this study are implemented in the semiconductor manufacturing processes with known etching chemistries. Molybdenum can be etched using the ICP-RIE approach through Cl_2, CF_4 and SF_6 halogen plasmas. The dry etching of Mo in a Cl_2 plasma is shown to be driven by the chemical assistance of Cl atoms in the plasma. In the case of CF_4 and SF_6 based plasmas, enhanced etch rates are observed with the addition of O_2 [137]. Similarly, metals such as Al and Ti are also extensively used in semiconductor manufacturing. Dry etching techniques with chemical assistance for such metals are exhaustively studied [138]–[141].

Ruthenium is used as the capping layer in the EUV mask stack and is a strong low – n attPSM absorber candidate. Dry etching of Ru using the ICP-RIE approach has been extensively investigated. Through the combination of Cl_2 and O_2 plasmas, an anisotropic profile with 90º sidewall angles for Ru lines can be achieved. At optimized etching

conditions, a high etch selectivity with SiO_2 hard mask has been demonstrated. The chemical etching of Ru is achieved by the formation of RuO_4 volatile compound in the O_2 plasma [142].

Chemical etching of Te and Te-based compounds as absorber candidates have shown promising results. Chemical etching (without a carrier gas) of Te, PtTe and $TaTe_2$ candidates in a halogen-based plasma resulted in isotropic etch profiles. Adding a carrier gas for dry physical etching can enable anisotropic etch profiles with high sidewall angles [143].

Etching metal composites through selective etching techniques with known chemistry is challenging for non-reactive elements such as Ni, Pt and Rh [143]–[145]. Previous attempts to etch Ni without a hard mask resulted in re-sputtering of Ni particles on the resist sidewalls leading to resist fencing [146]. Addition of a hard mask between the photoresist eliminated resist fences however, the physical etching process is not selective with the Ru capping layer.

A novel patterning approach to selectively etch Ni absorber thin films using cyclic RIE process followed by a cyclic atomic layer etch (ALE) has been recently identified [147], [148]. A 40nm Ni thin film is etched through an RIE process using chlorine plasma. This is followed by exposure to a hydrogen-based plasma. Introducing hydrogen atoms enhances the removal of metal chlorides such as $NiCl_x$ in this case. This cyclic RIE process is repeated until the desired isotropic absorber profile is achieved. Following the RIE processes, the samples are subjected to oxidation and thermal ALE by gas phase formic acid. The oxidation step oxidizes the Ni and Ni compounds on the sidewall of the absorber. The etch selectivity of NiO to Ni in thermal ALE is approximately 100. Therefore, the

subsequent ALE process is self-limiting. Through cyclic oxidation – ALE exposures, an anisotropic absorber profiles are observed.

Similar approaches may be identified to selectively etch other non-reactive metals such as Pt and Rh. Enhanced dry chemical etching in combination with a physical RIE process can be implemented to obtain desired pattern profiles. A study showed dry chemical etch of Pt using CO with Cl_2 gases [149]. Chlorination of the Pt thin film is followed by carbonation to form a volatile $PtCl_2(CO)_2$ compound. Sequential Cl_2 and CO exposures may be used to selectively remove the Pt for EUV absorber patterning.

4.4.3 Additive Patterning

Another approach to patterning a mask absorber is by using an additive patterning technique. Additive patterning eliminates the issues with more conventional subtractive patterning techniques such as resist fencing and etch-stop detection. Figure 4.32 shows the process flow for additive patterning.
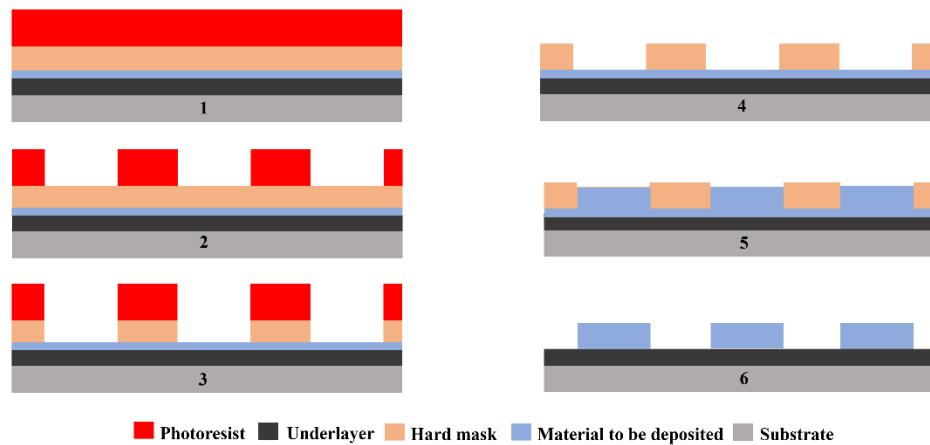
Figure 4.32: Additive patterning process. The numbers indicate the process flow sequence. Red layer is the photoresist, orange layer is the hard mask, blue is the material to be deposited, dark gray is the underlayer and light grey is the substrate.

Additive patterning techniques implement area selective deposition (ASD) [150]–[153]. The sacrificial hard mask, which can be any dielectric material such as SiO_2, is

deposited on a thin seed layer of the desired material [154]. The sacrificial mask layer is then patterned using a lithography process. The image transferred on the sacrificial hard mask is the negative of the mask pattern. ASD is then utilized to selectively fill the trenches in the hard mask layer. Finally, a dry etch processing step removes the seed layer from the surface.

ASD is referred to as any physical or chemical deposition technique that enables controlled deposition of a desired material. ASD encompasses advanced deposition techniques such as atomic layer deposition (ALD) and molecular layer deposition (MLD). ASD allows film formation in one region of the surface while avoiding film deposition in the adjacent areas. Multiple approaches have been proposed for ASD techniques. Figure 4.30 shows the metal on dielectric approach. Some other methods include metal on metal, dielectric on metal and dielectric on dielectric [155]. For EUV mask absorbers, metal on metal and metal on dielectric approaches have been adopted. A Co layer for a 200 nm pitch line/space pattern has been selectively deposited using the electroless deposition technique on a thin Ru layer using an SiO_2 film as the sacrificial layer [143].

The sidewall profile of the absorber depends on the profile of the sacrificial dielectric. Etching of the dielectric is therefore a critical process to achieve desired feature dimensions. Additionally, the removal of the dielectric layer after an ASD must also be optimized. Unetched dielectric materials on the sidewalls of the absorber material may lead to undesirable CD non-uniformity. Another major challenge for additive patterning techniques includes thickness uniformity. Uniform thickness is essential for attPSM absorber candidates for optimum phase and reflectivity. Additional optimization and testing of the ASD process for absorber candidates is required.

Lift-off is a well-known additive micropatterning technique [156]–[160]. In a typical lift-off process, the material is deposited after the pattern is transferred on to the sacrificial mask layer. Figure 4.33 shows a sketch of the lift-off process. The sacrificial hard mask in this case may not be necessary. The photoresist can act as a hard mask.

■ Photoresist ■ Underlayer ■ Hard mask ■ Material to be deposited ■ Substrate
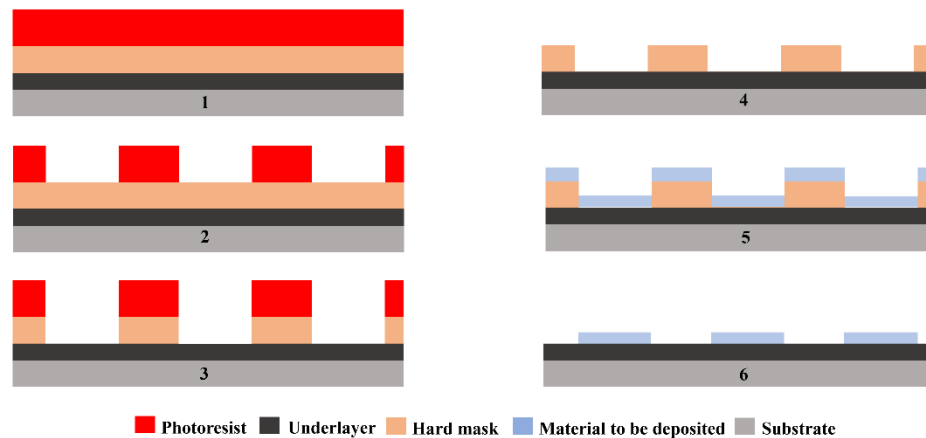
Figure 4.33: Lift-off patterning process. The numbers indicate the process flow sequence. Red layer is the photoresist, orange layer is the hard mask, blue is the material to be deposited, dark gray is the underlayer and light grey is the substrate.

A major challenge in the lift-off patterning process is the thickness uniformity of the patterned features. In case of isotropic deposition, the material may adhere to the sidewall of the sacrificial mask layer leading to a tapered profile of the features, as shown in Figure 4.34. To achieve planar structures, a planarization process is necessary. Techniques such as etch-back and chemical-mechanical polishing are widely used in conjunction with the lift-off process.

One approach to achieve planar structures is by using an isotropic sacrificial layer profile as shown in Figure 4.35. In this case, the deposition material does not encounter the

114

sidewalls of the sacrificial layer. However, controlling the width of the structures is challenging [161].

Underlayer **Hard mask** **Material to be deposited** **Substrate**
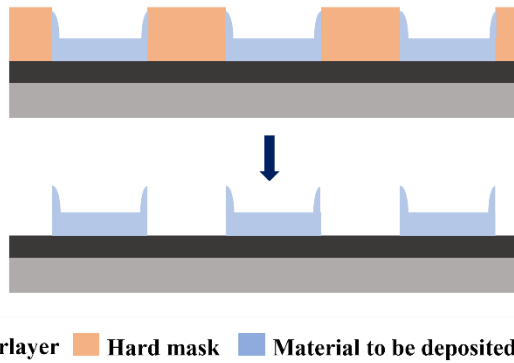
Figure 4.34: Lift-off patterning process with tapered profile structures. Orange layer is the hard mask, blue is the material to be deposited, dark gray is the underlayer and light grey is the substrate.

Through novel patterning approaches such as ALE in subtractive patterning and ASD in the case of additive patterning, alternative mask absorbers for EUVL can be realized. Implementing these processes for high volume manufacturing of EUVL masks still needs further technology maturation to obtain uniform, anisotropic absorber pattern with low mask defect density and linewidth roughness.

Underlayer **Hard mask** **Material to be deposited** **Substrate**
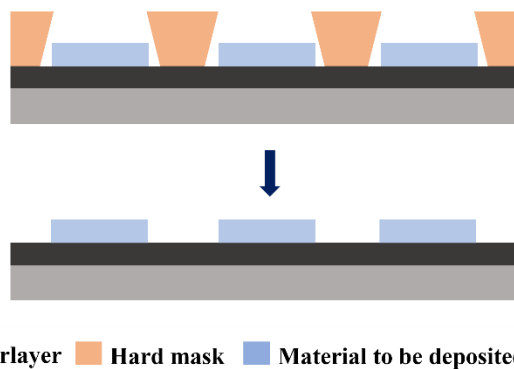
Figure 4.35: Lift-off patterning process with isotropic hard mask profile. Orange layer is the hard mask, blue is the material to be deposited, dark gray is the underlayer and light grey is the substrate.

5 Conclusions

Many studies have shown the potential benefits of employing alternative mask absorbers for EUV lithography. Through alternative mask technologies, a thinner mask absorber can reduce some of the inherent EUV M3D effects and improve the overall performance of the imaging system. Additionally, implementing novel mask absorber technologies can extend 0.33NA EUVL to next generation semiconductor technological nodes before the adaptation of 0.55 high-NA anamorphic EUV lithography systems for high volume manufacturing. Alternative mask absorbers can then be implemented in the high-NA EUV mask by adjusting the absorber design such as thickness, phase shift and reflectivity.

This report investigates alternative mask absorbers for EUV lithography by first identifying the absorber material systems and candidates through dielectric constant modeling and the effective media approximation model. Dielectric constant modeling identifies the range of effective dielectric constants for all compositions of homogeneous elemental materials in the dielectric constant domain. The EMA model is then used to identify the exact value of the effective dielectric constant of the heterogeneous composite for a given volume composition of its constituents. The EMA model employed accounts for the material depolarization effects of the surrounding media on the modeled sample using a material depolarization factor. The modeled effective dielectric constant is then translated to the effective refractive index of the absorber composite.

Six binary refractory metal systems, specifically, Rh-Ti, Rh-Ta, Mo-Pt, Pt-Ti, Mo-Ni and Ru-Te have been identified. The material systems are selected such that the absorber

candidates resulting from these systems have a wide range of effective dielectric constants (and refractive indices). Of the six material systems, nine absorber candidates are modeled as alloys using the EMA model. The volume fractions of the EMA modeled composites are calculated using the respective weight and atomic fractions of the alloy from the thermodynamic phase diagrams. Table 5.1 lists the nine EMA modeled absorber candidates with the corresponding complex dielectric constants and refractive indices. Among these, materials with high extinction coefficient such as $RuTe_2$ and $MoNi_4$ are the high $-k$ absorber candidates. On the other hand, materials with low refractive index and low extinction coefficient, such as Rh_5Ti and Rh_3Ta are the high reflectivity attenuated phase shifting absorbers.

Table 5.1: EMA modeled absorber candidates and corresponding complex dielectric constants and refractive indices.

Material Composition	Dielectric constant		Refractive index	
	ε_r	ε_k	n	k
$RuTe_2$	0.9152	0.1252	0.9588	0.0653
MoNi	0.8708	0.0612	0.9337	0.0328
$MoNi_4$	0.8836	0.1017	0.9415	0.0540
PtTi	0.8505	0.0666	0.9229	0.0361
$PtTi_3$	0.8824	0.0442	0.9396	0.0235
Rh_3Ta	0.8057	0.0575	0.8982	0.0320
MoPt	0.8240	0.0577	0.9083	0.0317
$MoPt_2$	0.8128	0.0741	0.9025	0.0410
Rh_5Ti	0.7938	0.0492	0.8914	0.0276

Absorbers candidates from Table 5.1 are characterized by using the simulations of aerial image contrast and nearfield imaging. Through aerial image simulations, two low absorber thickness zones of high aerial image NILS, specifically 32-37nm and 39-44nm, are identified. High $-k$ absorber candidates generate high aerial image NILS in the

relatively lower absorber thickness range whereas low $-n$ absorber candidates generate high aerial image NILS in both absorber thickness regions.

Nearfield simulations on the best performing absorbers from both thickness regions show a trade-off between shadowing and intensity imbalance in the absorber. Low absorber thickness results in lower shadowing but at a cost of high intensity imbalance. A similar trade-off is observed based on the extinction coefficient of the mask absorber. Higher extinction coefficient of the absorber candidate results in a low intensity imbalance in the absorber region at the cost of additional shadowing. It is also found that a low extinction coefficient of the mask absorber leads to low intensity loss in the open regions (reflective multilayer region) of the mask. Therefore, in the case of dark field masks, absorber candidates with higher extinction coefficients may be preferred for isolated patterns whereas for dense patterns, an absorber candidate with low extinction coefficient may be more suitable.

Nearfield phase response investigations showed large phase deviations at the absorber edge in the low absorber thickness range at 6° propagation angle. Additionally, the low $-n$ absorber candidates produce a non-uniform phase response due to intensity imbalance in the absorber region. In contrast, high $-k$ mask absorbers had uniform phase in the absorber region but resulted in unexpectedly large phase shifts due to high reflectivity at low absorber thickness. Increasing the propagation angle to 10° negatively impacts the phase responses of all absorber candidates. In the larger thickness region, all absorber candidates generate a comparatively stable phase response at 6° and 10° propagation angles. The phase deformation in the absorber region corresponding to the intensity imbalance is also suppressed in the larger thickness region. From the results of

nearfield intensity and phase, it is concluded that the optimum absorber thickness is in the range of 40 – 45nm.

The EMA model is validated through multilayer thin film deposition and ellipsometry in the UV-VIS-NearIR spectrum. The optical constants of the multilayer composites are modeled at inspection 800nm wavelength using the EMA and compared to the measured optical constants of the deposited multilayer stacks. Therefore, the individual thin films thickness does not exceed 80nm ($1/10^{th} \times$ wavelength) to satisfy the EMA model requirement. Multilayer composites from Mo-Ni, Mo-W and Al(1%Si)-Ni material systems are deposited using PVD-sputtering techniques. Total multilayer thicknesses are verified using a KLA Tencor's P2 profilometer and the optical constants are measured using a J.A. Woollam Variable Angle Spectroscopic Ellipsometer (VASE).

Three multilayer composites from the Mo-Ni material systems are deposited using the PVD-75B RF magnetron sputtering system at the RIT Nano Power Research Labs (NPRL). The multilayer composites have 20%, 50% and 90% Ni by volume. The verification results show excellent agreement between the EMA modeled and measured optical constants for 20% Ni and 50% Ni composites. The measured *n* and *k* of the 90% Ni composite does not match the corresponding EMA modeled values due to high surface roughness of the sample resulting from deposition chamber impurities and change in deposition conditions.

The multilayer composites from the Mo-W and Al(1%Si)-Ni material systems are deposited using the CVC-601 DC sputter system at the RIT Nanolabs. For the Mo-W material system, two material composites with 45% and 70% W by volume are deposited for EMA model validation. Similarly, 45% and 75% Ni by volume are deposited from the

Al(1%Si)-Ni material system. The verification results showed good agreement between the EMA modeled and measured values for all multilayer samples except the 45%Ni composite from the Al(1%Si)-Ni material system. This is attributed to the cracking of Ni sputter target at the racetrack during the deposition run. Table 5.2 provides a summary of verification results for all the multilayer composites in this study.

Table 5.2: EMA Model verification results from Mo-Ni, Mo-W and Al-Ni multilayer systems at 800nm inspection wavelength.

Material System	Composition %	Modeled		Measured	
		n	k	n	k
Mo-Ni	20%Ni	2.597	0.652	2.541	0.659
	50%Ni	2.805	0.866	2.812	0.870
	90%Ni	3.082	1.183	3.346	1.398
Mo-W	45%W	3.578	3.427	3.579	3.285
	70%W	3.643	3.293	3.633	3.206
Al-Ni	45%Ni	2.134	5.161	2.352	4.764
	75%Ni	2.452	4.821	2.473	4.600

The model agreement is especially good for the Mo-Ni material system (20%Ni and 50%Ni). This is because of the superior deposition capabilities and lower chamber base pressure of the PVD-75B sputter system. The CVC-601 sputter system has a substantially larger deposition chamber and hence, it has a higher base pressure. The EMA validation results show that the model accuracy can be further improved by improving the thin film deposition capability. The validation results also provide reasonable confidence in employing the EMA model at EUV wavelength for mask absorber modeling.

Finally, the absorber design characterization is considered for an attenuated phase shifting mask absorber and an index matched absorber. For attenuated phase shifting masks, absorber designs are identified through co-optimization of lithography metrics (NILS and MEEF) with the relative absorber reflectivity. For line/space patterns imaged using low – n absorber candidates, the resulting aerial image NILS is found to be in phase

with the relative absorber reflectivity in the 35-50nm desired absorber thickness range. The high aerial image NILS in this thickness range is influenced by the combination of low refractive index n and absorber reflectivity and hence, the resulting phase shift. On the other hand, MEEF is out of phase with the relative absorber reflectivity in the same thickness range. Therefore, it is concluded that choosing an absorber thickness corresponding to absorber reflectivity peak results in optimum NILS and MEEF for line/space patterns. In the case of dense contact-holes, NILS and MEEF both are in phase with the relative absorber reflectivity in the desired absorber thickness range. Therefore, an absorber thickness corresponding to the absorber reflectivity peak may be chosen if the resulting MEEF is within the defined tolerances.

High mask absorber reflectivity can result in false contacts and sidelobes for contact-holes and line/spaces patterns, respectively. To avoid printing unwanted features and reduce the probability of stochastic failures, False Contact Ratio (FCR) is introduced. High FCR is desired for failure free imaging. Through FCR simulations, the optimum relative absorber reflectivity in the range of 10-20 % is identified for low – n attPSM absorbers in EUV lithography.

The absorber design co-optimization is implemented on absorber candidates with a range of refractive index (n) values to identify optimum phase shift for attenuated phase shifting mask absorbers in EUV. It is found that the optimum phase shift in the desired absorber thickness range decreases with an increase in refractive index n. Additionally, the phase shift requirement is higher for contact hole patterns compared to the line/space patterns. It is also found that the optimum phase shift increases with an increase in the NA of the objective lens from 0.33 to 0.55. This is attributed to the increase in the diffraction

angle at the mask introduced by increases in NA. It is therefore concluded that the desired phase shift is a function of absorber material, diffraction angle, mask pattern and absorber reflectivity. The phase shift requirement of the reflective EUV lithography is higher (>180° or π) in comparison to the refractive DUV lithography. The optimum phase shift in EUV for the attSPM using the low $- n$ is approximately 220° (or 1.2π).

The low $- n$, low $- k$ attenuated phase shifting mask absorbers are prone to large best-focus variations through pitch. Biasing isolated features to correct such large focus variations lead to CD non-uniformity which is extremely critical for small feature dimensions. Therefore, as an alternative, index matched absorber candidates with high extinction coefficient from the Al-Te material system are proposed as promising absorber candidates for EUV lithography. Al has a refractive index greater than 1 whereas Te has a high extinction coefficient at 13.5nm wavelength. The high refractive index ($n \approx 1$) of the absorber candidates reduces contrast fading and best-focus variations. On the other hand, the high extinction coefficient has the potential to increase the aerial image contrast at reduced absorber thickness. Using the EMA model and lithography simulations, a 45nm 74% Te composite is identified as a potential index matched absorber.

This thesis has demonstrated with examples, the ability to identify and characterize any EUV mask absorber material for alternative mask technologies. However, a substantial amount of work remains before introducing an alternative mask absorber for high-volume manufacturing. The complete potential of the individual candidates must be realized by source mask optimization (SMO) and optical proximity corrections (OPC) on a critical layout using computational lithography infrastructure.

In the area of mask manufacturing, the accuracy of the EMA model at 13.5nm EUV wavelength remains to be determined. Measurements of the optical constants of EMA modeled absorber candidates using techniques such as x-ray reflectometry and EUV reflectometry should be performed. The material polarization of the underlying multilayer and its effect on the optical properties of the absorber candidate should also be determined, thus improving the EMA model accuracy.

6 Appendix A

Figure 6.1 plots the nearfield distribution images for all the absorber candidates from Table 4.1. The images are generated at 2º, 6º and 10º propagation angles for a 13P100 isolated line/space pattern.
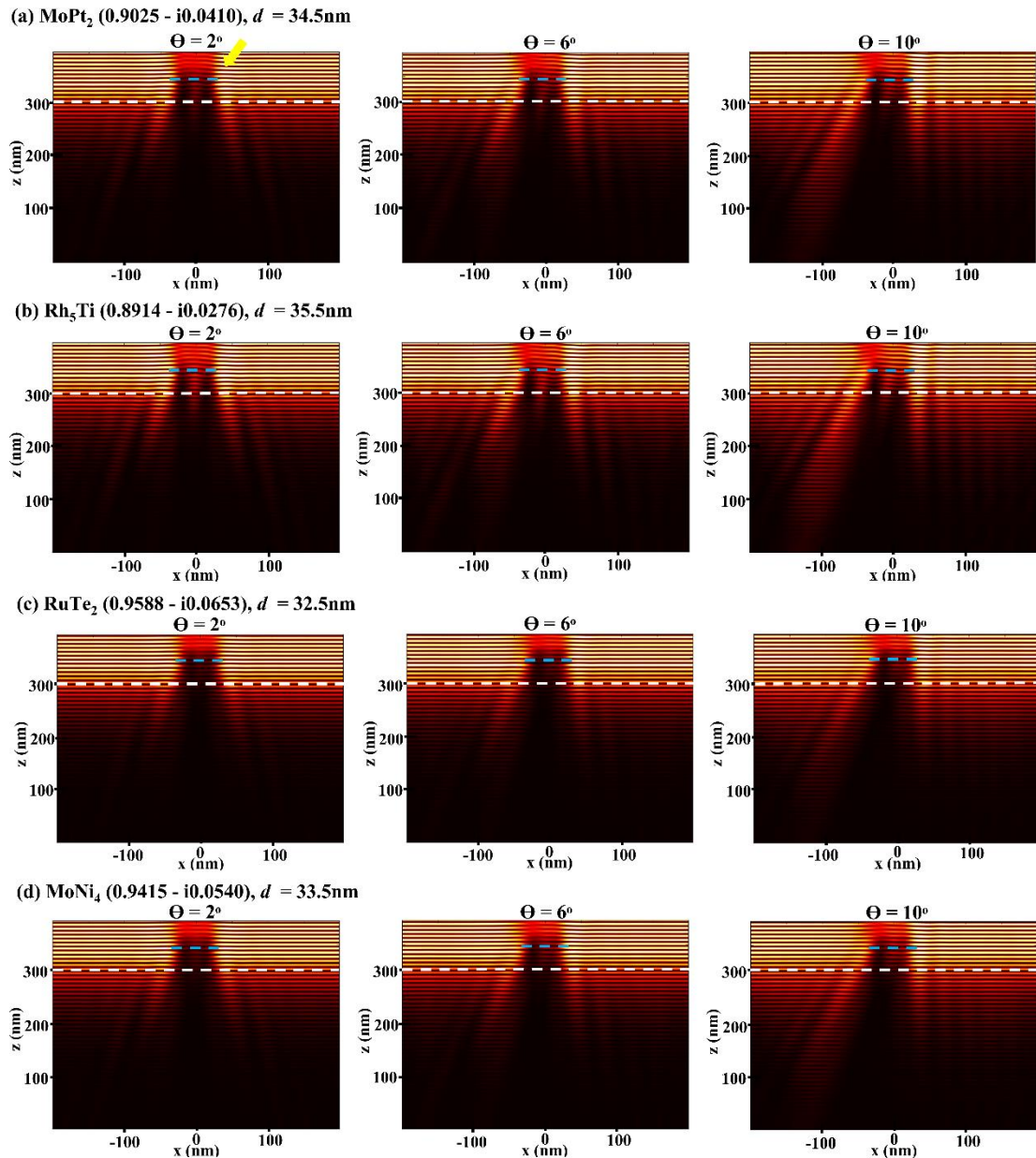
Figure 6.1: Nearfield Intensity of all the absorber candidates from Table 4.1. The intensities are plotted at 2º, 6º and 10º propagation angles for a 13P100 isolated line/space pattern.

Figure 6.2 plots the nearfield distributions for all the absorber candidates from Table 4.2. The images are generated at 2º, 6º and 10º propagation angles for a 13P100 isolated line/space pattern.

(a) Rh₅Ti (0.8914 - i0.0276), *d* = 42.5nm

(b) MoPt₂ (0.9025 - i0.0410), *d* = 41.5nm

(c) Rh₃Ta (0.8982 - i0.0320), *d* = 42nm

(d) MoPt (0.9083 - i0.0317), *d* = 42nm
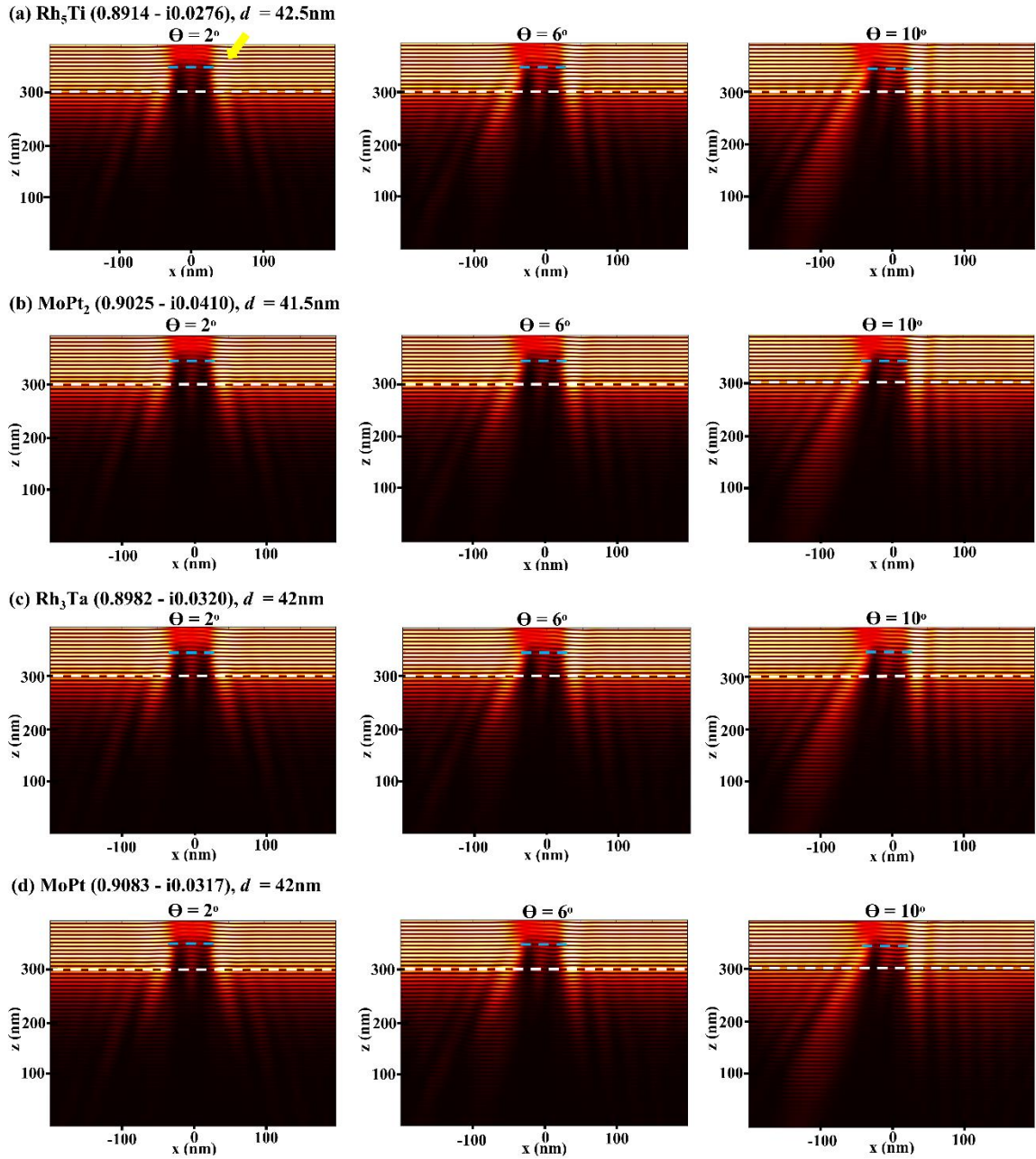
Figure 6.2: Nearfield Intensity of all the absorber candidates from Table 4.2. The intensities are plotted at 2º, 6º and 10º propagation angles for a 13P100 isolated line/space pattern.

In Figures 6.1 and 6.2, the white dashed lines highlight the top of multilayer mirror, and the blue dashed lines indicate the top of absorber layer. It is observed that increasing the propagation angle leads to an enhanced shadowing effect and the intensity imbalance in the absorber layer. It is also observed that increasing the absorber thickness results in more shadowing effect but low intensity imbalance in the absorber layer. Therefore, a trade-off based on the absorber thickness is observed between the shadowing and the intensity imbalance.

Similarly, a trade-off between the shadowing and the intensity imbalance also exists based on the extinction coefficient of the mask absorber. Absorbers with a relatively high extinction coefficient experience reduced intensity imbalance in the absorber region at the expense of more shadowing.

Figure 6.3 shows the simulated reflected nearfield intensity images for a 42m Rh_3Ta absorber candidate. The intensities are plotted for a 20P40nm dense contact-hole pattern at $6°$ and $10°$ propagation angles. The higher propagation angle results in increased intensity loss in open regions in the contact-hole pattern.
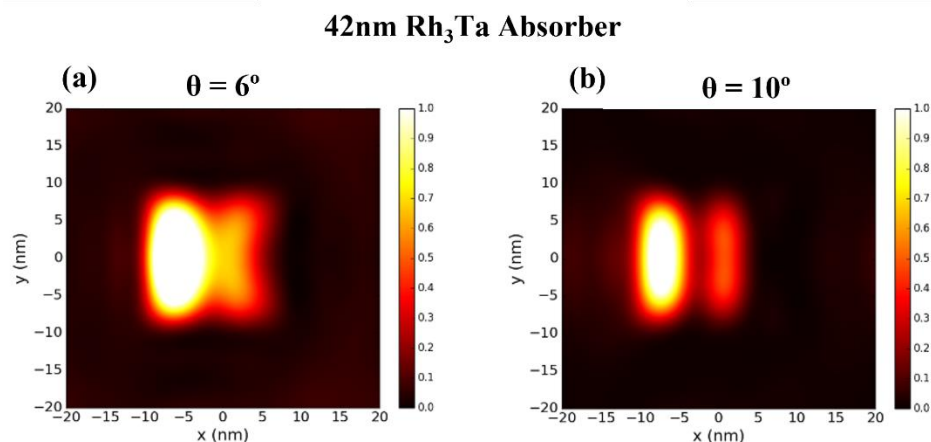
Figure 6.3: Reflected nearfield intensities for a 40nm pitch contact-holes pattern with a 20nm opening imaged using the 42nm Rh_3Ta absorber at propagation angle (a) $6°$ and (b) $10°$.

Figure 6.4 shows the simulated reflected nearfield intensity images for a 42m MoPt

absorber candidate. The intensities are plotted for a 20P40nm dense contact-hole pattern at

6° and 10° propagation angles. The MoPt absorber candidate has a higher refractive index

n than the Rh$_3$Ta absorber candidate but a similar extinction coefficient k (see Table 5.1).

Therefore, the reflected intensity distributions for both absorber candidates appear to be

similar.
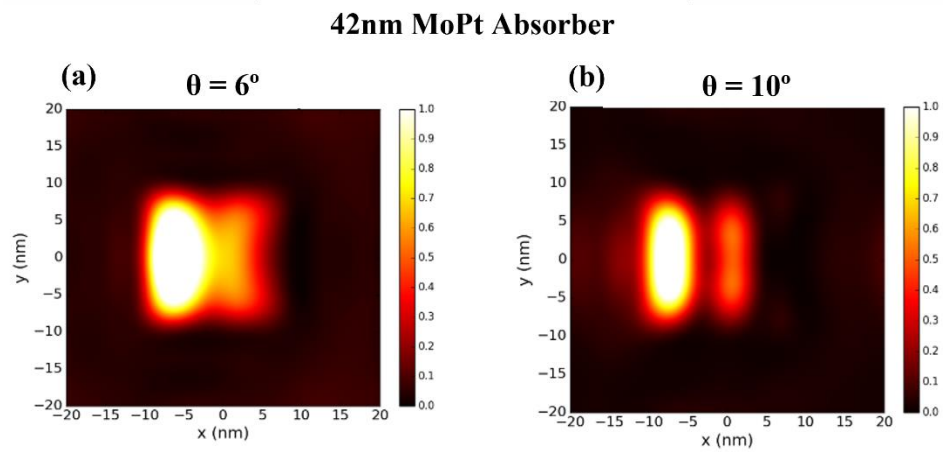
Figure 6.4: Reflected nearfield intensities for a 40nm pitch contact-holes pattern with a 20nm opening imaged using the 42nm MoPt absorber at propagation angle (a) 6° and (b) 10°.

7 Appendix B

7.1 Nearfield Distribution Intensity Imaging Script

Python script to generate nearfield distribution plots in the *DrLitho* software suite as shown in Figures 6.1 and 6.2. The script takes the following input parameters:

- Linewidth
- Pitch
- Incidence angle
- Layer thicknesses
- Optical constants
- File name

```
from dlProcess import graphics_bug_fix
from drlitho.emf import waveguide
from drlitho.emf.waveguide.wx import maskplot
import pylab
import math
import numpy
import os
import drlitho.utilities.readmatrix

linewidth = 0.013
pitch     = 0.1

# waveguide settings for EUV mask
wg = waveguide.waveguide_t()
wife = waveguide.Wife()

# general parameters
wg.simmode                = "3D"
wg.masktype               = "EUV"
wg.polarization           = 90.
wg.incidence_angle        = 6.
wg.incidence_angle_azimut = 0.
wg.orders                 = -1
wg.wavelength             = 0.0135
wg.domain_leftborder      = -4.*pitch/2
wg.domain_rightborder     = 4.*pitch/2
wg.refl_field_output_pos  = 0.01
wg.trans_field_output_pos = 0.0
wg.field_points_x         = 200
wg.orders                 = -1
```

```
# mask geometry specification
mask = waveguide.WGMask()
mask.setPitchX(4*pitch)
mask.setPitchY(0.1)

# vacuum on top
layer = waveguide.WGLayer()
layer.thickness = 0.02
layer.addRect(0.0, 0.0, 4 * pitch, 0.1, 1.0, 0.0)
mask.addLayer(layer)


# absorber
layer = waveguide.WGLayer()
layer.thickness = 0.055 # absorber
layer.addRect(0.0, 0.0, 4 * pitch, 0.1, 1.0, 0.0)
layer.addRect(0.0, 0.0, 4 * linewidth, 0.1, n, k)
mask.addLayer(layer)


# capping layer: 2nm ruthenium
layer = waveguide.WGLayer()
layer.thickness = 0.002
layer.addRect(0.0, 0.0, 4 * pitch, 0.1, 0.88634, -0.01707)
mask.addLayer(layer)
# 40 x MoSi layer
for i in range(0, 40, 1):
        # Mo
        layer = waveguide.WGLayer()
        layer.thickness = 0.003
        layer.addRect(0.0, 0.0, 4 * pitch, 0.1, 0.91943, -0.00663)
        mask.addLayer(layer)
        # Si
        layer = waveguide.WGLayer()
        layer.thickness = 0.004
        layer.addRect(0.0, 0.0, 4 * pitch, 0.1, 0.99875, -0.00183)
        mask.addLayer(layer)
# Substrate layer, SiO2
layer = waveguide.WGLayer()
layer.thickness = 0.02
layer.addRect(0.0, 0.0, 4 * pitch, 0.1, 0.98, -0.00182109)
mask.addLayer(layer)

#Viusalize mask
m = maskplot.MaskPlot()
m.input = mask
m.viewDirection = "TOP"
m.show()

# output parameters
```

```python
        wg.restype      = "ISOTROPIC"
        wg.refl_spec    = "NO"
        wg.refl_field   = "field.dat"   #Generates only reflected near field.
        wg.refl_csol    = "NO"
        wg.refl_nohop   = "NO"
        wg.trans_spec   = "NO"
        wg.trans_field  = "NO"
        wg.trans_csol   = "NO"
        wg.trans_nohop  = "NO"
        wg.mask_data    = "NO"
        wg.normalization = 0
        wg.screenout    = 0

        # additional parameters for the internal field computation
        wife.z_res = 0.0002
        for i in range(1, 85, 1):
            wife.set_layer_resolution(i, 0.0002)
        wife.setSpectrumMode(waveguide.TOTAL) #waveguide.TOTAL,
waveguide.FORWARD_PROPAGATING,  waveguide.BACKWARD_PROPAGATING
        wg.SetWife(wife)

        #Specify mask as waveguide compound
        wg.setMask(mask)


        wg.run() #run simulation

        # extraction of some internal field cuts from the full field #
        wife.compute_XZ_slice([0], 101, 101)  # List of y-point-positions where the internal field
is computed / number of field points in x- / y-direction
        dataFile = "xz_cut_E.dat"
        wg.wife.write_XZ_slice(dataFile, "E")   # intensity of complete E-field
        xz_cut = numpy.loadtxt("0_" + dataFile)
        os.remove("0_" + dataFile)
        os.remove("spectrum_output.h5")

        # generate near field plot
        pylab.figure() #hVacuumTop + hARC + hAbsorber + hCapping + 40*hBilayer +
hSubstrate
        height = 20. + 14. + 60. + 2.5 + 40*(3. + 4.) + 20.
        pylab.imshow(xz_cut[::-1,:], interpolation = "bilinear",
                origin = "lower", cmap = pylab.cm.hot,
                vmin = 0., vmax = 3., aspect = "auto", extent = (-2000*pitch, 2000*pitch, 0,
395))
        pylab.xlabel("x (nm)", size = 20)
        pylab.xticks(size = 18)
        pylab.ylabel("z (nm)", size = 20)
        pylab.yticks(size = 18)

        pylab.savefig("TaBN_CRA6.png")
        pylab.close()
```

```
#Visualization of the near field and mask layout
near_field_data = drlitho.utilities.readmatrix.ReadDoubleMatrixFile("int_iso_field.dat")
near_field_data = pylab.transpose(near_field_data)

pylab.figure()
pylab.imshow(near_field_data, interpolation = "bilinear", origin = "lower",
            #cmap = pylab.cm.hot, vmin = 0., vmax = 1., aspect = "auto",
            #extent = (-1000*pitch/2, 1000*pitch/2, -1000*pitch/2, 1000*pitch/2))
pylab.xlabel("x (nm)", size = 18)
pylab.xticks(size = 16)
pylab.ylabel("y (nm)", size = 18)
pylab.yticks(size = 16)
pylab.colorbar()
pylab.title("Near field intensity", size = 20)
pylab.savefig("FileName.png")
pylab.close()
```

7.2   Reflected Nearfield Intensity Imaging Script

Python script to generate reflected nearfield intensity plots in the *Dr.Litho* software

suite as shown in Figures 6.3 and 6.4. The script takes following input parameters:

- Linewidth
- Pitch
- Incidence angle
- Layer thicknesses
- Optical constants
- File name

```
"""
@title: Waveguide: Nearfields EUV
Simulation of the reflected near field of a EUV mask with a contact holes
Mask:
- 20nm contact
- pitch: 40nm
- standard MoSi-stack

Optical settings:
- wavelength=13.5nm
- Incidence angle 6 degree
- y-polarized light

@requirements:
- waveguide
```

@outputs:
- nearfield.png
- int_iso_field.dat
- pha_iso_field.dat

@version:
29/10/2019

@test:
4

@keywords:
EUV, nearfield

"""
```python
from dlProcess import graphics_bug_fix # important to use MayaVi (3D plotting); import drlitho.emf.waveguide
import pylab
import drlitho.utilities.readmatrix
from drlitho.emf.waveguide.wx import maskplot

# parameter settings to be used in script
size      =  0.020
pitch     =  0.040
reduction  =  4

wg = drlitho.emf.waveguide.waveguide_t()
wg.simmode  = "3D"
wg.orders   = 5
wg.orders_z = 5

# incident light
wg.wavelength            = 0.0135
wg.polarization          = 90.0
wg.incidence_angle       = 10
wg.incidence_angle_azimut = 0.0

# output
wg.restype       = "ISOTROPIC"
wg.field_points_x = 257
wg.field_points_y = 257
wg.normalization  = 0
wg.refl_spec     = "NO"
wg.refl_field    = "field.dat"
wg.refl_csol     = "NO"
wg.refl_nohop    = "NO"
wg.trans_spec    = "NO"
wg.trans_field   = "NO"
wg.trans_csol    = "NO"
wg.trans_nohop   = "NO"
```

```
wg.mask_data      = "NO"
wg.screenout      = 0

# definition of 3D mask layout: from illumination side ...
mask = drlitho.emf.waveguide.WGMask()
mask.setPitchX(reduction*pitch)
mask.setPitchY(reduction*pitch)

# air layer
layer = drlitho.emf.waveguide.WGLayer()
layer.thickness = 0.0
layer.addRect(0.0, 0.0, reduction*pitch, reduction*pitch, 1.0, 0.0)
mask.addLayer(layer)
mask.addLayer(layer)

# lower absorber layer
layer = drlitho.emf.waveguide.WGLayer()
layer.thickness = 0.045
layer.addRect(0.0, 0.0, reduction*pitch, reduction*pitch, 0.9806, -0.0632)
layer.addRect(0.0, 0.0, reduction*size, reduction*size, 1.0, 0.0)
mask.addLayer(layer)

# top  capping layer: 2nm ruthenium
layer = drlitho.emf.waveguide.WGLayer()
layer.thickness = 0.01
layer.addRect(0.0, 0.0, reduction*pitch, reduction*pitch, 0.88638, -0.01708)

mask.addLayer(layer)
# 40 bi-layers of Mo (3nm) Si (4nm)
for i in range(0, 40, 1):
    # Mo
    layer = drlitho.emf.waveguide.WGLayer()
    layer.thickness = 0.003
    layer.addRect(0.0, 0.0, reduction*pitch, reduction*pitch, 0.92184, -0.00663)

    mask.addLayer(layer)
    # Si
    layer = drlitho.emf.waveguide.WGLayer()
    layer.thickness = 0.004
    layer.addRect(0.0, 0.0, reduction*pitch, reduction*pitch, 0.99901, -0.00183)

  mask.addLayer(layer)
# substrate layer: 20nm SiO2
layer = drlitho.emf.waveguide.WGLayer()
layer.thickness = 0.02
layer.addRect(0.0, 0.0, reduction*pitch, reduction*pitch, 0.99, -0.00182109)

mask.addLayer(layer)
wg.setMask(mask)

# plot mask geometry
```

```
m = maskplot.MaskPlot()
m.input = mask
m.show()

wg.run()

# Visualization of the near field
near_field_data = drlitho.utilities.readmatrix.ReadDoubleMatrixFile("int_iso_field.dat")
near_field_data = pylab.transpose(near_field_data)

pylab.figure()
pylab.imshow(near_field_data, interpolation = "bilinear", origin = "lower",
          cmap = pylab.cm.hot, vmin = 0., vmax = 1., aspect = "auto",
          extent = (-1000*pitch/2, 1000*pitch/2, -1000*pitch/2, 1000*pitch/2))
pylab.xlabel("x (nm)", size = 18)
pylab.xticks(size = 16)
pylab.ylabel("y (nm)", size = 18)
pylab.yticks(size = 16)
pylab.colorbar()
pylab.title("Near field intensity", size = 20)
pylab.savefig("nearfield_AlTe_74%Te_45nm_CRA10.png")
pylab.show()
pylab.close()
```

8 References

[1]   J. S. Kilby, "Miniaturized electronic circuits," US3138743A, Jun. 23, 1964 Accessed: Mar. 05, 2021. [Online]. Available: https://patents.google.com/patent/US3138743/en

[2]   J. S. Kilby, "Invention of the integrated circuit," *IEEE Transactions on Electron Devices*, vol. 23, no. 7, pp. 648–654, Jul. 1976, doi: 10.1109/T-ED.1976.18467.

[3]   G. E. Moore, "Cramming more components onto integrated circuits, Reprinted from Electronics, volume 38, number 8, April 19, 1965, pp.114 ff.," *IEEE Solid-State Circuits Society Newsletter*, vol. 11, no. 3, pp. 33–35, Sep. 2006, doi: 10.1109/N-SSC.2006.4785860.

[4]   G. E. Moore, "Progress in digital integrated electronics," in *Electron devices meeting*, Washington, DC, 1975, pp. 11–13.

[5]   G. E. Moore, "Lithography and the Future of Moore's Law," *IEEE Solid-State Circuits Society Newsletter*, vol. 11, no. 3, pp. 37–42, 2006.

[6]   "Transistor count," *Wikipedia*. Mar. 08, 2021. Accessed: Mar. 09, 2021. [Online]. Available: https://en.wikipedia.org/w/index.php?title=Transistor_count&oldid=1011020443

[7]   C. Mack, *Fundamental Principles of Optical Lithography: The Science of Microfabrication : The Science of Microfabrication*. Newy York, UNITED KINGDOM: John Wiley & Sons, Incorporated, 2007. Accessed: Mar. 09, 2021. [Online]. Available: http://ebookcentral.proquest.com/lib/rit/detail.action?docID=470628

[8]   B. W. Smith and K. Suzuki, *Microlithography: science and technology*. CRC press, 2020.

[9]   L. R. S. R. S, "XV. On the theory of optical images, with special reference to the microscope," *The London, Edinburgh, and Dublin Philosophical Magazine and Journal of Science*, vol. 42, no. 255, pp. 167–195, Aug. 1896, doi: 10.1080/14786449608620902.

[10]   A. E. Rosenbluth *et al.*, "Optimum mask and source patterns to print a given shape," in *Optical Microlithography XIV*, International Society for Optics and Photonics, Sep. 2001, pp. 486–502. doi: 10.1117/12.435748.

[11]   M. Bertero, "Linear inverse and III-posed problems," in *Advances in electronics and electron physics*, Elsevier, 1989, pp. 1–120.

[12]   R. Easton, "Inverse Imaging Problem," *Fourier Methods in Imaging*, p. 84.

[13]   A. Yagola, A. Leonov, and V. Titarenko, "ILL-Posed Problems and a priori information," in *Inverse Problems in Engineering Mechanics III*, Elsevier, 2002, pp. 235–244.

[14]   J. Finders *et al.*, *DUV LITHOGRAPHY (KrF) FOR 130 nm USING OFF-AXIS ILLUMINATION AND ASSISTING FEATURES*.

[15] B. W. Smith, S. Butt, Z. Alam, S. Kurinec, and R. L. Lane, "Attenuated phase shift mask materials for 248 and 193 nm lithography," *Journal of Vacuum Science & Technology B: Microelectronics and Nanometer Structures Processing, Measurement, and Phenomena*, vol. 14, no. 6, pp. 3719–3723, Nov. 1996, doi: 10.1116/1.588655.

[16] O. W. Otto *et al.*, "Automated optical proximity correction: a rules-based approach," in *Optical/Laser Microlithography VII*, International Society for Optics and Photonics, 1994, pp. 278–293.

[17] B. E. Saleh and S. I. Sayegh, "Reduction of errors of microphotographic reproductions by optimal corrections of original masks," *Optical Engineering*, vol. 20, no. 5, pp. 781–784, 1981.

[18] B. E. Saleh and K. M. Nashold, "Image construction: optimum amplitude and phase masks in photolithography," *Applied optics*, vol. 24, no. 10, pp. 1432–1437, 1985.

[19] S. I. Sayegh and B. E. Saleh, "Image design: generation of a prescribed image at the output of a band-limited system," *IEEE transactions on pattern analysis and machine intelligence*, no. 4, pp. 441–445, 1983.

[20] P. D. Robertson, F. W. Wise, A. N. Nasr, A. R. Neureuther, and C. H. Ting, "Proximity effects and influences of nonuniform illumination in projection lithography," in *Optical Microlithography I: Technology for the Mid-1980s*, SPIE, 1982, pp. 37–43.

[21] A. C. Liu and B. J. Lin, "A study of projected optical images for typical IC mask patterns illuminated by partially coherent light," *IEEE transactions on electron devices*, vol. 30, no. 10, pp. 1251–1263, 1983.

[22] A. E. Rosenbluth, D. Goodman, and B. J. Lin, "A critical examination of submicron optical lithography using simulated projection images," *Journal of Vacuum Science & Technology B: Microelectronics Processing and Phenomena*, vol. 1, no. 4, pp. 1190–1195, 1983.

[23] P. Chien and M. Chen, "Proximity effects in submicron optical lithography," in *Optical microlithography VI*, SPIE, 1987, pp. 35–41.

[24] B. W. Smith and D. E. Ewbank, "OPC and image optimization using localized frequency analysis," in *Optical Microlithography XV*, SPIE, 2002, pp. 148–157.

[25] L. W. Liebmann *et al.*, "Optimizing style options for subresolution assist features," in *Optical Microlithography XIV*, International Society for Optics and Photonics, 2001, pp. 141–152.

[26] E. Tamechika, T. H. T. Horiuchi, and K. H. K. Harada, "Resolution improvement using auxiliary pattern groups in oblique illumination lithography," *Japanese journal of applied physics*, vol. 32, no. 12S, p. 5856, 1993.

[27] B. J. Lin, A. M. Moruzzi, and A. E. Rosenbluth, "Lithographic process having improved image quality," Feb. 20, 1990

[28]   J. F. Chen and J. A. Matthews, "Mask for photolithography," Sep. 07, 1993

[29]   J. H. Bruning, "Optical imaging for microfabrication," *Journal of Vacuum Science and Technology*, vol. 17, no. 5, pp. 1147–1155, Sep. 1980, doi: 10.1116/1.570631.

[30]   "GCA Stepper - SMFL - RIT Wiki." https://wiki.rit.edu/display/smfl/GCA+Stepper (accessed Mar. 16, 2021).

[31]   "ASML Stepper - SMFL - RIT Wiki." https://wiki.rit.edu/display/smfl/ASML+Stepper (accessed Mar. 16, 2021).

[32]   B. J. Lin, "The 157-nm good/bad news from intel," *Journal of Micro/Nanolithography, MEMS and MOEMS*, vol. 2, no. 3. Society of Photo-Optical Instrumentation Engineers, pp. 165–166, 2003.

[33]   V. Bakshi and A. Yen, "Special section guest editorial: EUV sources for lithography," *Journal of Micro/Nanolithography, MEMS, and MOEMS*, vol. 11, no. 2. Society of Photo-Optical Instrumentation Engineers, pp. 021101–021101, 2012.

[34]   B. W. Smith, H. Kang, A. Bourov, F. Cropanese, and Y. Fan, "Water immersion optical lithography for the 45-nm node," in *Optical Microlithography XVI*, International Society for Optics and Photonics, Jun. 2003, pp. 679–689. doi: 10.1117/12.485489.

[35]   C.-T. Wu *et al.*, "The rapid introduction of immersion lithography for NAND flash: challenges and experience," in *Optical Microlithography XXI*, SPIE, 2008, pp. 454–463.

[36]   J. H. Burnett, S. G. Kaplan, E. L. Shirley, P. J. Tompkins, and J. E. Webb, "High-index materials for 193 nm immersion lithography," in *Optical Microlithography XVIII*, International Society for Optics and Photonics, May 2005, pp. 611–621. doi: 10.1117/12.600109.

[37]   M. Maenhoudt, J. Versluijs, H. Struyf, J. V. Olmen, and M. V. Hove, "Double patterning scheme for sub-0.25 k1 single damascene structures at NA=0.75, λ=193nm," in *Optical Microlithography XVIII*, International Society for Optics and Photonics, May 2005, pp. 1508–1518. doi: 10.1117/12.613326.

[38]   K. Lucas, C. Cork, B. Yu, G. Luk-Pat, B. Painter, and D. Z. Pan, "Implications of triple patterning for 14nm node design and patterning," in *Design for Manufacturability through Design-Process Integration VI*, SPIE, 2012, pp. 11–22.

[39]   Y. Drissi *et al.*, "SALELE process from theory to fabrication," in *Design-Process-Technology Co-optimization for Manufacturability XIII*, International Society for Optics and Photonics, Mar. 2019, p. 109620V. doi: 10.1117/12.2517051.

[40]   "IEEE International Roadmap for Devices and Systems - IEEE IRDS™." https://irds.ieee.org/ (accessed Mar. 29, 2021).

[41]   J. W. Goodman, "Wave-optics analysis of coherent optical systems," *Introduction to Fourier Optics*, pp. 96–97, 2005.

[42] M. Born and E. Wolf, *Principles of Optics: Electromagnetic Theory of Propagation, Interference and Diffraction of Light*. Saint Louis, UNITED KINGDOM: Elsevier Science & Technology, 1980. Accessed: Mar. 15, 2022. [Online]. Available: http://ebookcentral.proquest.com/lib/rit/detail.action?docID=4586942

[43] J. van Schoot, K. van I. Schenau, C. Valentin, and S. Migura, "EUV lithography scanner for sub-8nm resolution," in *Extreme Ultraviolet (EUV) Lithography VI*, SPIE, Mar. 2015, pp. 449–460. doi: 10.1117/12.2087502.

[44] V. Bakshi, H. Mizoguchi, T. Liang, A. Grenville, and J. Benschop, "Special section guest editorial: Euv lithography for the 3-nm node and beyond," *Journal of Micro/Nanolithography, MEMS, and MOEMS*, vol. 16, no. 4, pp. 041001–041001, 2017.

[45] W. H. Bragg and W. L. Bragg, "The reflection of X-rays by crystals," *Proceedings of the Royal Society of London. Series A, Containing Papers of a Mathematical and Physical Character*, vol. 88, no. 605, pp. 428–438, Jul. 1913, doi: 10.1098/rspa.1913.0040.

[46] B. W. Smith, P. Venkataraman, S. K. Kurinec, and R. S. Mackay, "Materials for reflective multilayer coatings for EUV wavelengths," in *Emerging Lithographic Technologies II*, International Society for Optics and Photonics, Jun. 1998, pp. 544–554. doi: 10.1117/12.309614.

[47] F. Scholze, J. Tu\" mmler, E. Gullikson, and A. Aquila, "Comparison of extreme ultraviolet reflectance measurements," *Journal of Micro/Nanolithography, MEMS and MOEMS*, vol. 2, no. 3, pp. 233–235, 2003.

[48] D. M. Tennant *et al.*, "Comparison of reflective mask technologies for soft x-ray projection lithography," presented at the 11th Annual BACUS Symposium on Photomask Technology, K. C. McGinnis, Ed., Sunnyvale, United States, Jan. 1992, pp. 91–104. doi: 10.1117/12.56938.

[49] B. L. Fontaine *et al.*, "Architectural choices for EUV lithography masks: patterned absorbers and patterned reflectors," in *Emerging Lithographic Technologies VIII*, SPIE, May 2004, pp. 300–310. doi: 10.1117/12.539074.

[50] S. B. Hill *et al.*, "EUV testing of multilayer mirrors: critical issues," in *Emerging Lithographic Technologies X*, SPIE, 2006, pp. 120–128.

[51] "CXRO X-Ray Interactions With Matter." https://henke.lbl.gov/optical_constants/ (accessed Oct. 06, 2020).

[52] G. L. Fenger, "Image-based EUVL aberration metrology," ProQuest Dissertations Publishing, 2013. Accessed: Mar. 30, 2022. [Online]. Available: https://go.exlibris.link/WWN0rFgt

[53] R. Soufli, S. Bajt, R. M. Hudyma, and J. S. Taylor, "Optics and multilayer coatings for EUVL systems," *EUV lithography*, vol. 178, p. 133, 2009.

[54] H. Kinoshita and O. Wood, "EUV lithography: An historical perspective," *EUV lithography*, pp. 1–54, 2008.

[55]   S. Raghunathan, G. McIntyre, G. Fenger, and O. Wood, "Mask 3D effects and compensation for high NA EUV lithography," in *Extreme Ultraviolet (EUV) Lithography IV*, SPIE, Apr. 2013, pp. 334–346. doi: 10.1117/12.2011643.

[56]   A. Erdmann, P. Evanschitzky, J. T. Neumann, and P. Graeupner, "Mask-induced best-focus shifts in deep ultraviolet and extreme ultraviolet lithography," *JM3*, vol. 15, no. 2, p. 021205, Mar. 2016, doi: 10.1117/1.JMM.15.2.021205.

[57]   J. Finders, L. de Winter, and T. Last, "Mitigation of mask three-dimensional induced phase effects by absorber optimization in ArF i and extreme ultraviolet lithography," *Journal of Micro/Nanolithography, MEMS, and MOEMS*, vol. 15, no. 2, p. 021408, 2016.

[58]   A. Erdmann, P. Evanschitzky, H. Mesilhy, V. Philipsen, E. Hendrickx, and M. Bauer, "Attenuated phase shift mask for extreme ultraviolet: can they mitigate three-dimensional mask effects?," *JM3*, vol. 18, no. 1, p. 011005, Aug. 2018, doi: 10.1117/1.JMM.18.1.011005.

[59]   N. Davydova *et al.*, "Alternative EUV mask technology for Mask 3D effect compensation," p. 23, 2014.

[60]   J. T. Neumann, P. Gräupner, W. Kaiser, R. Garreis, and B. Geh, "Interactions of 3D mask effects and NA in EUV lithography," in *Photomask Technology 2012*, SPIE, Nov. 2012, pp. 322–333. doi: 10.1117/12.2009117.

[61]   A. Erdmann, D. Xu, P. Evanschitzky, V. Philipsen, V. Luong, and E. Hendrickx, "Characterization and mitigation of 3D mask effects in extreme ultraviolet lithography," *Advanced Optical Technologies*, vol. 6, no. 3–4, pp. 187–201, Jun. 2017, doi: 10.1515/aot-2017-0019.

[62]   T. Schmoeller *et al.*, "EUV pattern shift compensation strategies," in *Emerging Lithographic Technologies XII*, SPIE, Mar. 2008, pp. 389–396. doi: 10.1117/12.772640.

[63]   V. Philipsen *et al.*, "Reducing EUV mask 3D effects by alternative metal absorbers," in *Extreme Ultraviolet (EUV) Lithography VIII*, International Society for Optics and Photonics, Mar. 2017, p. 1014310. doi: 10.1117/12.2257929.

[64]   N. Davydova *et al.*, "Experimental approach to EUV imaging enhancement by mask absorber height optimization," in *29th European Mask and Lithography Conference*, SPIE, Oct. 2013, pp. 54–68. doi: 10.1117/12.2030806.

[65]   N. Davydova *et al.*, "Imaging performance improvements by EUV mask stack optimization," in *27th European Mask and Lithography Conference*, SPIE, Apr. 2011, pp. 319–331. doi: 10.1117/12.884504.

[66]   V. Philipsen, E. Hendrickx, R. Jonckheere, N. Davydova, T. Fliervoet, and J. T. Neumann, "Actinic characterization and modeling of the EUV mask stack," in *29th European Mask and Lithography Conference*, International Society for Optics and Photonics, Oct. 2013, p. 88860B. doi: 10.1117/12.2030663.

[67] F. Scholze, C. Laubis, K. V. Luong, and V. Philipsen, "Update on optical material properties for alternative EUV mask absorber materials," in *33rd European Mask and Lithography Conference*, SPIE, Sep. 2017, pp. 44–55. doi: 10.1117/12.2279702.

[68] A. Erdmann, H. S. Mesilhy, P. Evanschitzky, V. Philipsen, F. J. Timmermans, and M. Bauer, "Perspectives and tradeoffs of absorber materials for high NA EUV lithography," *JM3*, vol. 19, no. 4, p. 041001, Oct. 2020, doi: 10.1117/1.JMM.19.4.041001.

[69] P. Yan *et al.*, "EUV mask absorber characterization and selection," in *Photomask and Next-Generation Lithography Mask Technology VII*, SPIE, Jul. 2000, pp. 116–123. doi: 10.1117/12.392025.

[70] R. Sejpal *et al.*, "Exploring alternative EUV mask absorber for iN5 self-aligned block and contact layers," in *Photomask Technology 2019*, International Society for Optics and Photonics, Sep. 2019, p. 111481B. doi: 10.1117/12.2536892.

[71] M. Burkhardt, "Investigation of alternate mask absorbers in EUV lithography," in *Extreme Ultraviolet (EUV) Lithography VIII*, SPIE, Mar. 2017, pp. 195–208. doi: 10.1117/12.2258266.

[72] M. Burkhardt, A. D. Silva, J. Church, L. Meli, C. Robinson, and N. Felix, "Investigation of mask absorber induced image shift in EUV lithography," in *Extreme Ultraviolet (EUV) Lithography X*, SPIE, Mar. 2019, pp. 232–250. doi: 10.1117/12.2515365.

[73] S. Migura, B. Kneer, J. T. Neumann, W. Kaiser, and J. Van Schoot, "Anamorphic high-NA EUV lithography optics," presented at the 31st European Mask and Lithography Conference, U. F. W. Behringer and J. Finders, Eds., Eindhoven, Netherlands, Sep. 2015, p. 96610T. doi: 10.1117/12.2196393.

[74] J. V. Schoot *et al.*, "High-numerical aperture extreme ultraviolet scanner for 8-nm lithography and beyond," *J. Micro/Nanolith. MEMS MOEMS*, vol. 16, no. 04, p. 1, Oct. 2017, doi: 10.1117/1.JMM.16.4.041010.

[75] J. Van Schoot *et al.*, "The future of EUV lithography: continuing Moore's Law into the next decade," in *Extreme Ultraviolet (EUV) Lithography IX*, N. M. Felix and K. A. Goldberg, Eds., San Jose, United States: SPIE, Mar. 2018, p. 23. doi: 10.1117/12.2295800.

[76] P. Graeupner, D. Golde, J. van Schoot, P. Kuerz, and J. Stoeldraijer, "High NA EUV optics: preparing the next major lithography step," in *Optical and EUV Nanolithography XXXVI*, SPIE, Apr. 2023, p. PC1249405. doi: 10.1117/12.2658370.

[77] J. van Schoot, "High-NA EUVL exposure tool: program progress and mask interaction," in *Photomask Japan 2022: XXVIII Symposium on Photomask and Next-Generation Lithography Mask Technology*, SPIE, Sep. 2022, p. PC123250A. doi: 10.1117/12.2656140.

[78] L. de Winter *et al.*, "Extreme ultraviolet scanner with high numerical aperture: obscuration and wavefront description," *JM3*, vol. 21, no. 2, p. 023801, Apr. 2022, doi: 10.1117/1.JMM.21.2.023801.

[79] I. Lee, J.-H. Franke, V. Philipsen, K. Ronse, S. De Gendt, and E. Hendrickx, "Hyper-NA EUV lithography: an imaging perspective," in *Optical and EUV Nanolithography XXXVI*, A. Lio and M. Burkhardt, Eds., San Jose, United States: SPIE, Apr. 2023, p. 7. doi: 10.1117/12.2659153.

[80] Rayleigh, "XXXI. Investigations in optics, with special reference to the spectroscope," *The London, Edinburgh, and Dublin Philosophical Magazine and Journal of Science*, vol. 8, no. 49, pp. 261–274, Oct. 1879, doi: 10.1080/14786447908639684.

[81] D. D. Flanders, A. M. Hawryluk, and H. I. Smith, "Spatial period division—A new technique for exposing submicrometer-linewidth periodic and quasiperiodic patterns," *Journal of Vacuum Science and Technology*, vol. 16, no. 6, pp. 1949–1952, Nov. 1979, doi: 10.1116/1.570362.

[82] M. D. Levenson, N. S. Viswanathan, and R. A. Simpson, "Improving resolution in photolithography with a phase-shifting mask," *IEEE Transactions on Electron Devices*, vol. 29, no. 12, pp. 1828–1836, Dec. 1982, doi: 10.1109/T-ED.1982.21037.

[83] K. K. H. Toh, G. T. Dao, R. R. Singh, and H. T. Gaw, "Chromeless phase-shifted masks: a new approach to phase-shifting masks," in *10th Annual Symp on Microlithography*, SPIE, Mar. 1991, pp. 27–53. doi: 10.1117/12.29750.

[84] H. Watanabe, Y. Todokoro, and M. Inoue, "Transparent phase shifting mask," in *International Technical Digest on Electron Devices*, Dec. 1990, pp. 821–824. doi: 10.1109/IEDM.1990.237036.

[85] H. Watanabe, Y. Todokoro, Y. Hirai, and M. Inoue, "Transparent phase-shifting mask with multistage phase shifter and comb-shaped shifter," in *Optical/Laser Microlithography IV*, SPIE, Jul. 1991, pp. 101–110. doi: 10.1117/12.44832.

[86] G. Galan, F. Lalanne, P. S. P. Schiavone, and J.-M. T. J.-M. Temerson, "Application of Alternating-Type Phase Shift Mask to Polysilicon Level for Random Logic Circuits," *Jpn. J. Appl. Phys.*, vol. 33, no. 12S, p. 6779, Dec. 1994, doi: 10.1143/JJAP.33.6779.

[87] L. W. Liebmann, J. Lund, F.-L. Heng, and I. C. Graur, "Enabling alternating phase shifted mask designs for a full logic gate level," *JM3.1*, vol. 1, no. 1, pp. 31–42, Apr. 2002, doi: 10.1117/1.1435368.

[88] M. Sugawara, A. Chiba, H. Yamanashi, and I. Nishiyama, "Alternating Phase Shift Mask in Extreme Ultra Violet Lithography," *Jpn. J. Appl. Phys.*, vol. 42, no. Part 1, No. 6B, pp. 3776–3783, Jun. 2003, doi: 10.1143/JJAP.42.3776.

[89] B. J. Lin, "The attenuated phase-shifting mask," *Solid State Technology*, vol. 35, no. 1, pp. 43–48, Jan. 1992.

[90] H. I. Smith, E. H. Anderson, and M. L. Schattenburg, "Lithography mask with a π-phase shifting attenuator," US4890309A, Dec. 26, 1989 Accessed: May 28, 2023. [Online]. Available: https://patents.google.com/patent/US4890309A/en

[91] "Generalized inverse lithography methods for phase-shifting mask design." https://opg.optica.org/oe/fulltext.cfm?uri=oe-15-23-15066&id=144625 (accessed May 28, 2023).

[92] P. D. Buck and M. L. Rieger, "Phase-shift mask applications," in *Optical/Laser Microlithography IV*, SPIE, Jul. 1991, pp. 218–228. doi: 10.1117/12.44806.

[93] J. A. Dobrowolski, "Optical properties of films and coatings," *Handbook of Optics I*, pp. 42–3, 1995.

[94] B. L. Henke, E. M. Gullikson, and J. C. Davis, "X-ray interactions: photoabsorption, scattering, transmission, and reflection at E= 50-30,000 eV, Z= 1-92," *Atomic data and nuclear data tables*, vol. 54, no. 2, pp. 181–342, 1993.

[95] M. Fox, *Optical Properties of Solids*. Oxford, UNITED KINGDOM: Oxford University Press, Incorporated, 2010. Accessed: Mar. 15, 2022. [Online]. Available: http://ebookcentral.proquest.com/lib/rit/detail.action?docID=3056080

[96] H. A. Lorentz, *The theory of electrons and its applications to the phenomena of light and radiant heat*. New York: Dover Publications, 1952.

[97] P. Drude, "Zur Elektronentheorie der Metalle," *Annalen der Physik*, vol. 306, no. 3, pp. 566–613, 1900, doi: 10.1002/andp.19003060312.

[98] H. A. Kramers, "La diffusion de la lumiere par les atomes," in *Atti Cong. Intern. Fisica (Transactions of Volta Centenary Congress) Como*, 1927, pp. 545–557.

[99] R. de L. Kronig, "On the Theory of Dispersion of X-Rays," *J. Opt. Soc. Am., JOSA*, vol. 12, no. 6, pp. 547–557, Jun. 1926, doi: 10.1364/JOSA.12.000547.

[100] R. Sejpal and B. Smith, "Identifying extreme ultraviolet lithography attenuated phase shifting mask absorber materials using effective media approximation modeling," *Journal of Vacuum Science & Technology B, Nanotechnology and Microelectronics: Materials, Processing, Measurement, and Phenomena*, vol. 39, no. 6, p. 062604, 2021.

[101] O. Wiener, "Die Theorie des Mischkorpers fur das Feld der stationaren Stromung," *Abhandlungen der Sachsischen Gesellschaft der Akademischen Wissenschaften in Mathematik und Physik*, vol. 32, pp. 507–604, 1912.

[102] A. Bourov, "Optical properties of materials for 157 nm lithography," *Theses*, Jan. 2003, [Online]. Available: https://scholarworks.rit.edu/theses/8382

[103] J. C. M. Garnett and J. Larmor, "XII. Colours in metal glasses and in metallic films," *Philosophical Transactions of the Royal Society of London. Series A, Containing Papers of a Mathematical or Physical Character*, vol. 203, no. 359–371, pp. 385–420, Jan. 1904, doi: 10.1098/rsta.1904.0024.

[104] D. a. G. Bruggeman, "Berechnung verschiedener physikalischer Konstanten von heterogenen Substanzen. I. Dielektrizitätskonstanten und Leitfähigkeiten der Mischkörper aus isotropen Substanzen," *Annalen der Physik*, vol. 416, no. 7, pp. 636–664, 1935, doi: 10.1002/andp.19354160705.

[105] G. A. Niklasson, C. G. Granqvist, and O. Hunderi, "Effective medium models for the optical properties of inhomogeneous materials," *Appl. Opt., AO*, vol. 20, no. 1, pp. 26–30, Jan. 1981, doi: 10.1364/AO.20.000026.

[106] D. E. Aspnes, J. B. Theeten, and F. Hottier, "Investigation of effective-medium models of microscopic surface roughness by spectroscopic ellipsometry," *Phys. Rev. B*, vol. 20, no. 8, pp. 3292–3302, Oct. 1979, doi: 10.1103/PhysRevB.20.3292.

[107] D. E. Aspnes, "Optical properties of thin films," *Thin Solid Films*, vol. 89, no. 3, pp. 249–262, Mar. 1982, doi: 10.1016/0040-6090(82)90590-9.

[108] D. E. Aspnes, "Bounds on allowed values of the effective dielectric function of two-component composites at finite frequencies," *Phys. Rev. B*, vol. 25, no. 2, pp. 1358–1361, Jan. 1982, doi: 10.1103/PhysRevB.25.1358.

[109] W. A. G. III, D. Brenner, S. E. Lyshevski, and G. J. Iafrate, *Handbook of Nanoscience, Engineering, and Technology*. CRC Press, 2018.

[110] H. Okamoto and H. Okamoto, *Phase diagrams for binary alloys*, vol. 44. ASM international Materials Park, OH, 2000.

[111] V. Luong *et al.*, "Ni-Al Alloys as Alternative EUV Mask Absorber," *Applied Sciences*, vol. 8, no. 4, Art. no. 4, Apr. 2018, doi: 10.3390/app8040521.

[112] R. Sejpal, W. Maguire, and B. W. Smith, "Modeling and verification of next-gen EUV mask absorbers," in *Optical and EUV Nanolithography XXXVI*, SPIE, Apr. 2023, pp. 127–135. doi: 10.1117/12.2660823.

[113] J. Hale and B. Johs, "CompleteEASE." JA Woollam: Lincoln, NE, 2012.

[114] T. M. CompleteEASE, "Data Analysis Manual Version 4.63, JA Woollam Co," *Inc., Lincoln, NE*, p. 45, 2011.

[115] K. L. A. Tencor, "PROLITH," *Version X5*, vol. 1, 2015.

[116] C. A. Mack, "PROLITH: a comprehensive optical lithography model," in *Optical Microlithography IV*, International Society for Optics and Photonics, 1985, pp. 207–220.

[117] H. Mesilhy, P. Evanschitzky, G. Bottiglieri, E. Van Setten, T. Fliervoet, and A. Erdmann, "Pathfinding the perfect EUV mask: the role of the multilayer," in *Extreme Ultraviolet (EUV) Lithography XI*, International Society for Optics and Photonics, 2020, p. 1132316.

[118] F. J. Timmermans, C. van Lare, and J. Finders, "Alternative mask materials for low-k1 EUV imaging," in *35th European Mask and Lithography Conference (EMLC 2019)*, International Society for Optics and Photonics, Aug. 2019, p. 111770Y. doi: 10.1117/12.2535682.

[119] C. van Lare *et al.*, "Investigation into a prototype extreme ultraviolet low-n attenuated phase-shift mask," *JM3*, vol. 20, no. 2, p. 021006, May 2021, doi: 10.1117/1.JMM.20.2.021006.

[120] C. van Lare, F. Timmermans, and J. Finders, "Mask-absorber optimization: the next phase," *JM3*, vol. 19, no. 2, p. 024401, May 2020, doi: 10.1117/1.JMM.19.2.024401.

[121] M.-C. van Lare, F. J. Timmermans, and J. Finders, "Alternative reticles for low-k1 EUV imaging," in *International Conference on Extreme Ultraviolet Lithography 2019*, International Society for Optics and Photonics, Sep. 2019, p. 111470D. doi: 10.1117/12.2536415.

[122] R. Sejpal *et al.*, "Exploring alternative EUV mask absorber for iN5 self-aligned block and contact layers," in *Photomask Technology 2019*, International Society for Optics and Photonics, Sep. 2019, p. 111481B. doi: 10.1117/12.2536892.

[123] T. Fühner, T. Schnattinger, G. Ardelean, and A. Erdmann, "Dr. LiTHO: a development and research lithography simulator," in *Optical Microlithography XX*, International Society for Optics and Photonics, 2007, p. 65203F.

[124] "Computational Lithography and Optics," *Fraunhofer Institute for Integrated Systems and Device Technology IISB*. https://www.iisb.fraunhofer.de/en/research_areas/simulation/lithography.html (accessed Jul. 08, 2021).

[125] "TFCalc Demo and Manual." http://www.sspectra.com/demo.html (accessed Jul. 28, 2023).

[126] P. D. Bisschop, "Stochastic effects in EUV lithography: random, local CD variability, and printing failures," *JM3.1*, vol. 16, no. 4, p. 041013, Dec. 2017, doi: 10.1117/1.JMM.16.4.041013.

[127] M. Burkhardt, Z. Chen, S. Halle, R. Lallement, S. Sieg, and L. Meli, "Focus considerations of design pitches and absorber choice for EUV random logic," in *Optical and EUV Nanolithography XXXV*, SPIE, May 2022, pp. 78–95. doi: 10.1117/12.2614296.

[128] T. Kovalevich, L. V. Look, J.-H. Franke, and V. Philipsen, "Evaluation of LS printing and general understanding of imaging with DF low-n mask," in *International Conference on Extreme Ultraviolet Lithography 2022*, SPIE, Nov. 2022, p. PC122920M. doi: 10.1117/12.2644701.

[129] T. Kovalevich, L. V. Look, J.-H. Franke, and V. Philipsen, "Evaluation of Lines and Spaces printing and general understanding of imaging with dark field low-n mask," *JM3*, vol. 22, no. 2, p. 024401, Apr. 2023, doi: 10.1117/1.JMM.22.2.024401.

[130] H. Mesilhy *et al.*, "EUV mask absorber induced best focus shifts," in *Optical and EUV Nanolithography XXXV*, A. Lio and M. Burkhardt, Eds., San Jose, United States: SPIE, Jun. 2022, p. 10. doi: 10.1117/12.2614174.

[131] C. Van Lare, J. Finders, and T. Van Rhee, "Low-n mask progressing insights: focus on isolated features," in *International Conference on Extreme Ultraviolet Lithography 2022*, K. G. Ronse, P. A. Gargini, P. P. Naulleau, and T. Itani, Eds., Monterey, United States: SPIE, Dec. 2022, p. 31. doi: 10.1117/12.2644332.

[132] Z. Chen, M. Burkhardt, S. Sieg, and L. Meli, "EUV sub-resolution assist feature impact: experimental and simulation evaluation," in *Optical and EUV Nanolithography XXXVI*, SPIE, Apr. 2023, pp. 285–292. doi: 10.1117/12.2657634.

[133] F. Letzkus *et al.*, "Dry etch processes for the fabrication of EUV masks," *Microelectronic Engineering*, vol. 73–74, pp. 282–288, Jun. 2004, doi: 10.1016/j.mee.2004.02.054.

[134] T. Abe *et al.*, "Process development for EUV mask production," in *Photomask Technology 2006*, SPIE, Oct. 2006, pp. 1026–1032. doi: 10.1117/12.692519.

[135] Y. Du, C. J. Choi, G. Zhang, S.-J. Park, P.-Y. Yan, and K.-H. Baik, "TaN-based EUV mask absorber etch study," in *Photomask and Next-Generation Lithography Mask Technology XIII*, SPIE, May 2006, pp. 905–911. doi: 10.1117/12.681832.

[136] P.-Y. Yan *et al.*, "EUVL mask patterning with blanks from commercial suppliers," in *24th Annual BACUS Symposium on Photomask Technology*, SPIE, Dec. 2004, pp. 774–780. doi: 10.1117/12.569329.

[137] K.-H. Kwon, A. Efremov, S. J. Yun, I. Chun, and K. Kim, "Dry etching characteristics of Mo and Al2O3 films in O2/Cl2/Ar inductively coupled plasmas," *Thin Solid Films*, vol. 552, pp. 105–110, Feb. 2014, doi: 10.1016/j.tsf.2013.12.013.

[138] R. d'Agostino, F. Fracassi, and C. Pacifico, "Dry etching of Ti in chlorine containing feeds," *Journal of applied physics*, vol. 72, no. 9, pp. 4351–4357, 1992.

[139] F. Fracassi and R. d'Agostino, "Chemistry of titanium dry etching in fluorinated and chlorinated gases," *Pure and applied chemistry*, vol. 64, no. 5, pp. 703–707, 1992.

[140] R. W. Light, "Reactive ion etching of aluminum/silicon," *Journal of the Electrochemical Society*, vol. 130, no. 11, p. 2225, 1983.

[141] P. M. Schaible, W. C. Metzger, and J. P. Anderson, "Reactive ion etching of aluminum and aluminum alloys in an rf plasma containing halogen species," *Journal of Vacuum Science and Technology*, vol. 15, no. 2, pp. 334–337, 1978.

[142] S. Paolillo, D. Wan, F. Lazzarino, N. Rassoul, D. Piumi, and Z. Tőkei, "Direct metal etch of ruthenium for advanced interconnect," *Journal of Vacuum Science & Technology B*, vol. 36, no. 3, p. 03E103, May 2018, doi: 10.1116/1.5022283.

[143] V. Philipsen *et al.*, "Novel EUV mask absorber evaluation in support of next-generation EUV imaging," in *Photomask Technology 2018*, SPIE, Oct. 2018, pp. 53–65. doi: 10.1117/12.2501799.

[144] D.-S. Wuu, N.-H. Kuo, F.-C. Liao, R.-H. Horng, and M.-K. Lee, "Etching of platinum thin films in an inductively coupled plasma," *Applied Surface Science*, vol. 169–170, pp. 638–643, Jan. 2001, doi: 10.1016/S0169-4332(00)00803-5.

[145] X. Li, H. Zhou, R. J. W. Hill, M. Holland, and I. G. Thayne, "A Low Damage Etching Process of Sub-100 nm Platinum Gate Line for III–V Metal–Oxide–Semiconductor Field-Effect Transistor Fabrication and the Optical Emission Spectrometry of the Inductively Coupled Plasma of SF6/C4F8," *Jpn. J. Appl. Phys.*, vol. 51, no. 1S, p. 01AB01, Jan. 2012, doi: 10.1143/JJAP.51.01AB01.

[146] V. Philipsen *et al.*, "Single element and metal alloy novel EUV mask absorbers for improved imaging (Conference Presentation)," in *International Conference on Extreme Ultraviolet Lithography 2017*, SPIE, Oct. 2017, p. 104500G. doi: 10.1117/12.2280623.

[147] X. Sang, E. Chen, and J. P. Chang, "Patterning nickel for extreme ultraviolet lithography mask application I. Atomic layer etch processing," *Journal of Vacuum Science & Technology A*, vol. 38, no. 4, p. 042603, Jul. 2020, doi: 10.1116/6.0000190.

[148] X. Sang and J. P. Chang, "Patterning nickel for extreme ultraviolet lithography mask application. II. Hybrid reactive ion etch and atomic layer etch processing," *Journal of Vacuum Science & Technology A*, vol. 38, no. 4, p. 042604, Jul. 2020, doi: 10.1116/6.0000191.

[149] J. H. Kim and S. I. Woo, "Chemical Dry Etching of Platinum Using Cl2/CO Gas Mixture," *Chem. Mater.*, vol. 10, no. 11, pp. 3576–3582, Nov. 1998, doi: 10.1021/cm980337o.

[150] A. J. M. Mackus, M. J. M. Merkx, and W. M. M. Kessels, "From the Bottom-Up: Toward Area-Selective Atomic Layer Deposition with High Selectivity," *Chem. Mater.*, vol. 31, no. 1, pp. 2–12, Jan. 2019, doi: 10.1021/acs.chemmater.8b03454.

[151] R. Chen and S. F. Bent, "Chemistry for Positive Pattern Transfer Using Area-Selective Atomic Layer Deposition," *Advanced Materials*, vol. 18, no. 8, pp. 1086–1090, 2006, doi: 10.1002/adma.200502470.

[152] J. Yarbrough, A. B. Shearer, and S. F. Bent, "Next generation nanopatterning using small molecule inhibitors for area-selective atomic layer deposition," *Journal of Vacuum Science & Technology A*, vol. 39, no. 2, p. 021002, Mar. 2021, doi: 10.1116/6.0000840.

[153] M. Fang and J. C. Ho, "Area-Selective Atomic Layer Deposition: Conformal Coating, Subnanometer Thickness Control, and Smart Positioning," *ACS Nano*, vol. 9, no. 9, pp. 8651–8654, Sep. 2015, doi: 10.1021/acsnano.5b05249.

[154] M. F. J. Vos *et al.*, "Area-Selective Deposition of Ruthenium by Combining Atomic Layer Deposition and Selective Etching," *Chem. Mater.*, vol. 31, no. 11, pp. 3878–3882, Jun. 2019, doi: 10.1021/acs.chemmater.9b00193.

[155] G. N. Parsons and R. D. Clark, "Area-Selective Deposition: Fundamentals, Applications, and Future Outlook," *Chem. Mater.*, vol. 32, no. 12, pp. 4920–4953, Jun. 2020, doi: 10.1021/acs.chemmater.0c00722.

[156] M. Hatzakis, B. J. Canavello, and J. M. Shaw, "Single-Step Optical Lift-Off Process," *IBM Journal of Research and Development*, vol. 24, no. 4, pp. 452–460, Jul. 1980, doi: 10.1147/rd.244.0452.

[157] Z. Wang, K. Zhang, G. Chen, Z. Zhu, Y. Wang, and J. Wei, "A metal lift-off process through hyperbolic undercut of laser heat-mode lithography," *Materials Letters*, vol. 264, p. 127344, Apr. 2020, doi: 10.1016/j.matlet.2020.127344.

[158] H. S. Lee and J.-B. Yoon, "A simple and effective lift-off with positive photoresist," *J. Micromech. Microeng.*, vol. 15, no. 11, p. 2136, Oct. 2005, doi: 10.1088/0960-1317/15/11/020.

[159] K. M. Cheung *et al.*, "Chemical Lift-Off Lithography of Metal and Semiconductor Surfaces," *ACS Materials Lett.*, vol. 2, no. 1, pp. 76–83, Jan. 2020, doi: 10.1021/acsmaterialslett.9b00438.

[160] H. Wolf *et al.*, "Sub-20 nm silicon patterning and metal lift-off using thermal scanning probe lithography," *Journal of Vacuum Science & Technology B*, vol. 33, no. 2, p. 02B102, Nov. 2014, doi: 10.1116/1.4901413.

[161] D. Kang and W. Moon, "Improvement of High Dynamic Range Capacitive Displacement Sensor by a Global Planarization," *Journal of Sensor Technology*, vol. 01, Jan. 2011, doi: 10.4236/jst.2011.14014.